AD-A184 286 METALLURGICAL INVESTIGATION OF HOT DUCTILITY LOSS IN TI-6211 ALLOY(U) LOCKHEED MISSILES AND SPACE CO INC PALO ALTO CA R E LEWIS 15 JAN 86 LMSC-F108004 1/3

UNCLASSIFIED N00014-79-C-0449 F/G 11/6 NL

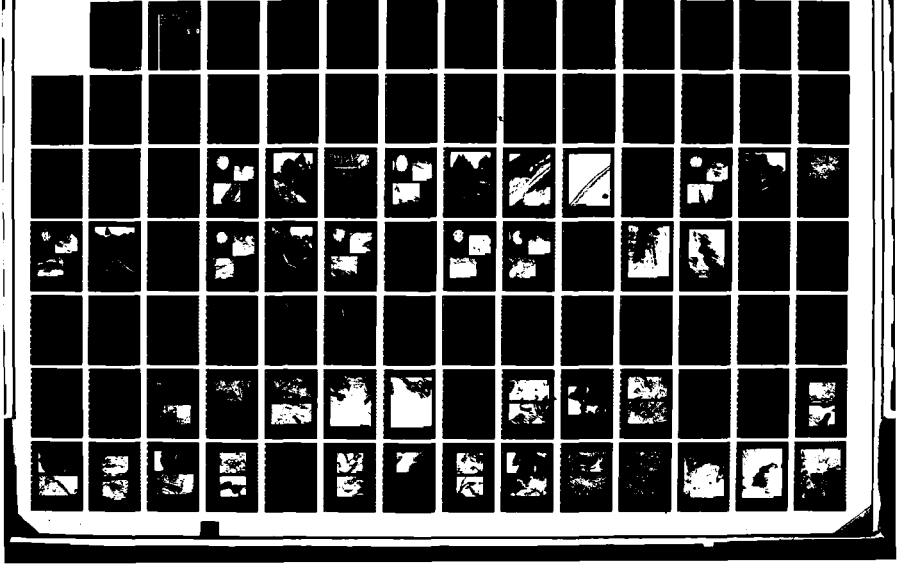

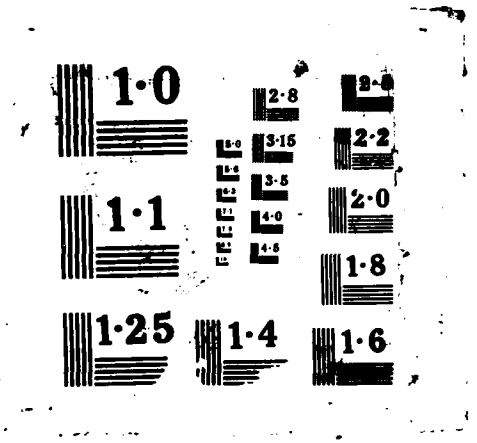
1·0
1·1
1·25
1·4
2·8
3·15
3·5
4·0
4·5
2·2
2·0
1·8
1·6

LMSC-F108004

(12)

METALLURGICAL INVESTIGATION OF HOT DUCTILITY LOSS IN TI-6211 ALLOY

R. E. Lewis
Lockheed Palo Alto Research Laboratory
3251 Hanover Street
Palo Alto, California 94304

January 1986

Final Technical Report for Period June 1979 to January 1986
Contract N00014-79-C-0449

Approved for Public Release; Distribution unlimited

Sponsored by:
OFFICE OF NAVAL RESEARCH
Arlington, Virginia 22209

Lockheed Missiles & Space Company, Inc.

Research and Development
3251 Hanover Street, Palo Alto, California 94304-1191

In reply refer to:
LMSC/F227204

15 July 1987

Scientific Officer
Director, Metallurgy & Ceramics Program
Material Sciences Division
Office of Naval Research
800 North Quincy Street
Arlington, Virginia 22217

Attention: Dr. Bruce A. MacDonald, Code 471

Subject: Transmittal of Final Report
Contract N00014-79-C-0449
Metallurgical Investigation of Fracture in Ti-6211 Alloy

Reference: (a) CDRL, Data Sequence A002

Enclosure: (1) Final Report entitled "Metallurgical Investigation of Hot Ductility Loss in Ti-6211 Alloy," LMSC/F108004 dated January 1986, (1 copy)

(2) DD 250 RDA001Z dated 87Jul15E

Gentlemen:

Enclosed please find copies of the Final Report for Contract N00014-79-C-0449 submitted in accord with the requirements of reference (a). Distribution of the report is also being made in compliance with the Supplemental Distribution List provided by the ONR Scientific Officer.

Upon your acceptance, please forward an executed copy of the Enclosure (2) DD 250 to the undersigned at the letterhead address, c/o Organization 90-31, Building 253. Thank you.

Very truly yours,

RESEARCH & DEVELOPMENT DIVISION

R. D. Simmons
Contract Administration

RDS:bw

cc: NAVPRO/LMSC w/encl (1) (1 cy)

Director, Naval Research Laboratory
Attn: Code 2627
Washington, DC 20375 w/encl (1) (6 cys)

Defense Documentation Center
Bldg. 5, Cameron Center
Alexandria, Virginia 22314 w/encl (1) (12 copies)

Office of Naval Research - Branch Office
1030 E. Green Street
Pasadena, CA 91106 w/encl (1) (1 cy)

Supplemental Distribution List (attached) w/encl (1) (1 cy each)

RE/431/82/174

SUPPLEMENTARY DISTRIBUTION LIST

Technical and Summary

December 1982

Professor G. J. Abbaschian
University of Florida
Metallurgy and Materials Science
Gainesville, FL 32611

Professor G. A. Ansell
Rensselaer Polytechnic Institute
Troy, NY 02181

Dr. O. Arora
David W. Taylor Naval Ship
Research and Development Center
Code 2813
Annapolis, MD 21402

Professor R. J. Arsenault
University of Maryland
Department of Materials Engineering
College Park MD 20742

Professor D. G. Ast
Cornell University
Department of Materials Science and
Engineering
Ithaca, NY 14853

Dr. J. J. Becker
Corporate Research and Development
General Electric Company
Schenectady,NY 12301

Dr. K. J.Bhansali
National Bureau of Standards
Metallurgy Division
Washington, DC 20234

Dr. N. S. Bornstein
United Technologies Research Center
East Hartford, CT 06108

Dr. R. G. Bourdeau M26
Pratt & Whitney Aircraft Group
Government Products Division
P.O. Box 2691
West Palm Beach, FL 33402

Dr. H. H. Chaskelis
Naval Research Laboratory
Code 5834
Washington, DC 20375

Dr. A. E. Clark
Naval Surface Weapons Center
White Oak Laboratory - Code R45
Silver Spring, MD 20910

Professor J. B. Cohen
Northwestern University
Dept. of Materials Sciences
Evanston, IL 60201

Professor M. Cohen
Massachusetts Institute of Technology
Department of Metallurgy
Cambridge, MA 02139

Dr. S. A. David
Oak Ridge National Laboratory
Metals and Ceramics Division
Oak Ridge, TN 37830

Professor Thomas W. Eagar
Massachusetts Institute of Technology
Department of Materials Science
and Engineering
Cambridge, MA 02139

Professor G. R. Edwards
Colorado School of Mines
Department of Metallurgical
Engineering
Golden, CO 80401

Dr. W. A. Ernst
Westinghouse R&D Center
Structural Materials Department
1310 Beulah Road
Pittsburgh, PA 15235

Professor B. C. Giessen
Northeastern University
Department of Chemistry
Boston, MA 02115

Professor Karl Graff
Ohio State University
Dept. of Welding Engineering
190 West 19th Avenue
Columbus, OH 43210

Professor C. D. Graham
University of Pennsylvania
Dept. Materials Science & Eng.
3451 Walnut Street
Philadelphia, PA 19104

Mr. C. L. Hoffman
Naval Research Laboratory
Material Science and Technology Division
Alloy Transformations Branch
Washington, DC 20375

Dr. S. Huang
General Electric Company
Corporate R&D
Schenectady, NY 12301

Dr. D. F. Keaney
Charles Stark Draper Laboratory
555 Technology Square
Cambridge, MA 02139

Professor D. A. Koss
Michigan Technological University
College of Metallurgical Engineering
Houghton, MI 49931

Dr. I. R. Kramer
University of Maryland
Department of Materials Engineering
College Park, MD 20742

Professor A. Lawley
Drexel University
Department of Metallurgical Engineering
Philadelphia, PA 19104

Dr. G. R. Leverant
Southwest Research Institute
8500 Culebra Road
P.O. Box 28510
San Antonio, TX 78284

Mr. R. E. Lewis
Lockheed Missiles and Space Co.
Lockheed Palo Alto Research
Palo Alto CA 94304

Dr. C. T. Liu
Oak Ridge National Laboratory
P.O. Box X
Oak Ridge, TN 37830

Dr. W. E. Lukens
DTNSRDC
Code 2811
Annapolis, MD 21402

Professor Harris Marcus
The University of Texas at Austin
College of Engineering
Austin, TX 78712

Professor H. Margolin
Polytechnic Institute of New York
333 Jay Street
Brooklyn, NY 11201

Dr. H. Mishler
Battelle Columbus Labs
505 King Avenue
Columbus, OH 43201

Mr. M. S. Misra
Martin Marietta Aerospace
P.O. Box 179
Denver, CO 80201

Professor C. E. Mobley
Ohio State University
Dept. Metallurgical Engineering
Columbus, OH 43212

Professor K. Mukherjee
Michigan State University
Department of Metallurgy
East Lansing, MI 48824

Dr. R. S. Polvani
National Bureau of Standards
Fracture and Deformation Div.
Washington, DC 20234

Mr. A. Pollack
Naval Ships Research & Development
Code 2821
Annapolis, MD 21042

Professor G. W. Powell
Ohio State University
Department of Metallurgical Engineering
Columbus, OH 43210

Dr. B. B. Rath
Naval Research Laboratory Code 6300
Material Science and Technology Division
Washington, DC 20375

Professor D. R. Sadoway
Massachusetts Institute of Technology
Materials Processing Center
Cambridge, MA 02139

Professor O. D. Sherby
Stanford University
Materials Sciences Division
Stanford, CA 94300

Dr. D. B. Snow
United Technology Corporation
United Technology Research Laboratories
East Hartford, CT 06108

Professor E. H. Starke
University of Virginia
Department of Materials Science
Charlottesville, VA 22901

Professor P. R. Strutt
University of Connecticut
School of Engineering
Department of Metallurgy
Storrs, CT 06268

Professor J. K. Tien
Columbia University
Henry Krumb School of Mines
New York, NY 10027

Professor D. Turnbull
Harvard University
Division of Engineering and
Applied Physics
Cambridge, MA 02138

Professor J. B. Vander Sande
Massachusetts Institute of Technology
Department of Materials Science
Cambridge, MA 02139

Dr. R. M. Waterstrat
American Dental Association
National Bureau of Standards
Washington, DC 20239

Dr. S. H. Whang
Northeastern University-341 MV
Institute of Chemical Analysis
Boston, MA 02115

Dr. J. C. Williams
Carnegie-Mellon University
Department of Metallurgy and
Materials Sciences
Schenley Park
Pittsburgh, PA 15213

Professor H. G. F. Wilsdorf
University of Virginia
School of Engineering and
Applied Sciences
Charlottesville, VA 22903

LMSC-F108004

METALLURGICAL INVESTIGATION OF HOT DUCTILITY LOSS IN Ti-6211 ALLOY

R. E. Lewis
Lockheed Palo Alto Research Laboratory
3251 Hanover Street
Palo Alto, California 94304

January 1986

Final Technical Report for Period June 1979 to January 1986
Contract N004-79-C-0449

Approved for Public Release; Distribution unlimited

Sponsored by:
OFFICE OF NAVAL RESEARCH
Arlington, Virginia 22209

UNCLASSIFIED

SECURITY CLASSIFICATION OF THIS PAGE

REPORT DOCUMENTATION PAGE

Form Approved OMB No. 0704-0188

1a. REPORT SECURITY CLASSIFICATION UNCLASSIFIED	1b. RESTRICTIVE MARKINGS DISTRIBUTION UNLIMITED
2a. SECURITY CLASSIFICATION AUTHORITY	3. DISTRIBUTION/AVAILABILITY OF REPORT
2b. DECLASSIFICATION/DOWNGRADING SCHEDULE	
4. PERFORMING ORGANIZATION REPORT NUMBER(S) LMSC-F108004	5. MONITORING ORGANIZATION REPORT NUMBER(S)
6a. NAME OF PERFORMING ORGANIZATION Metallurgy Laboratory, R&DD LMSC, Inc.	6b. OFFICE SYMBOL (If applicable) / 7a. NAME OF MONITORING ORGANIZATION
6c. ADDRESS (City, State, and ZIP Code) 3251 Hanover Street Palo Alto, CA 94304	7b. ADDRESS (City, State, and ZIP Code)
8a. NAME OF FUNDING/SPONSORING ORGANIZATION Office of Naval Research	8b. OFFICE SYMBOL (If applicable) ONR / 9. PROCUREMENT INSTRUMENT IDENTIFICATION NUMBER N00014-79-C-0449
8c. ADDRESS (City, State, and ZIP Code) Materials Science Division 800 N. Quincy Street Arlington, VA 22217	10. SOURCE OF FUNDING NUMBERS PROGRAM ELEMENT NO. / PROJECT NO. / TASK NO. / WORK UNIT ACCESSION NO.

11. TITLE (Include Security Classification)
Metallurgical Investigation of Hot Ductility Loss in Ti-6211 Alloy

12. PERSONAL AUTHOR(S)
R. E. Lewis

13a. TYPE OF REPORT	13b. TIME COVERED	14. DATE OF REPORT (Year, Month, Day)	15. PAGE COUNT
Final	FROM 6/79 TO 1/86	1986 January 15	206

16. SUPPLEMENTARY NOTATION

17. COSATI CODES			18. SUBJECT TERMS (Continue on reverse if necessary and identify by block number)		
FIELD	GROUP	SUB-GROUP	Ti-6211 Alloy	Phase Transformations	Embrittlement
			Titanium	Hot Ductility	Intergranular Cracking
			α-β Alloys	Hot Ductility Loss	(Cont. on reverse)

19. ABSTRACT (Continue on reverse if necessary and identify by block number)

A preliminary metallurgical investigation of the hot ductility dip phenomenon in the Ti-6211 alloy was conducted by LMSC. The main characteristic of this phenomenon is a low (0 to 20 percent) reduction in area of hot ductility specimens which are thermally cycled to about 1649°C (3000°F) and broken in tension on cooling to between 760 and 843°C (1400 and 1550°F). Low hot ductility is also exhibited by specimens from weld metal on heating directly to 760 to 843°C (1400 to 1550°F). The metallurgical investigation included fractographic and microstructural examination of a number of tested hot

(Cont. on reverse)

20. DISTRIBUTION/AVAILABILITY OF ABSTRACT	21. ABSTRACT SECURITY CLASSIFICATION
☒ UNCLASSIFIED/UNLIMITED ☐ SAME AS RPT ☐ DTIC USERS	UNCLASSIFIED
22a. NAME OF RESPONSIBLE INDIVIDUAL Dr. Bruce A. McDonald	22b. TELEPHONE (Include Area Code) (202)696-4402 / 22c. OFFICE SYMBOL ONR

DD Form 1473, JUN 86 *Previous editions are obsolete.*

SECURITY CLASSIFICATION OF THIS PAGE

UNCLASSIFIED

18.

Metallography
Optical Microscopy
Transmission Electron Microscopy
Scanning Electron Microscopy
Fractography

Simulated Weld Thermal Cycles
Gleeble
Sulfur Segregation
Yttrium, Effect of
Phase Transformations
Massive Transformations
Martensite
Widmanstatten $\alpha + \beta$

19.

ductility specimens supplied by DTNSRDC-Annapolis, representing weld thermal cycles in 5.08-cm. (2-in.) thick, β-processed plate, weld fusion zone, and 15.2- x 15.2- cm (6- x 6-in.) castings of Ti-6211. Also included were thermally cycled specimens of Ti-6Al and Ti-50, a commercial purity alloy. This examination showed that intergranular fracture along prior β-grain boundaries was predominant in specimens exhibiting the low hot ductility. Intergranular fracture appears to occur as the result of microvoid nucleation and coalescence at the edge of or near the edge of the grain boundary α layer present in the prior β-grain boundary. Transmission electron microscopy revealed in one case a chain of small precipitates in this location; these disks are about 24 nm thick and spaced about 50 nm apart. Microprobe examination of sections through the boundaries did not reveal any significant local concentration of elemental species.

Auger electron spectroscopy (AES) of an apparent prior β-grain boundary on the fracture surface of a Ti-6211 β-processed plate specimen revealed a concentration of sulfur of 0.47 atomic percent, over 300 times higher than the base metal concentration. This fracture surface was obtained by testing in-situ in the AES chamber at about -149°C (-300°F), the specimen having been previously thermally cycled from RT to 1629°C (2965°F), control cooled to 829°C (1525°F), and water quenched. The possibility of embrittlement from sulfur diffusing to β-grain boundaries during certain elevated temperature cycles may be related to the well-known sulfur embrittlement phenomenon in alloy steels and other metals. If the hot ductility dip phenomenon is caused by sulfur concentration at the β-grain boundaries, then a relationship may exist between the observed weld thermal cycle low ductility and cracking during certain hot forming operations.

FOREWORD

This Final Technical Report was prepared by Lockheed Missiles and Space Company, Inc., Research and Development Division, Palo Alto, California, under ONR Contract N0004-79-C-0449. The work was sponsored by the Office of Naval Research, Arlington, Virginia, with Dr. B. A. MacDonald as Program Manager.

This report covers the period June 1979 to 15 January 1986 for the program to investigate factors affecting elevated temperature fracture of the Ti-6Al-1Nb-1Ta-0.8Mo alloy, particularly the hot ductility loss in the alloy as related to weld thermal cycles in thick plate weldments.

Mr. R. E. Lewis, the Principal Investigator on the program, was assisted by Dr. A. Joshi, LMSC, for surface analysis and by Mr. W. C. Coons, consultant, San Jose, for optical metallography. In addition, electron microscope studies were performed in collaboration with Dr. V. A. Phillips, LMSC (now with United Technologies Research Center), and with J. C. Williams and Mr. G. K. Scarr, Carnegie-Mellon University. Valuable guidance was provided by Mr. I. L. Caplan, David W. Taylor Naval Ship Research and Development Center - Annapolis, who proposed the original research topic and provided useful background information and discussion of the experimental results. He also arranged for support by the U.S. Navy (DTNSRDC) to conduct high speed time-temperature cycling of "Gleeble" specimens. Useful discussions on various technical aspects of the program were also provided by Mr. J. Cavallaro and Dr. W. E. Lukens, David W. Taylor Naval Ship Research and Development Center-Annapolis.

CONTENTS

CONTENTS (Cont.)

CONTENTS (Cont.)

ILLUSTRATIONS

ILLUSTRATIONS (Cont.)

ILLUSTRATIONS (Cont.)

ILLUSTRATIONS (Cont.)

ILLUSTRATIONS (Cont.)

TABLES

Section 1
INTRODUCTION AND BACKGROUND

1.1 INTRODUCTION

The Ti-6Al-2Nb-1Ta-0.8Mo (Ti-6211) alloy has been developed for advanced naval applications requiring thick-section products (plate, forgings, weldments). Weldability studies in the development of this alloy have been necessary to identify fabrication requirements and to establish mechanical property properties affecting service life.

Two different types of preliminary weldability studies were performed by the David W. Taylor Naval Ship Research and Development Center - Annapolis (DTNSRDC-Annapolis). These were (a) mechanical and metallurgical evaluation of weldments of a variety of joint designs and thicknesses and (b) synthetic weld heat-affected zone studies involving a special high speed, programmable thermal cycling apparatus (the "Gleeble").

In these studies, cracks were observed in some weldments (Ref. 1). These cracks were transgranular, and were believed to be caused by contamination in the welding process and tensile stresses caused by the high elastic constraint. However, such cracking was rather isolated and was difficult to duplicate. Hot ductility tests conducted with the Gleeble showed that the material consistently exhibits low ductility between 760 and 843°C (1400 and 1550°F) on cooling from 1565 to 1649°C (2850 to 3000°) (Refs. 2,3). The thermal cycle simulated is the near heat-affected zone, within 0.254 mm (0.010 in.) from the edge of the fusion zone. This low tensile ductility is likely to be an indication of the materials' propensity to form hot cracks during the welding process and/or during hot working of the alloy. It is important to establish whether such relationships exist.

An understanding of the hot ductility loss may be of major importance in the use of the Ti-6211 alloy, as resistance to cracking in weld fabrication or hot working is always considered a significant asset. Conversely, identification of factors causing or contributing to the hot ductility loss is necessary for development of improvements in the alloy or weld processes, if such improvements are required for important marine applications.

A preliminary investigation of microstructures and metallurgical factors associated with the observed hot ductility loss was conducted by the Lockheed Missiles & Space Co., Inc. (LMSC) for the David W. Taylor Naval Ship Research and Development Center in the 1977-1978 period. This study was to provide useful background for work proposed subsequently in November 1978 to the Office of Naval Research (ONR). The following is the report of the preliminary investigation.

1.2 BACKGROUND

1.2.1 Abstract

In a preliminary metallurgical investigation of the alloy Ti-6211 by LMSC, reduction of area, or a measure of ductility, was measured as a function of break temperature. A diminished ductility in the plotted results is referred to as the hot ductility dip, illustrated in Fig. 1. The main characteristic of this phenomenon is a low (0 to 20 percent) reduction in area of hot ductility specimens which are thermally cycled to about 1649°C (3000°F) and broken in tension on cooling to between 760 and 843°C (1400 and 1550°F). Low hot ductility is also exhibited by specimens from weld metal on heating directly to 760 to 843°C (1400 to 1550°F). The metallurgical investigation included fractographic and microstructural examination of a number of tested hot ductility specimens supplied by DTNSRDC-Annapolis, representing weld thermal cycles in 5.08-cm. (2-in.) thick, β-processed plate, weld fusion zone, and 15.2- x 15.2- cm (6- x 6-in.) castings of Ti-6211. Also included were

thermally cycled specimens of Ti-6Al and Ti-50, a commercial purity alloy. This examination showed that in specimens exhibiting the low hot ductility, intergranular fracture along prior β-grain boundaries was predominant. Intergranular fracture appears to occur as the result of microvoid nucleation and coalescence at the edge of or near the edge of the grain boundary α layer present in tne prior β-grain boundary. Transmission electron microscopy revealed, in one case, a chain of disk-shaped precipitates in this location; they were about 24 nm thick and spaced about 50 nm apart. Microprobe examination of sections through the boundaries did not reveal any significant local concentration of elemental species.

Auger electron spectroscopy (AES) of an apparent prior β-grain boundary on the fracture surface of a Ti-6211 β-processed plate specimen revealed a concentration of sulfur of 0.47 atomic percent, over 300 times higher than the base metal concentration. This fracture surface was obtained by testing in-situ in the AES chamber at about -149°C (-300°F), the specimen having been previously thermally cycled from RT to 1629°C (2965°F), control cooled to 829°C (1525°F) and water quenched. The possibility of embrittlement from sulfur diffusing to β-grain boundaries during certain elevated temperature cycles may be related to the well known sulfur embrittlement phenomenon in alloy steels and other metals. If the hot ductility dip phenomenon is caused by sulfur concentration at the β-grain boundaries, then a relationship may exist between the observed weld thermal cycle low ductility and cracking during certain hot forming operations.

1.2.2 DTNSRDC-Annapolis Test Results

Results of hot ductility tests conducted previously by DTNSRDC-Annapolis revealed a number of conditions which promote low tensile ductility (low reduction in area) in Ti-6211 base metal and weldments (Ref. 3). The major factor identified so far is thermal cycling to a peak temperature between 1093 and 1649°C (2000 and 3000°F), followed by cooling to between 760 and 843°C (1400 and 1550°F) and stressing in tension. Figure 1 illustrates that the ductility dip occurs in alloys other than Ti-6211 when thermally cycled the same way (Ref. 3). The hot ductility dip in Ti-6Al-4V is similar to that in

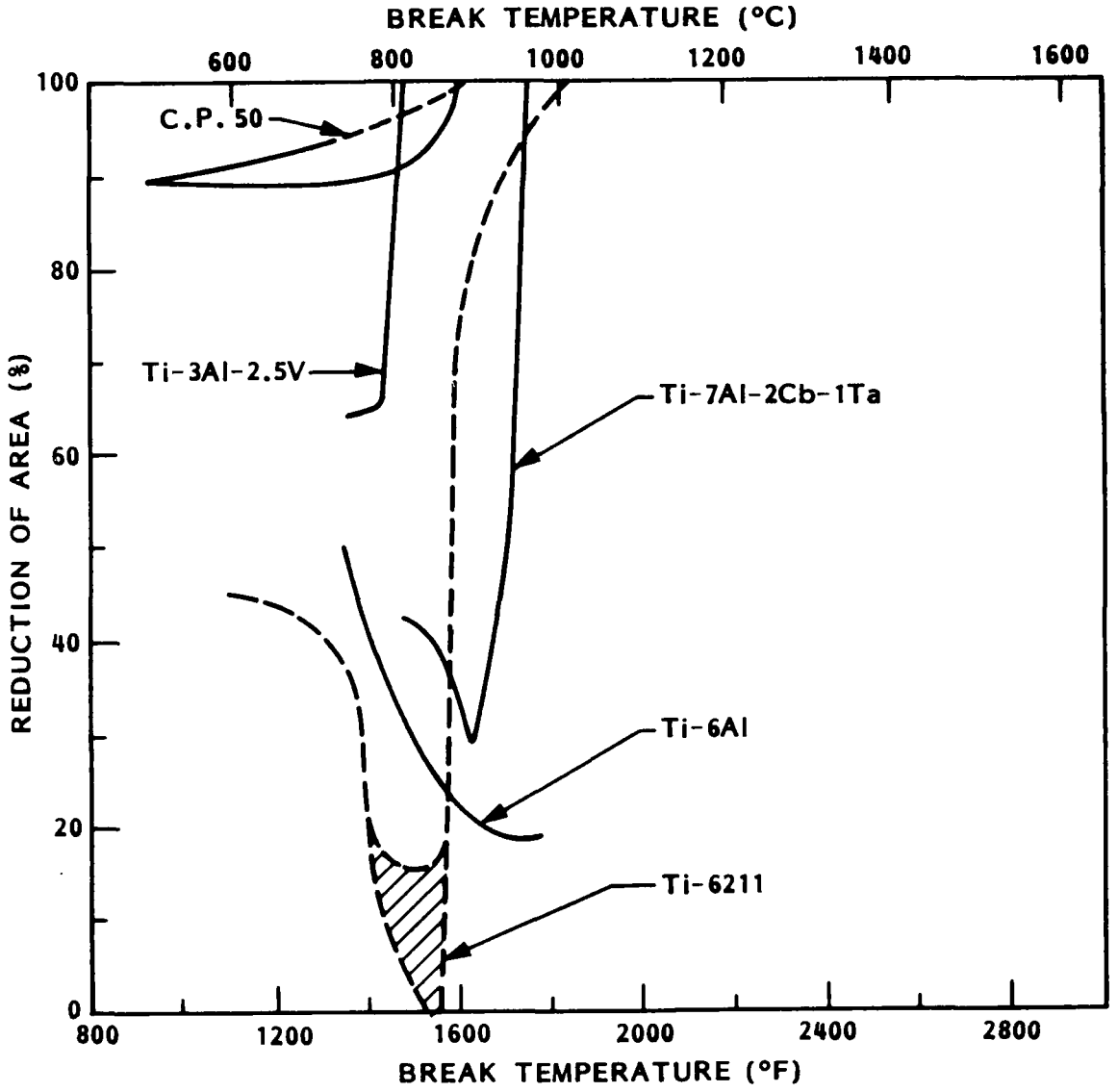

Fig. 1 Hot Ductility of Selected Composition Titanium Alloys Including Ti-50 (Commercial Purity). Reduction of area measured on cooling from 1538-1649°C (2800-3000°F) peak temperature simulated weld thermal cycle

Ti-6211 but the minimum ductility occurs at a slightly lower temperature (Ref. 3). As shown in Fig. 1, a significant ductility dip occurs in both Ti-6Al and Ti-7Al-2Cb-1Ta. A modest dip is shown for Ti-3Al-2.5V and essentially no dip occurs in commercially pure Ti-50. These data are for a simulated weld thermal cycle representing 1538-1649°C (2800-3000°F) peak temperature and 24-KJ weld energy input in 5.08-cm (2-in.) plate and with no preheat.

Such thermal cycles are reported by one investigator to also reduce the room temperature [21°C (70°F)] and 0°C (32°F) Charpy impact energy of Ti-6211 (Ref. 2). The low impact toughness was associated with fracture along prior β grain boundaries, and the microfractographic mode was ductile rupture. Thus, low energy grain boundary ductile rupture may occur as the result of a high temperature weld thermal cycle. The same investigator found that variations in cooling rate from a 1316°C (2400°F) peak temperature had no appreciable effect on the room temperature impact energy.

Some other factors previously investigated (Ref. 3) by DTNSRDC-Annapolis regarding possible correlation with the Ti-6211 hot ductility dip as shown in Fig. 1 are as follows.

(a) Effect of Microstructure. Both β-processed and α+β processed plates were found to exhibit the same hot ductility behavior. The size and amount of the α platelets and the "blockiness" of the platelet colonies was found to have a negligible effect on hot ductility.

(b) Effect of Molybdenum. Ti-6Al-0.8Mo was found to exhibit almost the same hot ductility dip as Ti-6211. Ti-6Al exhibits a hot ductility dip which is characterized by a higher minimum ductility (20 percent compared to 8 percent RA) and a higher break temperature at minimum ductility [927°C (1700°F) compared to 843°C (1550°F)], when related to Ti-6Al-0.8Mo. Ti-6Al-2.5Mo exhibited a hot ductility dip shifted to much lower temperatures than either of the above alloys [538°C (1000°F) compared to 843 and 927°C (1550°F and 1700°F)], and a higher reduction in area (~ 30 percent). These results do not indicate that molybdenum is responsible for the dip in hot ductility, but that the dip occurs below the β-transus on cooling,

and increased molybdenum content therefore lowers the temperature at which a minimum ductility is observed.

(c) Effect of Oxygen. Two different oxygen contents for both Ti-6211 and Ti-6Al-4V alloys were investigated, and no apparent correlation was observed between oxygen content and the hot ductility dip.

(d) Effect of Yttria Modification. Both 50 and 150 ppm Y_2O_3 levels in Ti-6211 were investigated. Hot ductility over the 760 to 871°C (1400 to 1600°F) temperature range on both heating and cooling were the same for both Y_2O_3 contents.

(e) Casting vs. Wrought Plate. Ti-6211 thick-section castings were found to exhibit a hot ductility dip at the same break temperature on cooling from 1613-1648°C (2935-3000°F) peak as exhibited by 5.08-cm (2-in.) thick β-processed plate, but the minimum reduction in area was higher in the castings then the plate (30 to 55 versus 0 to 15 percent, respectively). Apparently the much coarser β-grain size of the former favors a higher reduction in area in the low ductility temperature region. The minimum hot ductility occurs at the same temperature because the composition is the same and consequently the β-transus is the same.

(f) Effect of Peak Temperatures and Hold Times. Heating to any peak temperature between 1204 and 1621°C (2200 and 2950°F) has about the same effect on reduction in area of specimens broken on cooling to between 760 and 843°C (1400 and 1550°F). When the peak temperature is only 1093°C (2000°F), a somewhat higher hot ductility is exhibited (about 40 percent RA compared to 8 to 32 percent RA for the higher range of peak temperature). Holding for 30 s at peak temperature of 1316 or 1621°C (2400 or 2200°F) has the effect of further reducing hot ductility a small amount.

(g) Weldments vs. Plate. Hot ductility on heating to a break temperature of 760-843°C (1400-1550°F) is much lower in weldments than β-processed plate, 5.08 cm (2-in.) thick (19 to 28 and 50 to 65 percent RA, respectively). Apparently, the embrittling factor is present in the weldments before thermal cycling in the Gleeble, and is not present in the plate product until cycled to above 1621°C

(2200°F). The above observations suggest that either an actual or simulated weld thermal cycle is required to produce the low hot ductility observed in the 760-843°C (1400-1550°F) temperature range. In the case of weldments, this low ductility is exhibited either on heating or on cooling. In contrast, low ductility of plate product is exhibited only on cooling from between 1621 and 1649°C (2200°F and 3000°F). Hold times at peak temperature affects hot ductility. Because failure along prior β-grain boundaries is the preferential fracture path for specimens tested in the temperature range of the hot ductility dip, diffusion in or adjacent to the prior β-grain boundaries may be a contributing factor affecting the hot ductility dip.

A detailed, yet exploratory, investigation of microstructures and elemental concentration in the region adjacent to prior β-grain boundaries was then undertaken by LMSC. This study, described in the next two subsections, was an initial effort to identify factors contributing to or controlling the hot ductility dip in Ti-6211.

1.2.3 Preliminary Study by LMSC

1.2.3.1 Approach.

Selected synthetic weld heat-affected zone hot ductility test specimens supplied by DTNSRDC-Annapolis were analyzed by light optical, transmission electron, and scanning electron microscopy. Elemental species on fracture surfaces and sections through the microstructure were examined by energy dispersive analysis in the SEM and Auger electron spectroscopy in a high resolution scanning Auger microscope (SAM). Particular attention was given to the analysis of phases, particles, and elemental concentration at prior β-grain boundaries and on fracture surfaces.

A few samples of both Ti-6211 and Ti-3Al-2.5V alloys were obtained from DTNSRDC-Annapolis in the thermal cycled condition known to produce low hot ductility, but were untested. These samples were machined into notched round

bars, and broken by bending at -184°C (-300°F) in the SAM and the fracture surfaces examined insitu by AES.

An analysis of the results was undertaken with the goal of identifying those factors possibly controlling the hot ductility dip.

1.2.3.2 Results and Discussion

Examination of the Hot Ductility Data. Results of hot ductility tests conducted previously by DTNSRDC-Annapolis reveal a number of conditions in which a low tensile ductility (low reduction in area) is exhibited by Ti-6211 base metal and weldments. Specimens representing a number of these conditions were selected for preliminary metallurgical examination and are listed in Table 1. Fracture was induced by a moderately high strain rate tensile load on heating or on cooling during a simulated weld heat-affected zone thermal cycle. This cycle has a 1621°C (2950°F) nominal peak temperature as measured in a 5.08-cm- (2-in.-) thick titanium weldment, 24-kJ energy input, and no preheat.

The following general statements can be made regarding the data in Table 1.

- Ti-6211 β-processed 5.08-cm (2-in.) plate exhibits a low ductility (reduction in area of less than 20 percent) when broken on cooling to 760-816°C (1400-1500°F) after heating either to 1649°C (3000°F) with no hold time or to 1316°C (2400°F) with a 30-s hold time (compare EYL-1797 with EYL-2003)
- Ti-6211 plate, weldment, and casting and Ti-6Al plate all exhibit the hot ductility dip when broken on cooling (compare EYL-1797 with EYL-9, FEP-4 and EJT-7)
- Ti-6211 weldment exhibits a low ductility on heating to 843°C (1550°F), whereas 5.08-cm (2-in.) β-processed plate exhibits a relatively high ductility (compare EYL-24 with EYL-2000)
- Ti-6211 plate exhibits a low ductility when broken on heating to 821°C (1510°F) after thermal cycling from RT to 1621°C (2950°F) to RT, but

exhibits a relatively high ductility if broken on heating in the first cycle (compare EYL-2011 with EYL-2000)

- Commercially pure titanium doesn't exhibit the ductility dip on cooling (see EYB-2)

Table 1 HOT DUCTILITY SPECIMENS EXAMINED AFTER TEST

Spec. No.	Alloy	Product	Thermal Cycle °C(°F)	RA (Percent)
EYL-1797	Ti-6211	β-Processed 5.08-cm (2-in.) plate	RT-1649-821* (RT-3000-1510*)	10
EYL-2000	Ti-6211	β-Processed 5.08-cm (2-in.) plate	RT-838*(RT-1540*)	59
EYL-2011	Ti-6211	β-Processed 5.08-cm (2-in.) plate	RT-1613-RT-821* (RT-2935-RT-1510*)	12
EYL-9	Ti-6211	Weldment in β-Processed 5.08-cm (2-in.) plate	RT-1607-843* (RT-2925-1550*)	21
EYL-24	Ti-6211	"	RT-843*(RT-1550*)	15
FEP-4	Ti-6211	15.24-cm (6-in.) casting	RT-1621-788* (RT-2950-1450*)	36
EJT-7	Ti-6Al	5.08- x 10.6-cm (2-x4-in.) forging	RT-1593-916* (RT-2900-1680*)	21
EYB-2	TI-50	2.54-cm (1-in.) plate	RT-1591-802* (RT-2895-1475*)	90
EYL-2003	Ti-6211	β-Processed 2-in. plate	RT-1316, hold 30s-757* (RT-2400, hold 30s,-1395*)	14

* Break Temperature

Fractographic and Metallographic Examination of Tested Specimens. Supplementary information of the microstructural character of the specimens listed in Table 1 was obtained by metallographic and fractographic examination. These results are as follows:

EYL-1797 - The macroscopic fracture mode of this Ti-6211 plate material, broken at 821°C (1510°F) on cooling from 1649°C (3000°F) is intergranular, as shown in Fig. 2(a) and (b). The microscopic fracture mode is predominantly microvoid nucleation and growth along grain boundaries, with some region of relatively featureless slip. Both of these modes are illustrated in Fig. 2(c).

Some of the microstructural features related to the grain boundary separation are shown in Fig. 3. Surface and subsurface cracking in this hot ductility specimen is predominantly intergranular (Fig. 3a). The intergranular fracture apparently nucleates as microvoids at or near the edge of the grain boundary α (Fig. 3b), which then coalesce to form the grain boundary crack (Fig. 3c). The result is that the grain boundary α is positioned on one side of the fracture and the Widmanstatten structure on the other.

Thus, the low reduction in area (10 percent, see Table 1) is due to microvoid nucleation and coalescence along prior β grain boundaries, resulting in a minimal amount of plastic strain within the prior β grains. If the fracture energy for this material and test sequence were measured it would be very low.

EYL-2000 - This is the same material as EYL-1797, Ti-6211 β-processed, 5.08-cm (2-in.) plate, and the failure is ductile when tested at 838°C (1540°F) on heating. As seen in Fig. 4, significant macroscopic shear is involved in the fracture process, with a minor amount of grain boundary separation. Thus, the predominant fracture mode is transgranular ductile rupture. This is further clarified by microstructural examination of a cross-section through the fracture surface, see Fig. 5. The fracture surface is comprised of a number of relatively large "cusps" (Fig. 5a) with microvoids nucleated in the subsurface at both prior β-grain boundaries and within the α-β platelet microstructure (Fig. 5b).

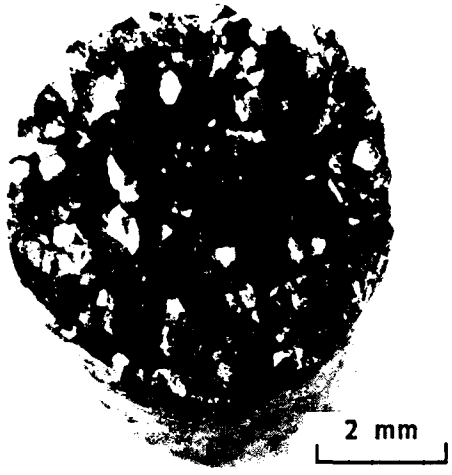

D419 (a)

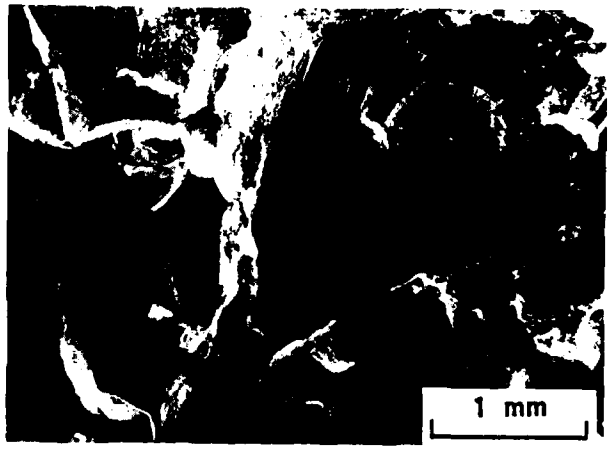

7IED (b)

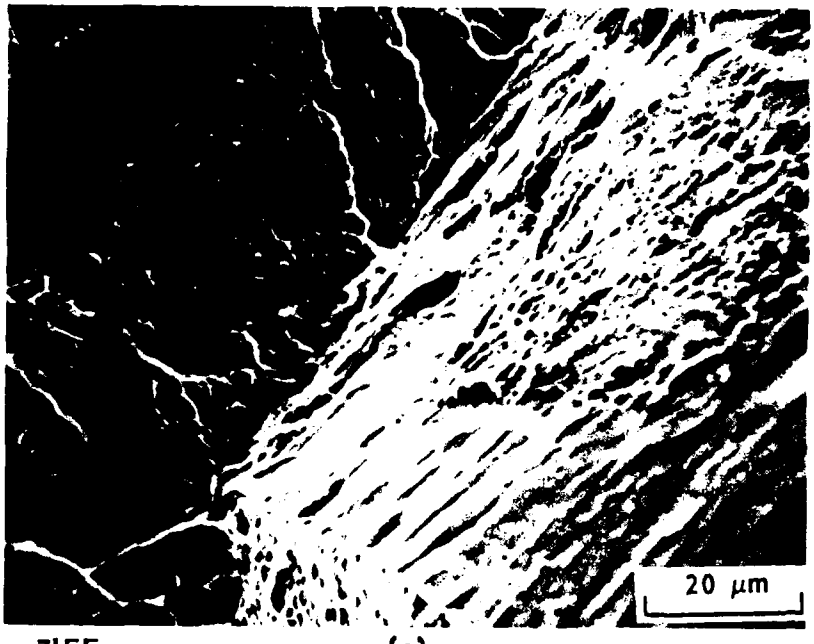

7IEF (c)

Fig. 2 Fracture Appearance of EYL-1797, Ti-6211, β-Processed 5.08-cm (2-in.) Plate. 10 percent RA, broken at 821°C (1510°F) on cooling from 1649°C (3000°F)

Fig. 3 Microstructure of Section Through Specimen EYL-1797 Showing (a) Intergranular Nature of Surface and Subsurface Cracks, (b) Chain of Microvoids Initiating at Boundary of Grain-Boundary α and Widmanstatten α+β, with (c) Crack Formation Along Same Boundary

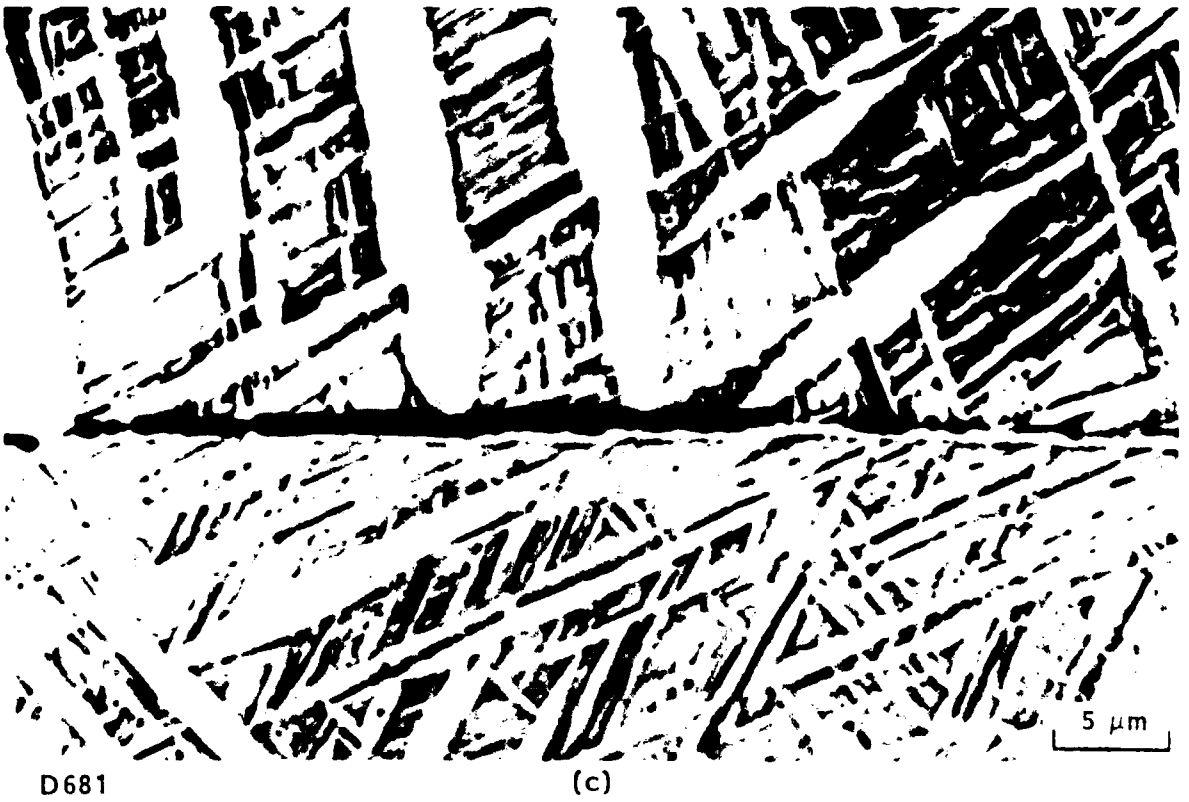

Fig. 3 Cont.

The major difference in microstructural appearance between EYL-2000 and EYL-1797 is in the coarseness of the α-β structure formed by nucleation and growth transformation. This structure is characterized by α platelets separated by thin ribs of β. In the case of EYL 1797, the α platelets vary widely in length and thickness, forming a complex Widmanstatten pattern, see Figs. 3b and c. Coarse α platelets up to 3 μm thick and many fine α platelets are present. Based on transmission electron microscopy, the fine α platelets are between 50 and 20 nm thick, separated by 5-20 nm thick ribs of β. At magnifications up to 100,000 times, the interface phase bracketing some of the β ribs is barely discernable (not illustrated). This microstructure is indicative of relatively high cooling rates in the α-β phase region close to the β transus.

In EYL-2000, the α platelets are significantly coarser than in EYL 1797 and the β ribs with the bordering interface phase are readily discernable, see Figs. 5c and d. Also, the microstructure is more a lamellar array than a

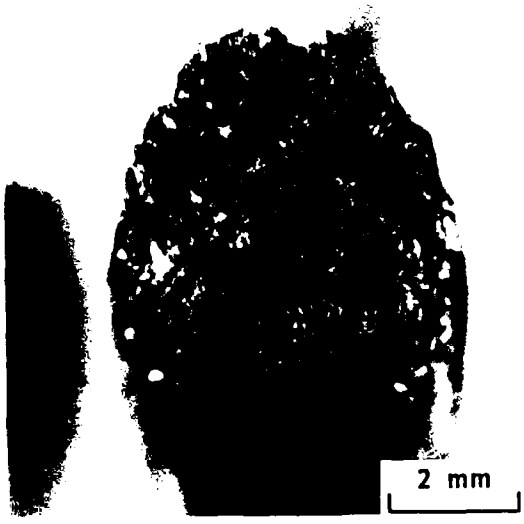

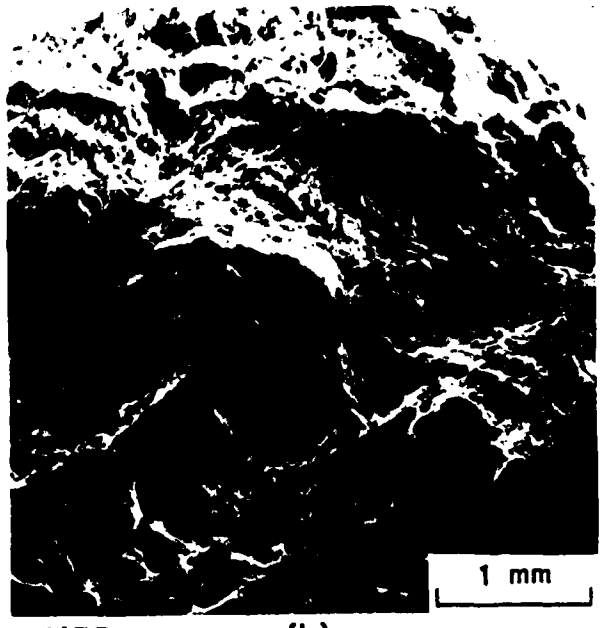

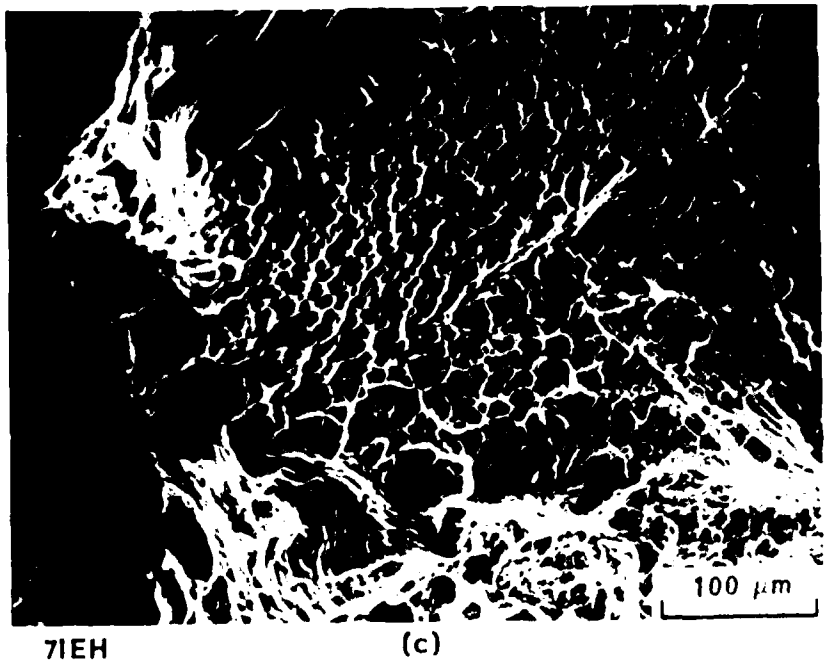

Fig. 4 Fracture Appearance of EYL-2000, Ti-6211, β-Processed 5.08-cm (2-in.) Plate. 59 percent RA, Broken at 838°C (1540°F) on Heating

Fig. 5 Microstructure of Section Through Specimen EYL-2000 Showing (a) Transgranular Ductile Rupture Mode of Fracture, (b) Nucleation of Microvoids Both at Prior β-Grain Boundaries and Within Prior β-Grains, (c) Bright Field TEM of α Platelets Separated by β Rib, and (d) Dark Field TEM of (c) Showing Interface Phase and with Corresponding SAD Inset

J797 (c)

Fig. 5 (Cont.)

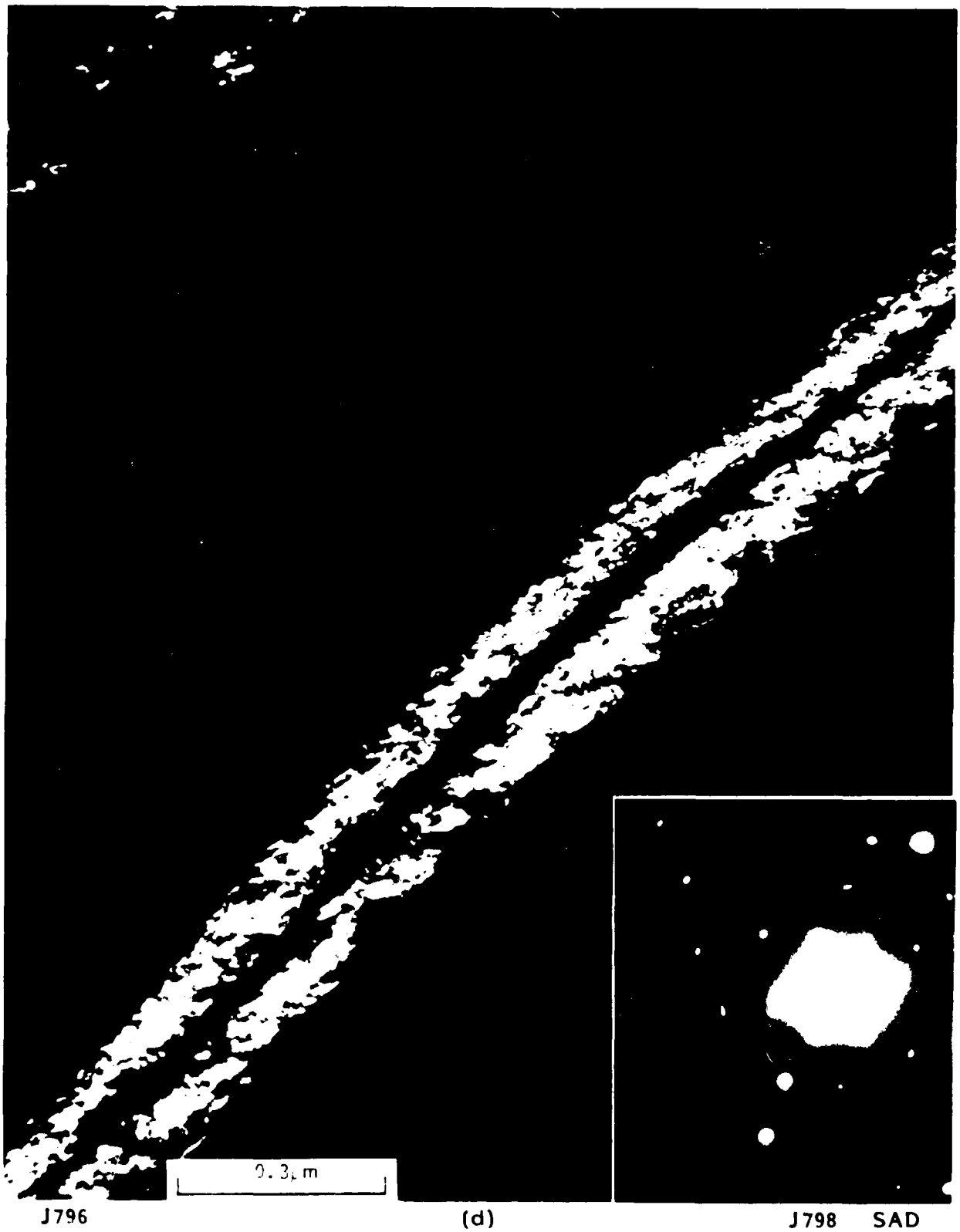

Fig. 5 Cont.

Widmanstatten pattern as in EYL-1797. The character of the interface phase in EYL-2000 is typical of relatively slow cooling rates high in the $\alpha + \beta$ phase region (Refs. 4-7).

EYL-2011 - This specimen was prepared from the same material as EYL-1797 and EYL-2000 but was tested differently. EYL-2011 was heated from RT to 1613°C (2935°F) and cooled back to RT without tensile strain, then tested on reheating to 821°C (1510°F). The hot ductility was low, 12 percent RA. The macroscopic and microscopic fracture modes are shown in Fig. 6 and closely resemble EYL-1797, see Fig. 3. Metallographic examination reveals microstructural features of grain boundary fracture similar to EYL-1797, see Fig. 7. The thermal cycle of heating to 1624°C (2935°F) and cooling to room temperature was apparently sufficient to cause the prior β grain boundaries to be sensitized to tensile strain when fractured upon subsequent reheating to 821°C (1510°F). Not only does the thermal cycle promote fracture along the α layer at prior β grain boundaries, but microvoids and microcracks are formed along some of the thicker α platelets within the grains, see Figs. 7b and c.

Transmission electron microscopy did not reveal any significant differences between EYL-2011 and EYL-1797. The microstructural features were predominantly established by the temperature excursion to 1649°C (3000°F) followed by controlled cooling to room temperature and were not changed significantly during the subsequent reheating to 821°C (1510°F), the break temperature.

EYL-9 - This specimen was prepared from a weldment in 5.08-cm (2-in.), β-processed Ti-6211 plate. The thermal cycle was quite similar to EYL-1797, RT to 1607°C (2925°F) peak temperature, then broken on cooling to 843°C (1550°F). A low hot ductility was exhibited, 21 percent RA. Just like the low hot ductility specimens EYL-1797 and -2011, the predominant fracture mode of EYL-9 is intergranular fracture, see Fig. 8. The microfractographic mode is nucleation of microvoids at prior β-grain boundaries, followed by coalescence leading to grain boundary separation. Metallographic examination shows the presence of subsurface cracks along prior β-grain boundaries, Fig. 9(a), and the serrated nature of the grain boundaries, Fig. 9(b). It is

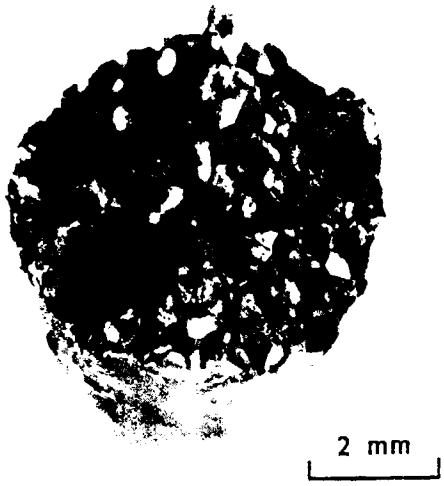

D417 (a)

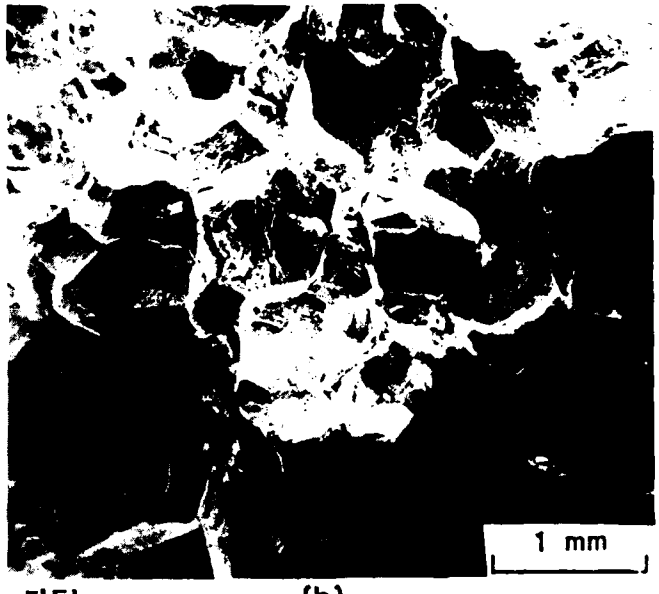

7IEI (b)

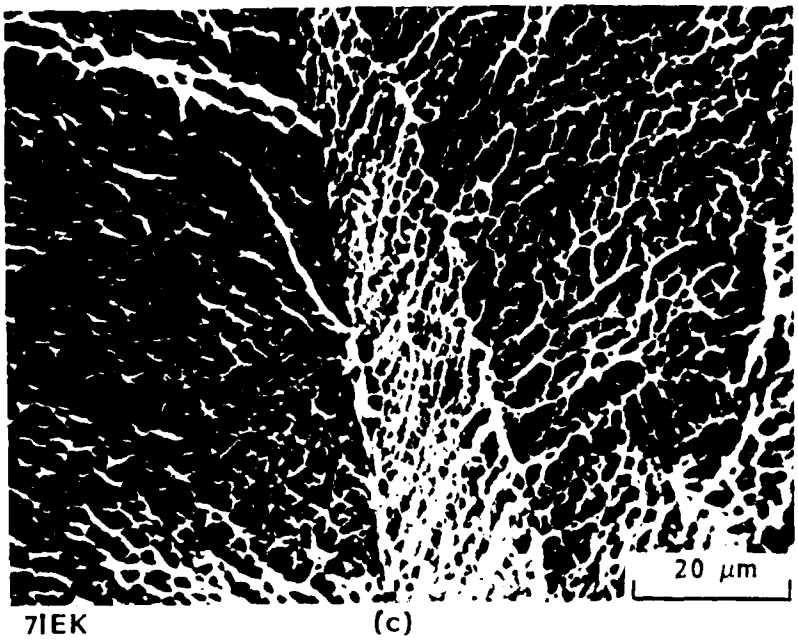

7IEK (c)

Fig. 6 Fracture Appearance of EYL-2011, Ti-6211, β-Processed 5.08-cm. (2-in.) Plate. 12 percent RA, broken on heating to 821°C (1510°F) after prior thermal cycle to 1613°C (2935°F) peak temperature

Fig. 7 Microstructure of Section Through Specimen EYL-2011 Showing Intergranular Nature of Surface and Subsurface Cracking, (b) Nucleation of Microvoids at Both Grain-Boundary α and Coarse Platelets of α and (c) Prevalence of Voids at Boundaries to Form at the Edge of the Grain Boundary α Layer

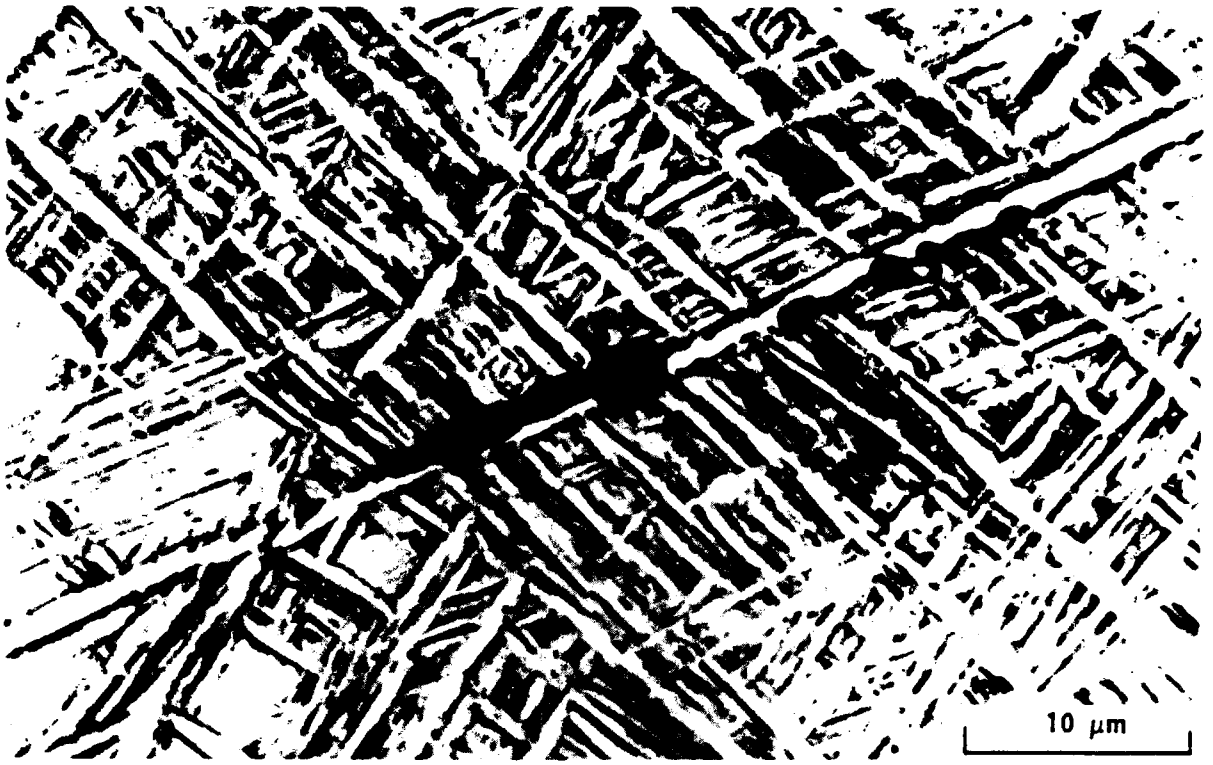

Fig. 7 (Cont.)

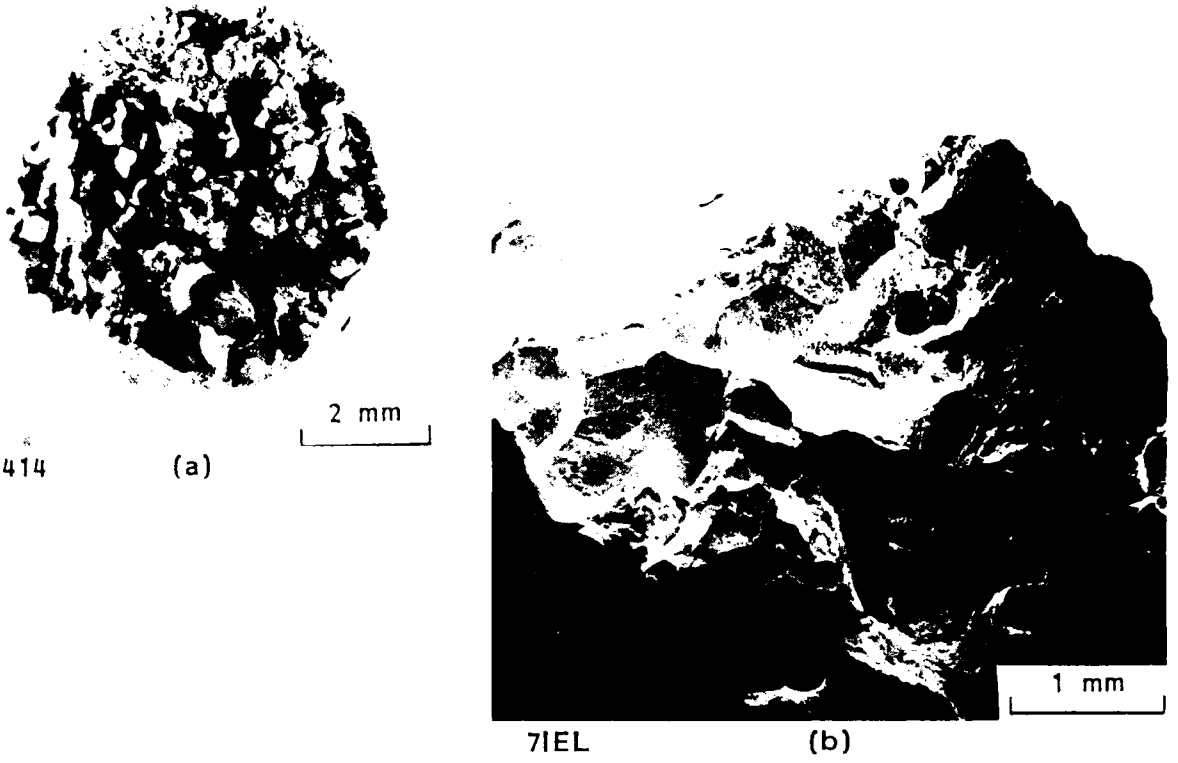

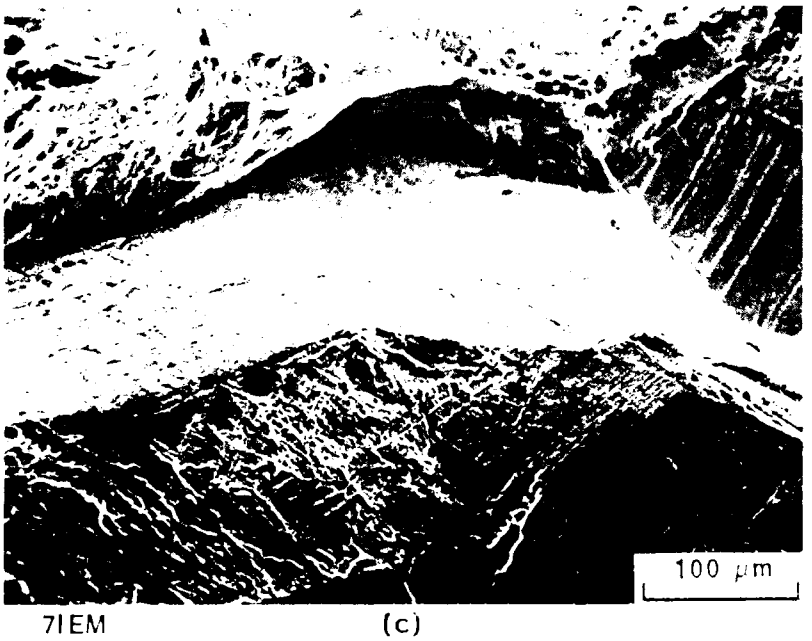

Fig. 8 Fracture Appearance of EYL-9, TIG Weldment in Ti-6211 β-Processed, 5.06-cm (2-in.) Plate. 21 percent RA, broken at 843°C (1550°F) on cooling from 1607°C (2925°F)

Fig. 9 Microstructure of Section Through Specimen EYL-9 Showing (a) Intergranular Nature of Surface and Subsurface Cracking and (b) the Serrated Appearance of the Prior β-Grain Boundaries

not clear whether this serrated feature was caused by the thermal cycle because a sample in the welded and uncycled condition was not available for examination. It is apparent, however, that neither the serration of the boundary nor the thinness of the grain boundary α makes much difference to the degree of sensitization from the thermal cycle effect on EYL-1797.

EJT-7 - This specimen was prepared from a 5.08- x 10.16-cm (2- x 4-in.) forging from a Ti-6Al lab heat weighing 15 kg (33 lb). Low hot ductility (21 percent RA) was exhibited when broken at 916°C (1680°F) on cooling from 1593°C (2900°F). Fractographic features show a mixture of prior β-grain boundary separation and transgranular fracture, see Fig. 10. Because there are no β stabilizers added to this alloy, the microstructure is essentially all α at room temperature. Some scattered platelets of α are present, see Fig. 11(a). The tensile strain in the hot ductility test has nucleated some voids and microcracks below the primary fracture surface, Fig. 11(b). This heterogeneity of void nucleation location may be why the fracture surface shows the mixture of intergranular and transgranular fracture, Fig. 10(c). Apparently the thermal cycle sensitized the grain boundary regions to form cracks at low tensile strain at 916°C (1680°F), and nucleation of voids at other than prior β-grain boundaries has some effect in promoting plastic deformation within the grains. This specimen illustrates the relative unimportance of microstructure within the grains on hot ductility behavior. For example, the Widmanstatten α + β platelet microstructure of EYL 1797 (Figs. 3(b) and (c)) and EYL 9 (Fig. 9(b)) also exhibits low tensile ductility when tested in a similar manner to EJT-7.

EYL-24 - This specimen is from a weldment in β-processed, 5.08-cm (2-in.) Ti-6211 plate. It exhibited low hot ductility at 843°C (1550°F) on heating without any prior synthetic weld thermal cycle. As shown in Fig. 12, the fracture surface shows only a small amount of plastic strain. At low magnification, the fracture features suggest that a relationship to the weld solidification pattern does exist, see Fig. 12(a). At high magnification, the fracture surfaces are shown to be quite flat, and covered with fine microvoids, see Fig. 12(c). Large plastic flow, therefore, was constrained during the fracture process to a narrow region in which microvoids nucleate

2 mm

D420 (a)

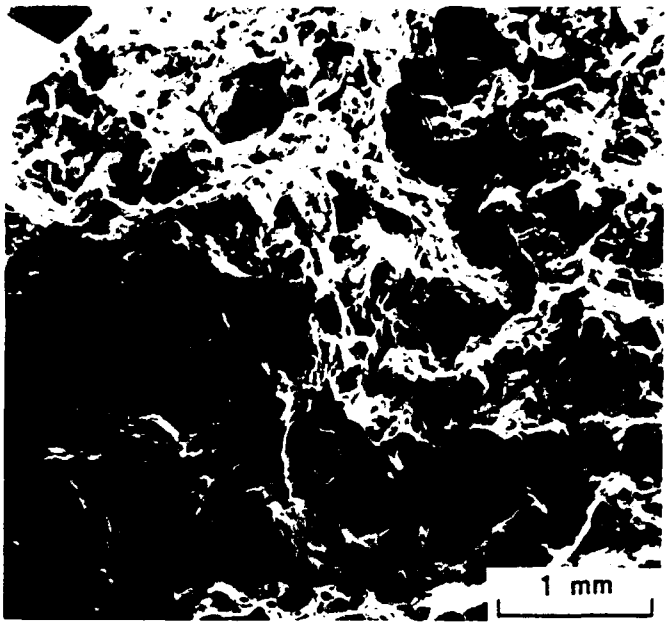

1 mm

7IED (b)

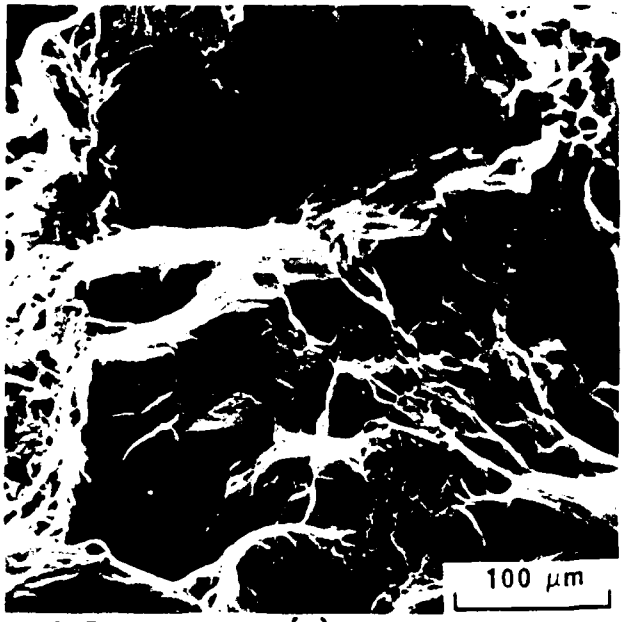

100 μm

7IEP (c)

Fig. 10 Fracture Appearance of EJT-7, Ti-6Al Forging. 21 percent RA, broken at 916°C (1680°F) on cooling from 1593°C (2900°F)

Fig. 11 Microstructure of Section Through Specimen EJT-7 Showing (a) Predominantly Grain Boundary Cracking at both Surface and Subsurface and (b) Region Relatively Devoid of α-β Platelets

D416 (a)

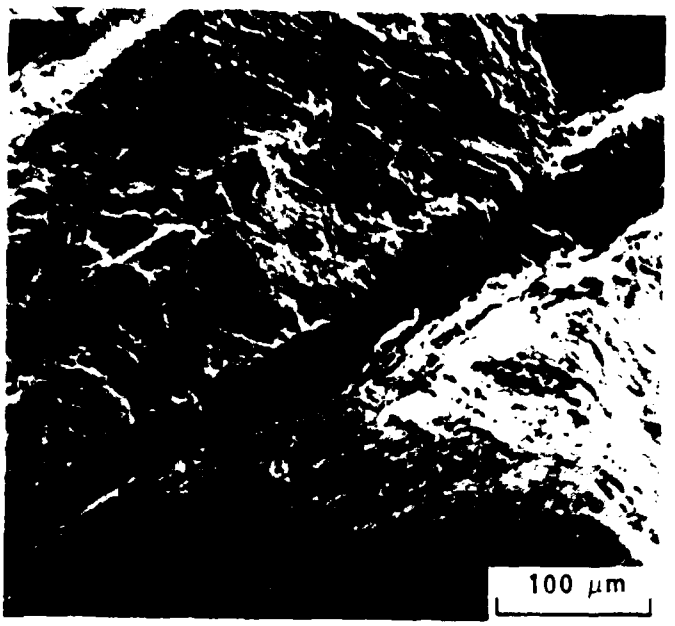

7IET (b)

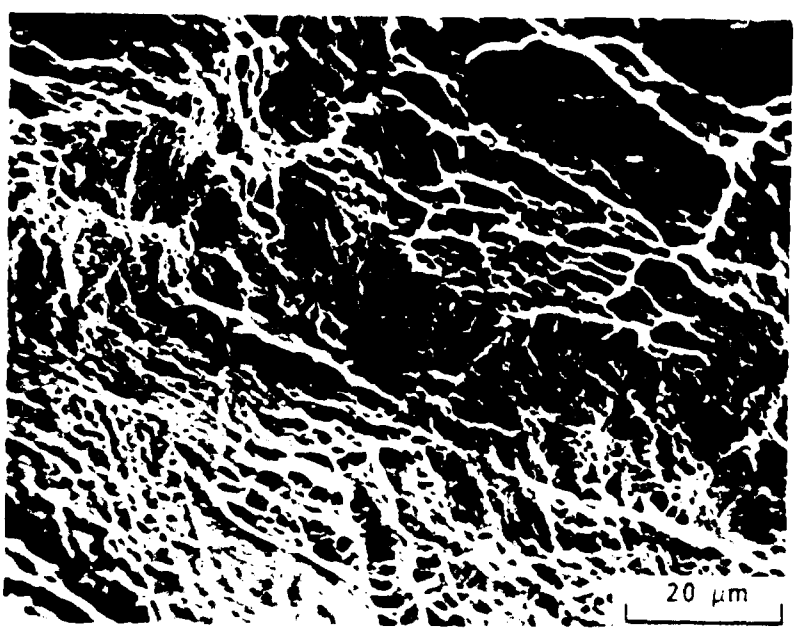

7IEU (c)

Fig. 12 Fracture Appearance of EYL 24, TIG Weldment in Ti-6211 β-Processed, 5.08-cm (2-in.) Plate. 15 percent RA, broken on heating to 843°C (1550°C)

and grow to form the fracture surfaces. No synthetic weld thermal cycle was needed to sensitize this region as the prior weld thermal cycles were apparently adequate. Thus, welds including heat affected zones already existing in a Ti-6211 structure exhibit low tensile ductility on reheating, and not just on cooling as is the case for unwelded base metal.

Metallographic examination of this specimen was not performed so a direct correlation between microstructures and preferred fracture path was not obtained. However, the microstructure of specimen EYL-9 is probably representative, see Figs. 9(a) and (b).

FEP-4 - This specimen is from a 15.2- x 15.2-cm (6- x 6-in.) casting of Ti-6211. A moderate hot ductility (36 percent RA) was exhibited at the break temperature of 788°C (1450°F) on cooling from 1621°C (2950°F). As shown in Fig. 13, the fracture mode is probably intergranular ductile rupture. Although the microscopic fracture mode is similar to the base metal (see, for example, EYL-1797, Fig. 2(c)) and weld metal [for example, EYL-9, Fig. 8(c)], the reduction in area exhibited by FEP-4, is significantly higher (36 percent compared to 10 percent for EYL-1797 and 21 percent for EYL-9). This higher hot ductility may be the result of the probably coarser prior β-grain size of FEP- 4. No metallographic examination was made of this specimen.

EYB-2 - This is an unalloyed grade of titanium, TIMET grade Ti-50A, and does not exhibit a hot ductility dip. When tested in the same manner as the Ti-6211 alloy plate (EYL-1797), EYB-2 exhibits a reduction of area of 90 percent in contrast to 10 percent for EYL-1797. The fracture appearance of EYB-2 clearly shows the large plastic flow in the fracture region and the complete absence of preferential cracking along prior β-grain boundaries. The microvoids in Fig. 14(c) are of widely varying size, shape, and location and follow no planar distribution as seen in EYL-1797, EYL-2011, and the other low hot ductility examples. Thus, the thermal cycle which sensitizes Ti-6211 and Ti-6Al does not sensitize Ti-50A. Metallographic examination of EYB 2 was not performed so microstructural comparison with the other samples is not presented.

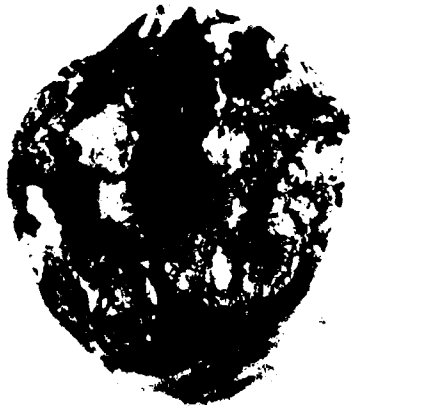

2 mm

D415 (a)

1 mm

7IEV (b)

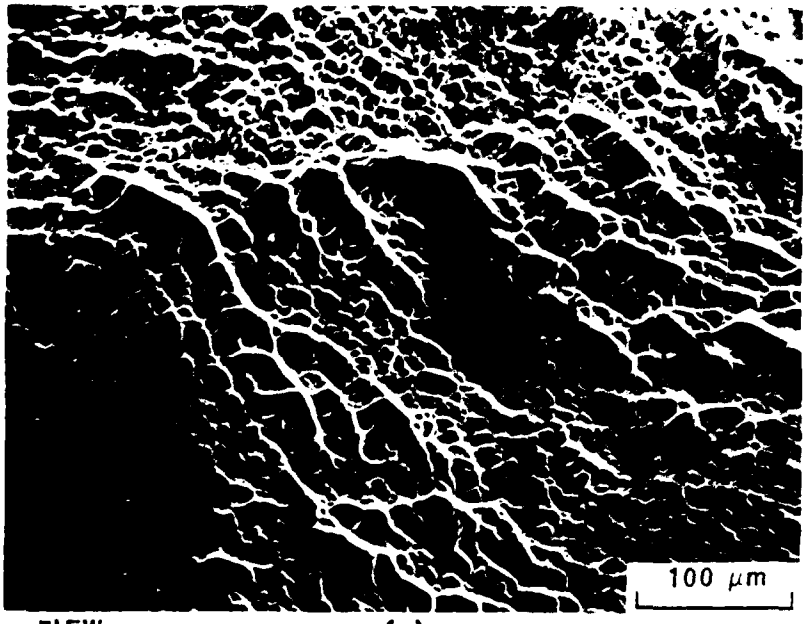

100 μm

7IEW (c)

Fig. 13 Fracture Appearance of FEP-4, Ti-6211 Alloy, 15.2 x 15.2-cm (6x6-in.) Casting, 36 percent RA, broken at 788°C (1450°F) on cooling from 1621°C (2950°F)

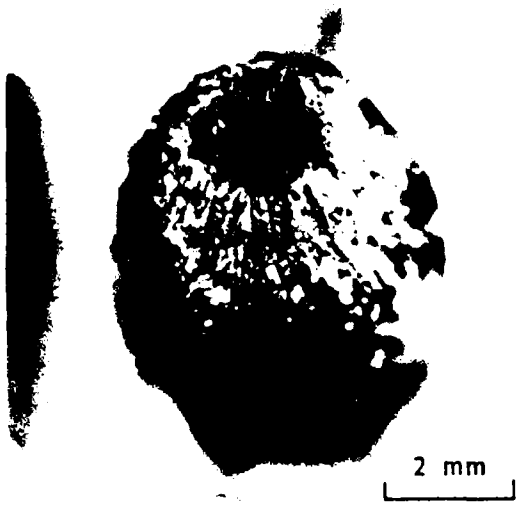

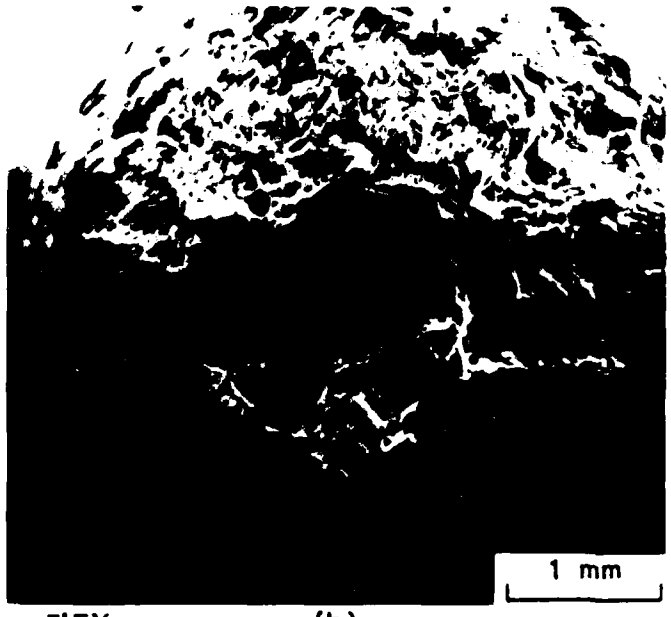

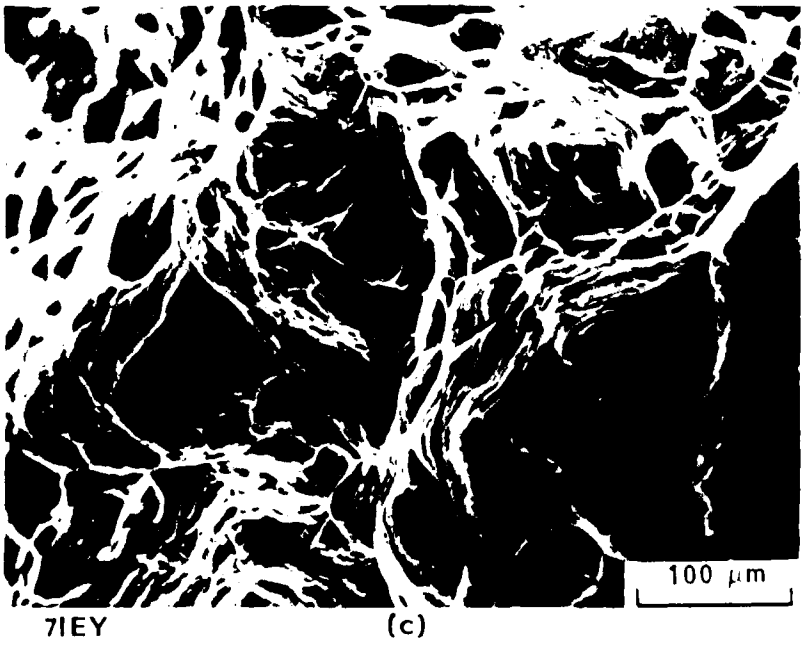

Fig. 14 Fracture Appearance of EBY-2, Titanium Grade Ti-50A. 90 percent RA, broken at 802°C (1475°F) on cooling from 1590°F (2895°F)

Additional Transmission Electron Micrographic Evidence. Because specimens exhibiting low hot ductility fail preferentially by intergranular fracture, selected specimens from EYL-1797, EYL-2000 and EYL-2011 were examined in detail by transmission electron microscopy. Of particular interest was the examination of prior β-grain boundaries for films and precipitates that might be present preferentially in the low hot ductility specimens.

In general, no unusual features were found. Two interesting observations were made however. In one particular instance, a grain boundary region was located in EYL-1797 which contained a string of small particles, see Fig. 15. These particles appear to be ellipsoidal or disk-like, about 24 nm thick and spaced about 50 nm apart. The location of the particle string in Fig. 15 corresponds with the preferred location of microvoid nucleation leading to intergranular separation. See, for example, Fig. 3(b), where microvoids have nucleated as a string along or close to the edge of the grain boundary α.

The second observation was of another microstructural feature that may relate to the grain boundary microvoid nucleation propensity in selected specimens, as shown in Fig. 16. The apparent prior β-grain boundary shown here is positioned diagonally through the center of the figure. Intersection of the α platelets with the grain boundary α produces a periodic array of small pools of β, the dark-appearing regions spaced about 100 nm apart. The location of this array is in agreement with the observed microvoid nucleation sites as shown, for example, in Figs. 3(b) or 7(c).

These small pools of β at the edge of the grain boundary α layer are probably rich in β-stabilizing elements such as Mo and Nb due to alloy partitioning associated with the formation of the grain boundary α and growth of the α platelets, provided the cooling rate was slow enough to allow formation of the latter by nucleation and growth, in contrast with a martensitic transformation; the enriched β is expected to exhibit a low room temperature toughness, but it is not clear that the enriched β is low in hot ductility.

J846

Fig. 15 Transmission Electron Micrograph of Prior β-Grain Boundary Region in Ti-6211 Specimen EYL-1797. Note chain of precipitates near edge of grain boundary

Fig. 1b Transmission Electron Micrograph of Prior β-Grain Boundary Region in Ti-6211 Specimen EYL-1797

Microprobe and Auger Electron Spectroscopy Examination. A portion of the fracture surface from EYL-1797 was examined by an energy dispersive analyzer in the Scanning Electron Microscope (SEM) with the intention of detecting possible local concentrations of α- or β-stabilizing elements. No such evidence was found on the fracture surface, but in one case an anomalous concentration of rhodium was found. If any concentration of Al, Nb, Ta, or Mo existed preferentially on the surfaces examined, there wasn't enough to be detected.

The other surface analysis technique employed Auger electron spectroscopy (AES) with a characteristic capability to detect elemental concentrations in surface layers as shallow as 2 to 3 atom diameters deep. Also, with the recent development of improved gun and detector designs, spot sizes as small as 0.2 μm dia. can be employed.

Attempts to analyze the fracture surfaces of previously tested hot ductility specimens in the AES were made but the results were not useful because of the extensive contamination already present. Attempts to analyze elemental concentrations of polished and lightly etched sections through the tested specimens by AES were also unsuccessful because of contamination. Consequently, DTNSRDC supplied a small number of specimens thermally cycled from RT to about 1638°C (2980°F) cooled to about 816°C (1500°F), then water quenched to RT. These specimens were not broken in the Gleeble, but were machined into small notched round specimens for subsequent fracturing in-situ in the AES equipment.

The first material was Ti-6211 plate broken in situ at about -184°C (-300°F) and examined. Fig. 17 shows the resulting Auger electron energy (E) spectrum as a function of dN/dE, the differential of N(E) versus E. This method of analysis is preferred because of increased signal-to-noise ratio compared to N(E) versus E. The spectra in Fig. 17 were analyzed for elemental concentration and gave the results shown in Table 2. The composition on the fracture surface is in close agreement to the typical ingot composition reported, except for sulfur. Bulk concentration of sulfur in the ingot is

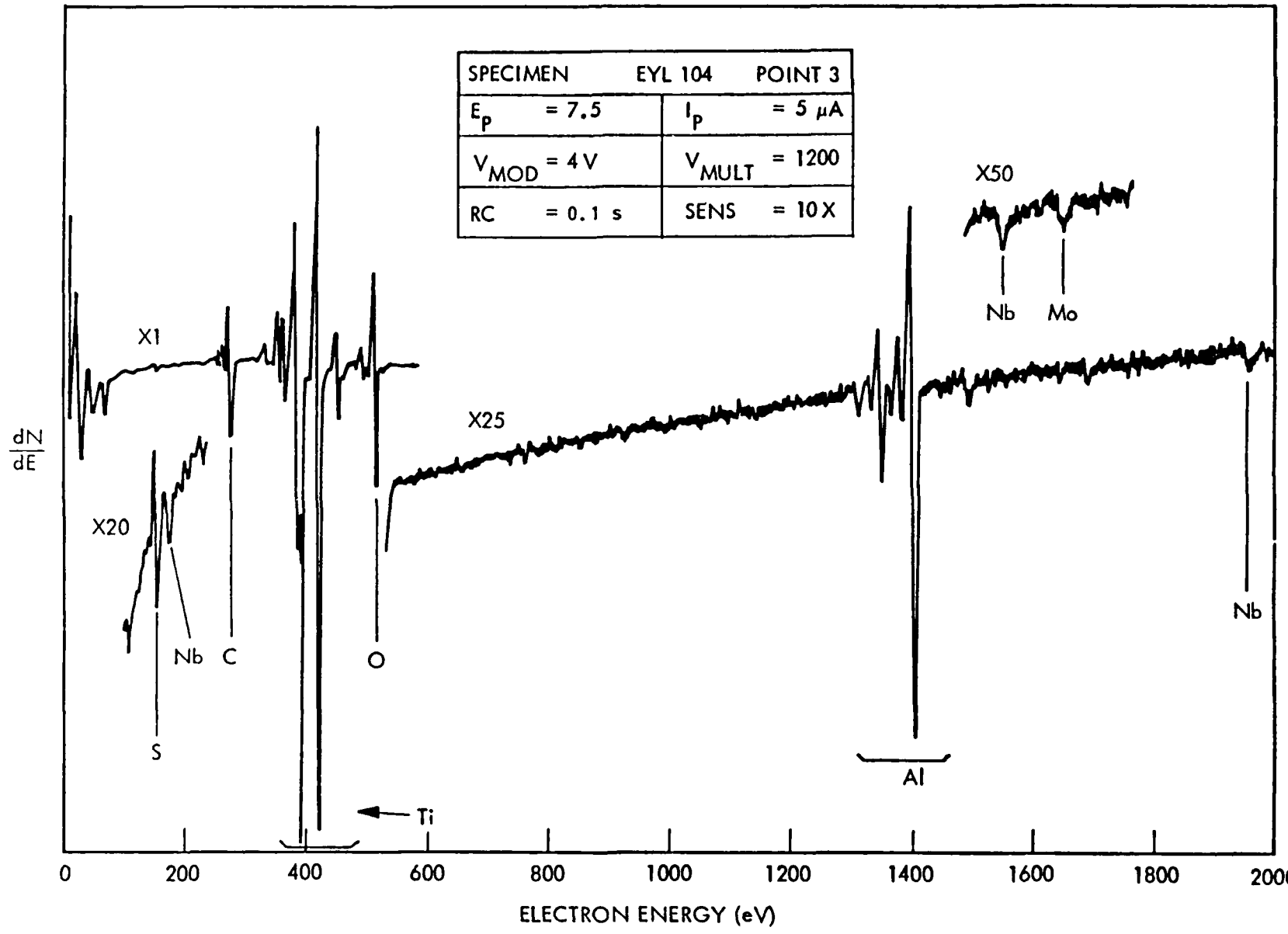

Fig. 17 Auger Spectrum of In Situ Fracture Surface of Specimen EYL-104, β-Processed Ti-6211 5.08-cm (2-in.) Plate, Thermally Cycled From RT to 1632°F (2970°F), Cooled to 818°C (1505°F), then Water Quenched

below the detection level of 0.0015 atomic percent. However, on the fracture surface a concentration of 0.47 atomic percent was found, over 300 times the bulk concentration. The sulfur peak appears on the dN/dE versus E curve at an Auger electron energy level of about 158 electron volts. Because sulfur has been found to be an embrittling species in many alloy steels and other metals, this finding is considered significant. The thermal cycles promoting sulfur embrittlement at grain boundaries in steel involves heating above 982 to

Table 2 ELEMENTAL CONCENTRATIONS ON FRACTURE SURFACE OF THERMALLY CYCLED Ti-6211 ALLOY SPECIMEN

ELEMENT	CONCENTRATION		
	ON FRACTURE SURFACE* at. %	TOP OF INGOT, TYPICAL	
		at. %	wt.%
Al	11.31	10.37	6.0
Nb	0.98	1.05	2.09
Ta	0.21	0.26	1.02
Mo	0.83	0.40	0.92
O		0.23	0.08
N		0.03	0.09
C		0.08	0.02
Fe		0.04	0.05
Si		0.02	0.01
Mn		<0.01	<0.01
Cu		<0.01	<0.01
H	**	0.15	32 ppm
S	0.47	<0.0015	<0.001
Ti	86.2	$\geq$87.5	bal.

* Calculated by AES dN/dE peak-to-peak height analysis method from 5 μm dia. spot on specimen EYL-104, fractured in-situ at $<10^{-10}$ μm Hg pressure

** Not measurable by AES

1093°C (1800 to 2000°F) to promote the diffusion of sulfur to the grain boundaries. Ways to avoid this problem have been to (a) reduce sulfur content to very low levels, or (b) to conduct thermal-mechanical treatments at temperatures below that required for grain boundary segregation of sulfur, so that the grain boundaries remaining are not enriched in sulfur.

Upon welding of Ti-6211, some portion of the heat-affected zone may incur such grain boundary enrichment, assuming the same type of sulfur diffusion occurs. Consequently, some sensitization of grain boundaries in the heat-affected zone is expected. To date no intergranular cracking had been observed in any weldments of Ti-6211, only some transgranular cracking in the fusion zone.

When other thermal processes are employed, such as by drawing, bending, or spinning at elevated temperatures, embrittlement of grain boundaries by segregation of embrittling species such as sulfur may occur during the forming process. The specific conditions of thermal history required to cause such embrittlement will depend on the temperature and time and not particularly on the heating or cooling rate except as they affect the time above some critical temperature. The effect of grain boundary embrittlement is likely to have only a small effect on toughness at elevated temperatures high enough to produce a really low shear stress and high shear strain in the grains. At lower temperatures where the shear strength of the grains increases significantly, then the embrittled grain boundaries become the locus for fracture initiation.

AES in situ fracture surfaces of thermally cycled Ti-3Al-2.5V alloy were also examined. The Auger electron energy spectra obtained show the presence of both sulfur and iron on the fracture surface. A profile analysis for oxygen, carbon, titanium, aluminum, iron, and sulfur was performed by progressive etching of the surface with argon ions and continually monitoring the Auger electrons. The relative elemental concentrations as a function of depth below the fracture surface are represented in Fig. 18, where peak-to-peak amplitude

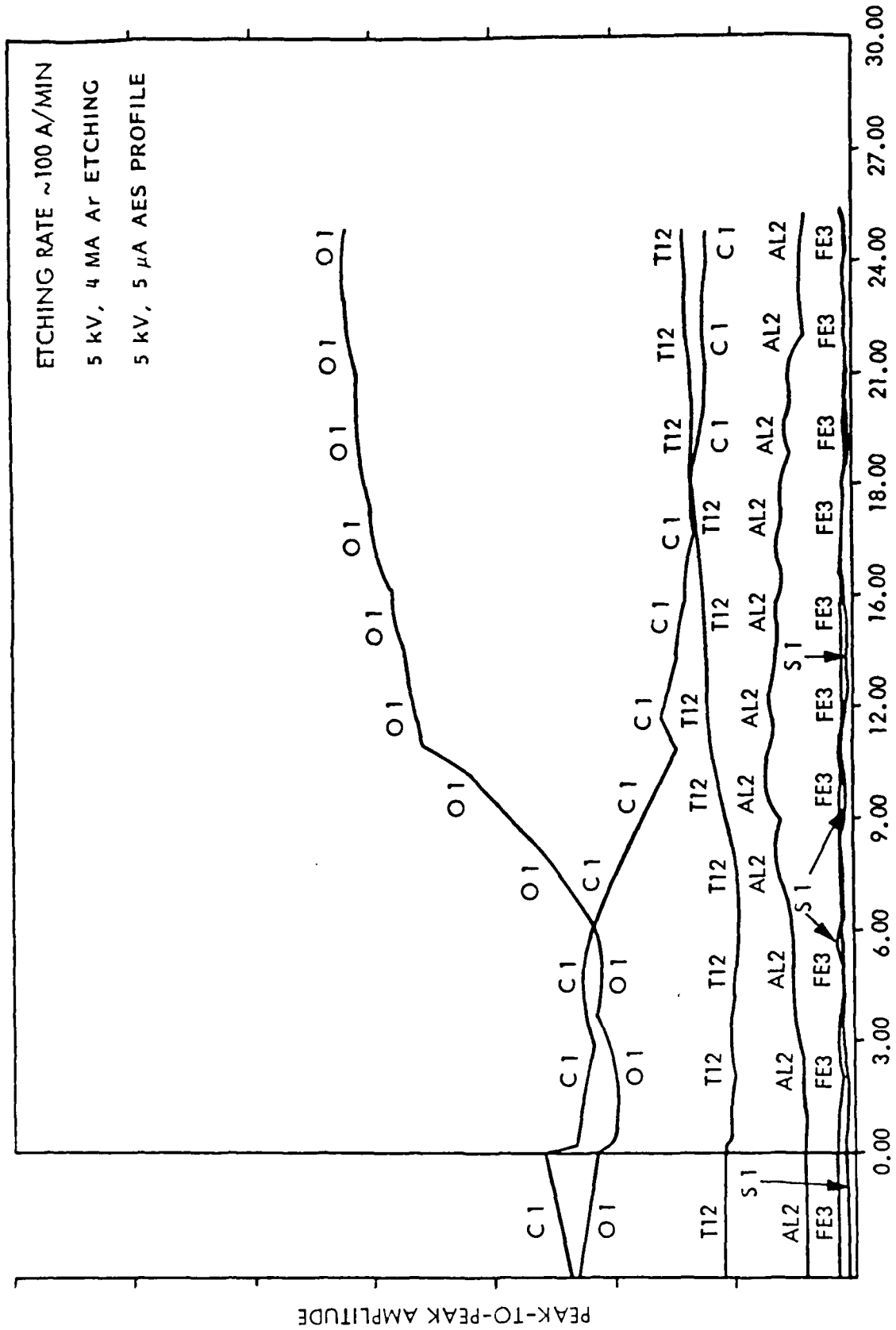

Fig. 18 Auger Profile Through Fracture Surface Oxide Film on Specimen FLJ-250, Ti-3Al-2.5V Alloy, Thermally Cycled from RT to 1616°C (2940°F), Then Water Quenched

of the dN/dE curve is plotted as a function of sputter time. The argon sputtering conditions used remove about 100 Å per minute from the specimen surface. This profile shows the presence of an anomalous thick oxide film on the fracture surface. The oxide film was seen by secondary electron imaging as a "glassy" coating on the fracture surface. Not only was the presence of this oxide film unexpected but the manner in which it formed is completely unknown.

The specimen may have incurred some unintended cracking during the high-temperature thermal cycling in air or the machining of the notch may have produced cracking which went undetected. In either case, the crack surfaces would have oxidized, with the film thickness being higher with an increased temperature.

Note in Fig. 18, the iron and sulfur concentrations do not change significantly over the entire range of the profile layer. After about 22.5 and 250 nm were removed by argon sputtering, Auger electron spectra were obtained as shown in Figs. 19 and 20. The sulfur and iron peaks are clearly visible in both instances. Because of the presence of the anomalous thick oxide film on this specimen, quantitative analyses of these spectra are not reported here. Additional tests are recommended where the fracture surface analyzed would be produced entirely within the hard vacuum of the spectrometer chamber so contamination would be avoided.

Sulfur in Titanium. According to Hansen (Ref. 8), a subsulfide with unknown structure and approximate composition Ti_2S has been identified (Ref. 9). The lowest percent addition at which sulfur apears as an insoluble compound, Ti_2S, is 0.02 weight percent as detected in magnesium-reduced Ti-base alloys, hot-rolled and annealed at 788°C (1450°F) (Ref. 10). According to Berger et al (Ref. 11), the solubility of S in α-Ti as well as in β-Ti is between 0.009 and 0.017 weight percent at 900°C (1652°F). The same authors suggest "there are some indications from grain-size studies that S is less soluble in β-than in α-Ti (Ref. 11).

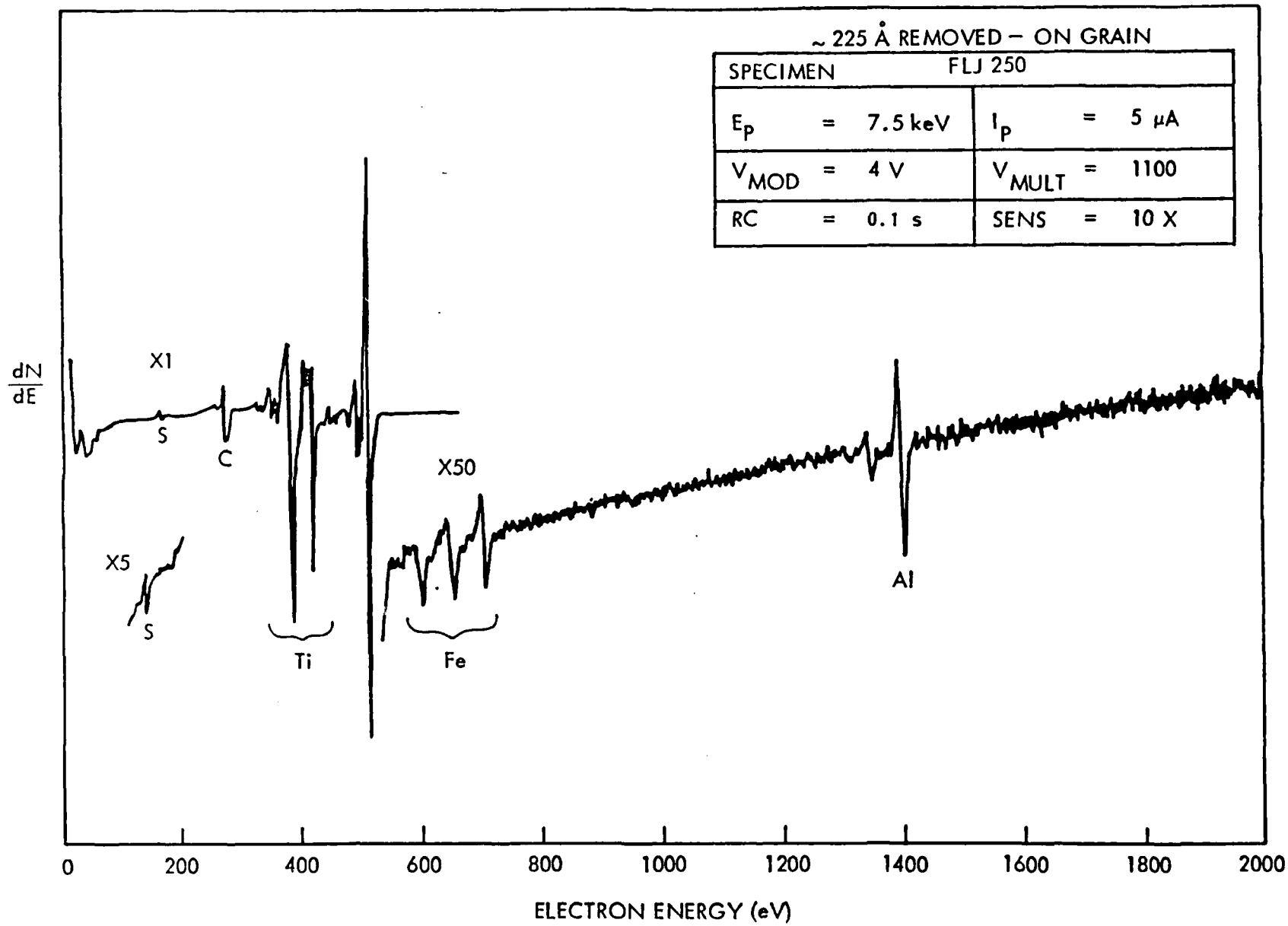

Fig. 19 Auger Spectrum of Specimen FLJ-250 After a 22.5 nm Surface Layer was Removed From the Fracture Surface by Argon Sputtering

LMSC-F108004

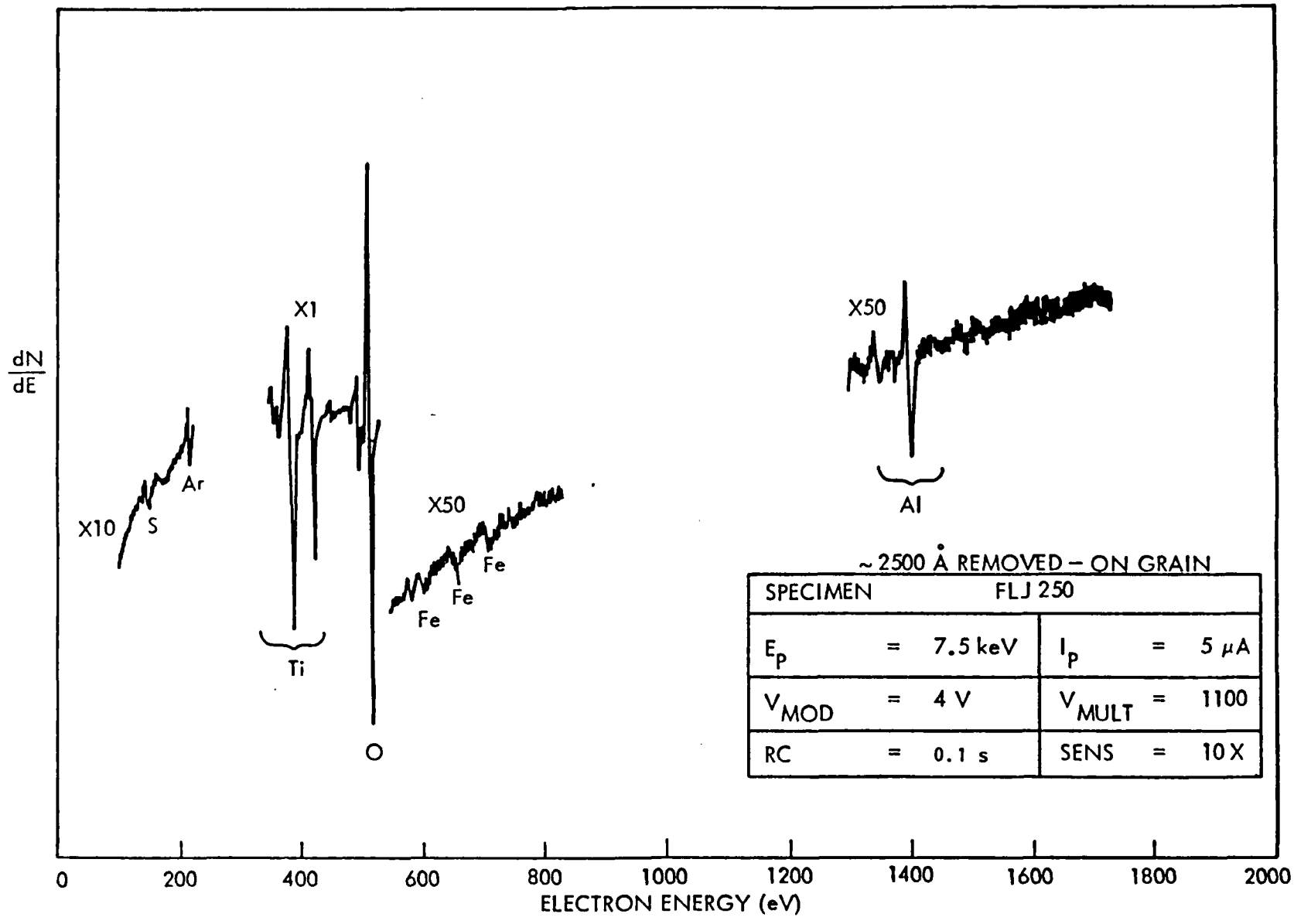

Fig. 20 Auger Spectrum of Specimen FLJ-250 After about 250 nm Surface Layer was Removed From the Fracture Surface by Argon Sputtering

Elliott (Ref. 12) reports the finding by Bartram (Ref. 13) of another solid solution phase having an approximate stochiometric ratio Ti_6S, but its structure and solubility in α- and β-Ti are unidentified.

In light of the findings in the present study, the solubility of sulfur in α- and β-Ti is an important question. Because the hot ductility of Ti-6211 specimens thermally cycled first to a peak temperature of approximately 1649°C (3000°F) is high when tested on cooling down to about 982°C (1800°F) (see Fig. 1), there is the implication that sulfur segregated to β-grain boundaries does not cause embrittlement until α begins to form. The first α to form in tne thermally cycled mateial is at the β-grain boundaries. The concentration of sulfur in the β-grain boundaries may be increased during cooling below the β-transus, as the grain-boundary α layer forms and grows in thickness. This requires the solubility of sulfur to be lower in α-than in β-Ti, contrary to that postulated by Berger et al (Ref. 11). The lower solubility in α causes a progressive enrichment of sulfur in β at the α-β interface during growth of α into β as occurs on cooling from above the β transus.

If solubility of sulfur is higher in α- than in β-Ti, as Berger et al. propose, then no significant enrichment of sulfur due to partitioning would be expected during growth of the grain-boundary α on cooling below the β-transus.

Additionally, the observed increased tensile ductility on cooling below 760°C (1400°F) is probably related to the progressive increase in strength of the grain-boundary α region so that the fracture process involves a significant plastic strain throughout the matrix of the prior β grains. This is in contrast to the localized plastic flow along the prior β-grain boundaries when a tensile stress is applied in the hot ductility dip region, 760 to 843°C (1400 to 1550°F).

1.3 CONCLUSIONS

1. Characteristics of fracture of Ti-6211 in the hot ductility dip between 760°C and 843°C (1400 and 1550°F) are microvoid nucleation and coalescence preferentially along prior β-grain boundaries leading to intergranular fracture. A necessary criterion for such fracture to be exhibited is a previous thermal excursion high above the β-transus, particularly 1204 to 1649°C (2200 to 3000°F). This fracture mode produces a low tensile ductility as measured by reduction in area either on heating or cooling to 760-843°C (1400-1550°F), provided the necessary thermal excursion has occurred.
2. Ti-Al alloys other than Ti-6211 appear to exhibit a similar hot ductility dip, namely Ti-6Al and Ti-6Al-4V.
3. The fracture surface of Ti-6211, 5.08-cm (2-in.) thick, β-processed plate thermally cycled to about 1649°C about (3000°F) has a significant concentration of sulfur present, 0.47 atomic percent, over 300 times higner than the bulk concentration. This is based on Auger electron spectroscopy of an apparent prior β-grain boundary region on the surface of the fracture produced at about -184°C (-300°F) in an atmospheric pressure of less than 10^{-10} mm Hg.
4. The preferred locus for microvoid nucleation and coalescence in low hot ductility specimens of Ti-6211 is in the grain boundary α close to its boundary with the prior β-grain microstructure or at the interface between the grain boundary α and the prior β-grain microstructure. Transmission electron microscopy reveals in one instance a chain of fine precipitates about 25 nm in size and spaced about 50 nm apart within but near the edge of the grain-boundary α. TEM also reveals a string of small pools of β at the border between grain boundary α and the prior β-grains. Either or both of these features may have some relationship to the preferred fracture associated with the low hot ductility dip.

Section 2
METALLURGICAL INVESTIGATION OF THE HOT DUCTILITY DIP PHENOMENON IN THE Ti-6211 ALLOY

2.1 INTRODUCTION

Based on the results of the preliminary study presented in Section 1, a further analysis was indicated to identify possible causes or contributing factors related to the hot ductility dip phenomenon. These analyses involve the detailed examination of microstructures and fracture features of a series of simulated weld thermal cycled ("Gleeble") specimens prepared from Navy-supplied Ti-6211 material of different types and different thermal-mechanical histories. The general approach involves using the Gleeble to program cycles simulating weld near-heat affected zone thermal histories using small cylindrical specimens and to dynamically break the specimens in tension at different temperatures either on cooling or heating (Ref. 14). Optical, transmission electron, and scanning electron microscopy was used to characterize metallurgical features found in each specimen and to attempt to identify those factors that are significant or insignificant with respect to the hot ductility behavior.

2.2 TECHNICAL BACKGROUND

2.2.1 Cracking During Fabrication

The Ti-6Al-2Cb-1Ta-0.8Mo (Ti-6211) alloy has been developed for potential use in various advanced design naval vessels. Fabrication of these vessels will involve forming and joining procedures including variously, fusion welding, hot spinning or shear forming, forging, and bending operations. Preliminary fabrication experience at DTNSRDC-Annapolis has shown that certain fabrication procedures may cause fracture in the Ti-6211 alloy. Hot forming such as shear

spinning may cause intergranular cracking when multiple reheats above the beta transus are involved. Highly constrained weldments may incur transgranular cracking in the fusion zone of multiple pass welds. It is important to determine the major factors contributing to such cracking, as it may significantly increase the manufacturing cost due to rejection and repair of defective components. The cracking may also reduce the reliability of such structures in service, as growth of undetected and unrepaired cracks may lead to premature failure.

An understanding of the fracture behavior would provide a useful basis for modifying composition or fabrication procedures to suppress or eliminate cracks formed during fabrication. Studies conducted at DTNSRDC-Annapolis have shown that the Ti-6211 alloy incurs a significant loss in hot tensile ductility between 760°C (1400°F) and 871°C (1600°F) provided the material was previously heated well above the beta transus for a short time. It is important to establish whether a relationship exists between the observed loss in hot ductility and cracking induced by fabrication procedures.

2.2.2 Intergranular Fracture

As part of the development activity for the Ti-6211 alloy, weldability studies were conducted over the last few years at the DTNSRDC-Annapolis facility (Ref. 15). These studies included hot ductility tests which involve simulated weld heat affected zone thermal cycling with tensile testing on heating or cooling. A typical weld thermal cycle is shown in Fig. 1 of Appendix B. Low (0 to 20 percent) hot ductility was observed for plate or weld fusion zone material upon testing in tension between 760°C (1400°F) and 871°C (1600°F) on cooling from peak temperatures between 1204°C (2200°F) and 1649°C (3000°F), see Fig. 1 in section 1.2.2). Low hot ductility in the same test temperature range was also observed on heating of weld fusion zone material. Similarly, a low hot ductility is exhibited by Ti-6Al-4V, Ti-6Al and Ti-7Al-2Nb-1Ta. A modest hot ductility dip is exhibited by the Ti-3Al-2.5V alloy (60 to 70 percent minimum reduction in area). The commercially pure alloy, Ti-50, was

found to exhibit a negligible hot ductility dip (90 percent minimum reduction in area).

Other factors found to have a negligible, minor, or inconclusive effect on the hot ductility dip include the following (Section 1).

(a) Microstructure: both β- and α + β processed plates, including size and amount of the α platelets and "blockiness" of the plate colonies.

(b) Molybdenum: amount of molybdenum present does not appear to affect the hot ductility level but the minimum occurs at a lower temperature with increased molybdenum.

(c) Oxygen: the effect of between 0.075 and 0.120 weight percent oxygen on the hot ductility dip in Ti-64 and Ti-6211 was found to be negligible.

(d) Yttria: hot ductility of Ti-6211 containing either 50 or 150 ppm Y_2O_3 was found to be the same, but the minimum hot ductility exhibited is higher than when no Y_2O_3 is present (20 percent higher reduction in area).

(e) Cast versus Wrought *Plate: castings* were found to exhibit a higher hot ductility (minimum reduction in area about 20 to 50 percent for castings compared to 0 to 20 percent for 5 cm thick plate).

Fracture of Ti-6211 in the hot ductility dip region is intergranular along prior β-grain boundaries (Section 1 and Ref. 15); see Figures 6 and 7, section 1.2.3.2. The predominant microscopic fracture mode is microvoid nucleation and coalescence and occurs at the border between grain boundary α and the microstructure within the prior β grains or within the grain boundary α but close to its edge (see Section 1.2.3).

Two metallurgical factors which may control or contribute to this prior β-grain boundary fracture have already been suggested (see Section 1.2.3). One is segregation of impurities to the grain boundary α interface and the other is the localized strength mismatch between the grain boundary α and the

matrix at the break temperature. This is attributed to alloy partitioning during nucleation and growth transformation of β to α at the prior β-grain boundary.

Evidence to support the first proposed factor is as follows. Transmission electron microscopy examination of an apparent grain boundary α region in a thermally cycled specimen which exhibited low hot ductility revealed an example of a small chain of very fine precipitates, 25 nm in size and spaced about 50 nm apart. These were within the grain boundary α but near its edge: see Section 1.2.3, Fig. 15. Such particles could promote nucleation of microvoids upon application of tensile stress.

Additionally, there is some possibility that segregation of sulfur to the prior β grain boundaries may occur as a result of thermal cycles above the β transus. In the recent study, Auger electron spectroscopy revealed a concentration of sulfur of 0.47 atomic percent on an apparent prior β grain boundary of a thermally cycled Ti-6211 specimen (Section 1.2.3). This concentration of sulfur is over 300 times the bulk concentration. The fracture surface, however, was formed by testing at about 77 K, and not at the temperature range known to produce the lowest hot ductility (760 to 871°C). Experiments are needed to confirm that the surface analysis technique is free from sulfur contamination artifacts and that the fracture surface studied is intergranular (prior β-grain boundaries).

2.2.3 Transgranular Fracture

As part of the weldability studies at DTNSRDC-Annapolis, welding of highly constrained, intersecting joints was performed. In some cases, transgranular cracking was observed in the weld fusion zone of previously deposited passes (Ref. 16). To date, cracking has not been observed at weld centerlines or in the base metal heat affected zones. The relations between microstructure and fracture path, crystallographic orientation, impurity levels, and other factors have yet to be determined. Because the fusion welding process can introduce rather large amounts of oxygen and hydrogen from dissociation of

water vapor in the inert shielding gas, the composition and impurity concentrations need to be analyzed carefully in weldments and related to the severity of cracking incurred.

The study described in the following subsection has as its goal the identification of major factors controlling intergranular and transgranular cracking in the Ti-6211 alloy as pertains to fabrication requirements of the alloy.

2.3 METALLURGICAL INVESTIGATION

2.3.1 Materials

One piece of Ti-6211 plate, approximately 30 x 60 cm and 2.5 cm thick, was received for use in the current study. This is from the same lot of plate provided all ONR participants in the Ti-6211 program. Composition, properties and processing history are already known to ONR and DTNSRDC. Twenty specimen blanks 6.4 mm dia. x 11 cm long with threaded ends were prepared from the plate for Gleeble programmed tests. The axis of these specimens was transverse to the final rolling direction in the plate. The first set of blanks was provided to DTNSRDC for thermal cycling at the beginning of the program. A second set of 15 specimens was also prepared from the same plate for additional Gleeble cycling by DTNSRDC.

Additional materials were made available for hot ductility evaluations. All the materials used are listed in Table 3.

2.3.2 Experimental Procedures

The thermal cycling (Gleeble) test procedures (Ref. 14) used are essentially the same as reported by other investigators (Refs. 2, 17). The test specimen and gripping arrangement is positioned within an argon-filled chamber to minimize oxidation and interstitial contamination. When specimens are broken on command during the thermal cycle, a tensile force is applied by an

Table 3 TITANIUM ALLOY SAMPLES FOR MICROSTRUCTURAL ANALYSIS

Spec. No.	Description	Notes
	ONR-SUPPLIED Ti-6211 2.5-cm PLATE	
Plate	(β-processed, α-β annealed)	
FQC-11	RT-1621°C (2950°F) - RT	a,b
FQC-7	RT-1627°C (2960°F) - break on cooling at 818°C (1505°F), R.A. = 9.5 percent	a,c
FQC-20	RT-1542°K (2807°F) - RT, break on heating at 816°C (1500°F), R.A. = 9.2 percent	a,c
FQC-6	RT-1621°C (2950°F) - RT - 1621°C break on cooling at 832°C (1530°F), R.A. = 3.4 percent	a,c
	Ti-6211 PLATE, 150 ppm Y_2O_3 ADDED TO MELT	
FJH-180	RT-1604°C (2920°F) - RT, break on heating at 818°C (1505°F), R.A. = 23 percent	a,c
FHJ-186	RT-1604°C (2920°F) - RT - 1604°C, break on cooling at 818°C (1505°F), R.A. = 45 percent	a,c
	Ti-621/0.8 5-cm PLATE, β-PROCESSED	
EYL-1797	RT-1649°C (3000°F), break on cooling at 821°C (1510°F), R.A. = 10 percent	a,c
EYL-2000	RT-break on heating at 838°C (1540°F), R.A. = 59 percent	a,c
EYL-2003	RT-1316°C (2400°F), hold 30 s, break on cooling at 757°C (1395°F), R.A. = 14 percent	a,c
	Ti-6Al 5- x 10-cm FORGING	
EJT-7	RT-1593°C (2900°F), break on cooling at 916°C (1680°F), R.A. = 21 percent	a,c

(a) simulated weld thermal cycle
(b) no tensile strain applied during thermal cycle
(c) hot ductility test performed

air-operated, hydraulic-valve displacement controlled actuator. During loading, the actuator produces a uniform tensile deflection rate over the 19-mm long ungripped length. Strain rate in the peak temperature zone (3 mm at mid-length) of the specimen is not measured in the hot ductility test as special extensometers are needed. The thermocouple material used for recording and feedback control in the Gleeble tests is Pt-Pt/26 wt. percent Re. The thermal cycles performed are also included in Table 3.

Samples for optical microscopy of thermally cycled specimens including hot ductility specimens are longitudinal wafers cut with a diamond saw. Each of the 6 mm long wafers contains a portion of the fracture surface. After mounting, the samples are ground through 600 grit SiC paper. Initial polishing is performed on nylon cloth using 1 μm diamond abrasive. Finish polishing is done in a "Fini-Pol" polishing device manufactured by LECO Corp. A slurry of "Finish-Pol" abrasive and ~10 ml of a $NaOH-K_3Fe(CN)_6-H_2O$ solution is used as the polishing medium. Polishing is conducted until a bright surface devoid of scratches, embedded diamond grit and other artifacts is produced.

Two etching procedures are employed, one for bright field examination and another for polarized light examination. For bright field examination, polished samples are first immersed in a solution of oxalic acid. Samples are then etched in a solution of HF and methanol. The oxalic acid immersion is a required step to remove the residue film from the polishing slurry.

Etching for polarized light examination was done with a chromic acid solution producing a dark blue anodized film on the polished surface. This film enhances contrast due to crystallographic orientation, slip, twins, and color variations due to material composition variations affecting local thickness of the anodized film. See Appendix 1 for additional details on procedure and application.

Specimens for TEM and SEM examination were prepared in the standard way.

2.3.3 Results and Discussion

The materials and hot ductility tests performed are summarized in Table 3. One hot ductility sample of Ti-6Al binary alloy was also included for comparison purposes. Optical microstructures of all the samples listed in Table 3 were studied except FHJ-180. TEM examination was made of FQC-7, FQC-20, FQC-6, FHJ-180, and FJH-186. Fractographic features of EYL and EJT specimens are reported in Section 1.2.3.

A number of interesting features are present in both the microstructures and the fracture surfaces and are described in the following.

2.3.3.1 ONR-Supplied Ti-6211, 2.5-cm. Plate. After rolling, the plate was vacuum degassed at 732°C (1350°F) for 2 hours, furnace cooled, then heated to 927°C (1700°F) for 1 hour and air cooled. The microstructure of this material is shown in Fig. 21. The prior β grains are elongated in the rolling direction [horizontal orientation in Fig. 21 (a)]. Thickness of the grain boundary α layer is typically 2 μm, see Fig. 21 (b). The matrix is composed of α platelets separated by β ribs and arranged in "blocks" or "colonies," typical of the nucleation and growth transformation product cooled at a moderate rate from above the β tranus.

This type of microstructure in the α-β alloys is generally favored as having good fracture toughness and fatigue crack growth resistance. However, room temperature tensile ductility is not usually as high as that containing a significant fraction of equiaxial or globular α (Ref. 18). This difference is probably due to more slip able to occur in large patches of α than in the relatively narrow platelets of α as in Fig. 21 (b). Toughness and fatigue crack growth resistance are improved apparently by the effect of platelet colonies forcing a more tortous path for crack growth (Refs. 18, 19).

2.3.3.2 Specimen FQC-11. The simulated weld thermal cycle produced a complex Widmanstatten α' structure as shown in Fig. 22. The grain boundary α thickness is typically less than 1 μm. At positions in the specimen

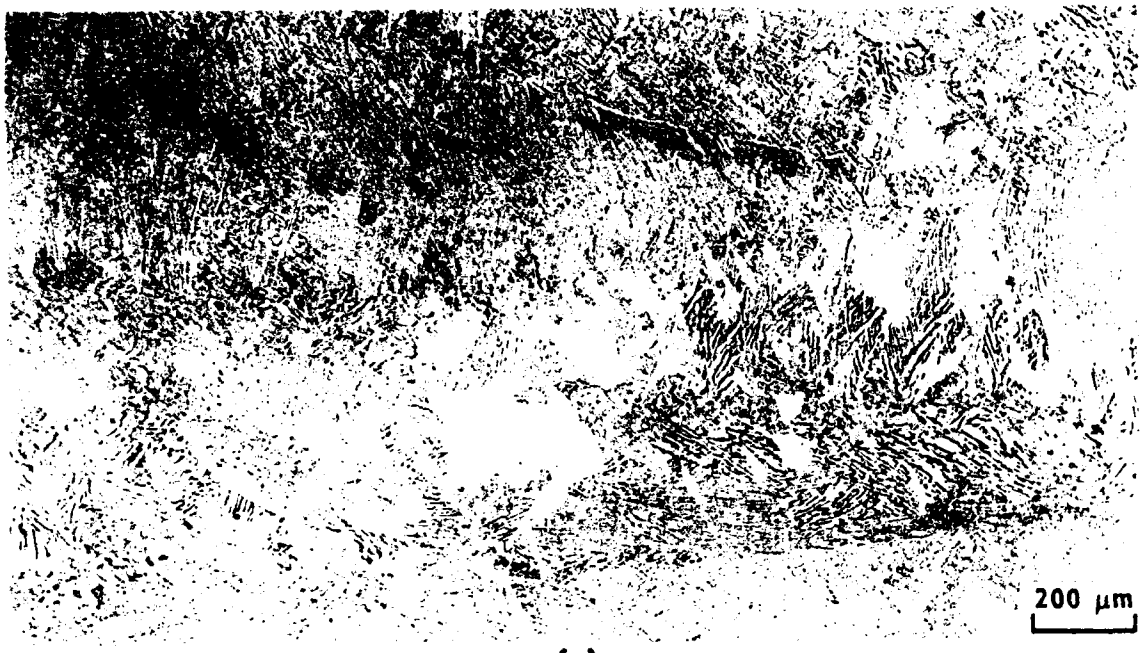

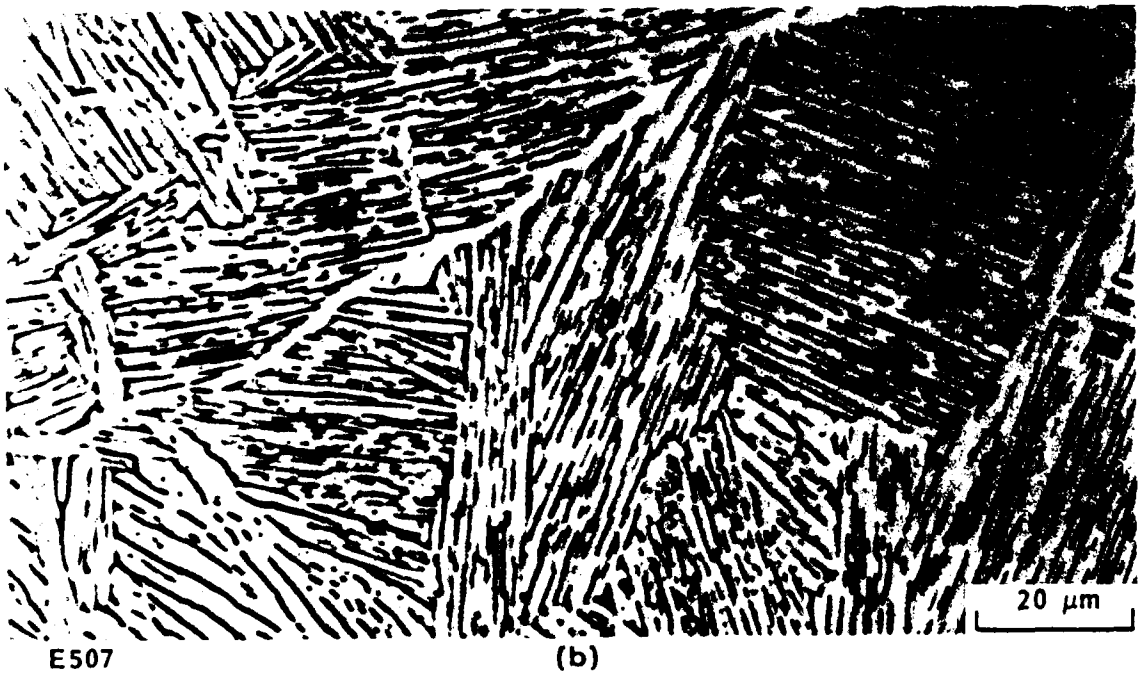

Fig. 21 Microstructure of 2.5-cm β-processed Plate, α - β Annealed. Longitudinal cross section shown (etchant is HF-methanol)

Fig. 22 Microstructure of Specimen FQC-11 (Etchant is HF-methanol)

experiencing a peak temperature of roughly 1482°C (2700°F), the grain boundary α is about 1 μm thick, see Fig. 23. The microstructure immediately adjacent to the prior β-grain boundaries in this region is comprised of α + β in parallel platelet arrays which grew into the grain 10 to 30 μm by a nucleation and growth process and which were interrupted by the α' platelets nucleated within the β grains on cooling. Another feature observed in the microstructure of FQC-11 is the presence within the prior β grains of relatively large patches that have the appearance of α and which are interspersed in the α' microstructures. This is illustrated in Fig. 24. The heterogeneity of size and shape of the α and α' platelets is one of the characteristics to be noted.

In the unstrained condition, grain boundary α in this specimen is relatively free from dislocations, as revealed by TEM (see Fig. 25). Dislocation "walls" exist at the boundaries of this α layer, and may be the locus of a thin layer of β phase. No precipitates or films were seen by TEM; only one β-grain boundary, however, was examined.

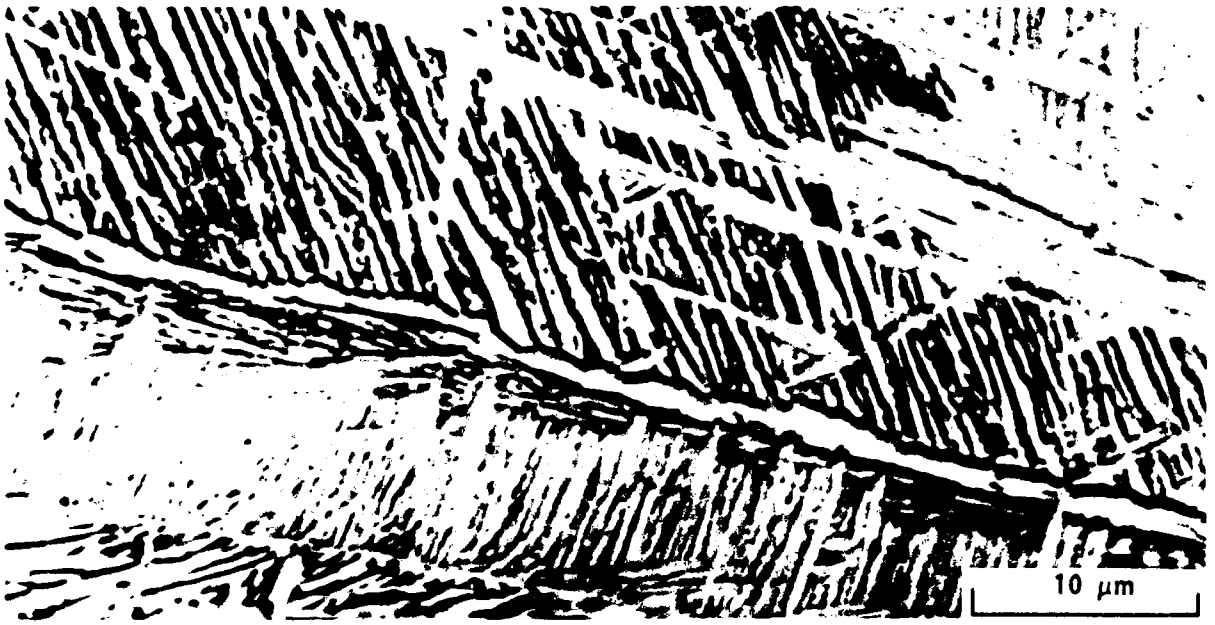

Fig. 23 Microstructure in specimen FQC-11 at a Location Having Reached a Peak Temperature of Approximately 1482°C (2700°F) (etchant is HF-methanol)

Fig. 24 Microstructure in Specimen FQC-11 Showing Large Patches of Apparent α Distributed Within the α' Platelet Arrays (polarized light; etchant is chromic acid)

Fig. 25 Transmission Electron Micrograph of Prior β-grain Boundary Region in Specimen FQC-11 (a) Bright Field, (b) Dark Field

Fig. 25 (Cont.)

2.3.3.3 Specimen EJT-7. Some of the microstructural features are of particular interest in this Ti-6Al hot ductility specimen. The microstructure is shown in Fig. 26. The transformed grain structure is either colonies of nucleation and growth transformation $\alpha + \beta$ or Widmanstatten α'. The boundaries are highly serrated and the structure within the grains is almost featureless except for twins formed by the tensile strain during fracture in the hot ductility test. The structure appears to be a "massive transformation product." It should be noted that such product does twin rather extensively, as shown in Fig. 26 (D). It also shows evidence of slip band formation associated with the intergranular scattered voids at the grain boundaries.

2.3.3.4 Specimen FQC-7. The intergranlar nature of cracking is shown in Fig. 27, which also shows the prevalence of secondary cracks along prior β-grain boundaries near the fracture surface. As seen in Fig. 28, the microstructure is Widmanstatten α' and contains regions that look like α. These are the white areas in Fig. 28 and in which numerous twins have formed by the tensile strain imposed in the hot ductility test. Twinning, at least massive twinning, in the martensite is not visible by light microscopy. Based on the low reduction in area (9.5 percent) the volume plastic strain to fracture in this microstructure was low. It is not clear whether the narrow martensite platelets existed at the hot ductility test temperature. From Gordine's continuous cooling diagram (Fig. 29) combined with the simulated weld heat affected zone cooling curve (Appendix B, Fig. 1) between 1093°C (2000°F) and 815°C (1500°F), one would expect that no martensite would have formed prior to the moment of loading. The large, clear etching patches apparently did exist at time of loading, otherwise they would not have twinned. This evidence suggests the published continuous cooling transformation diagram is in question, and verification is needed. The possibility that tensile strain imposed in the hot ductility test may have affected the $\beta \rightarrow \alpha$ or $\beta \rightarrow \alpha'$ transformation kinetics must also be considered. Such complexities are unusual for normal laboratory investigations of thermally induced transformations; the tensile strain in this example is representative of hot working and fabrication conditions in manufacturing.

E602 (a)

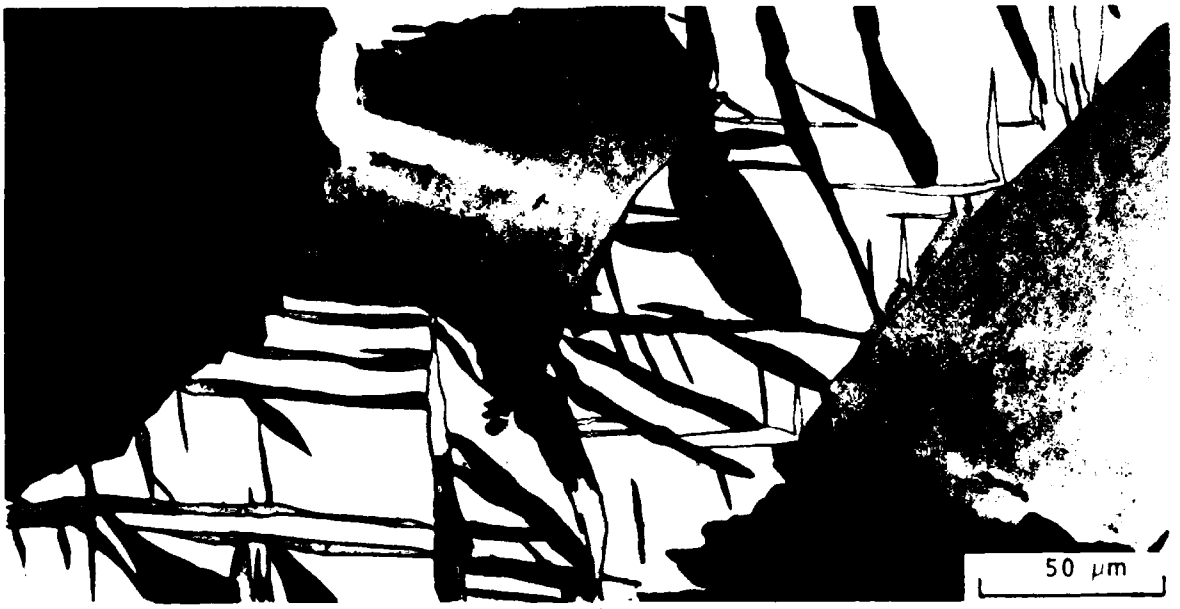

E606 (b)

Fig. 26 Microstructure of Ti-6Al Specimen EJT-7, Showing (a) Massive Transformation Product and (b) Prevalence of Twinning in the Grains and Slip Associated with Grain Boundary Voids (polarized light; etchant is chromic acid)

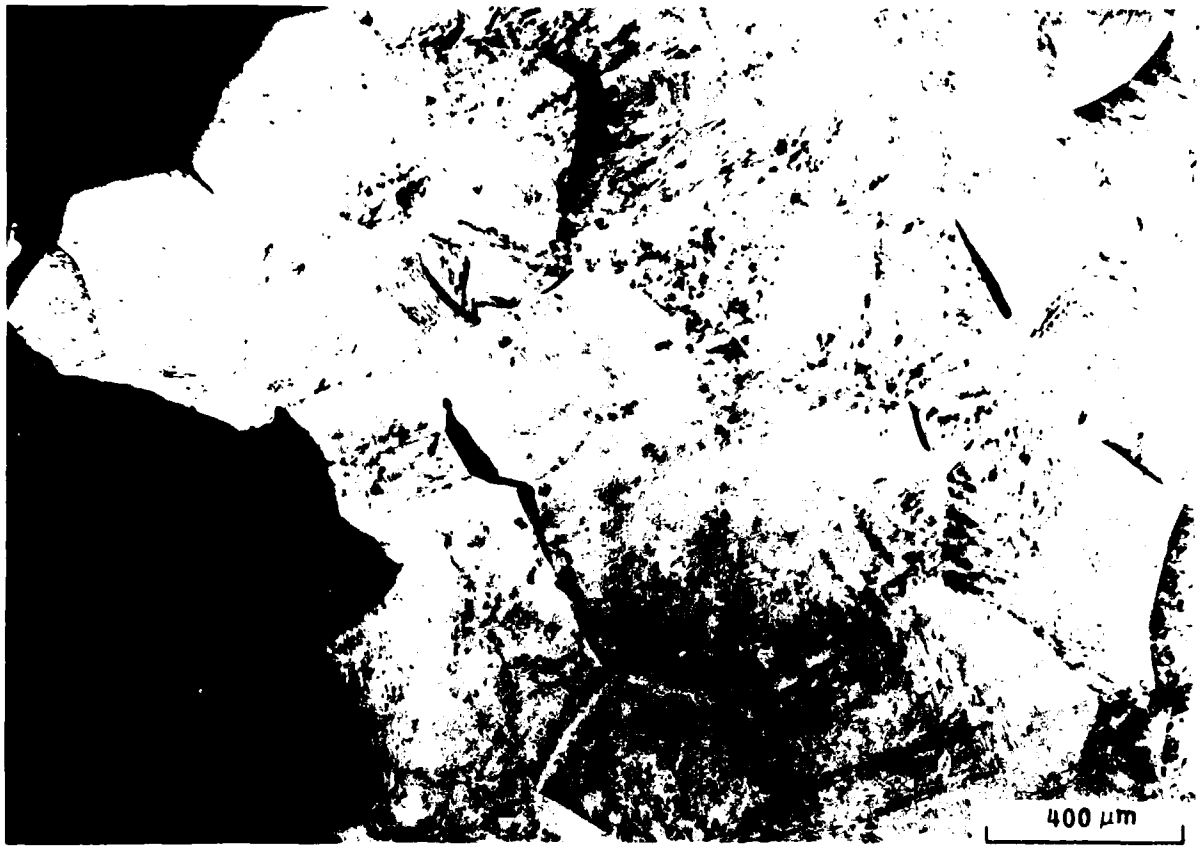

Fig. 27 Section Containing Fracture Surface in FQC-7. This specimen exhibited 9.5 percent reduction in area (etchant is HF-methanol)

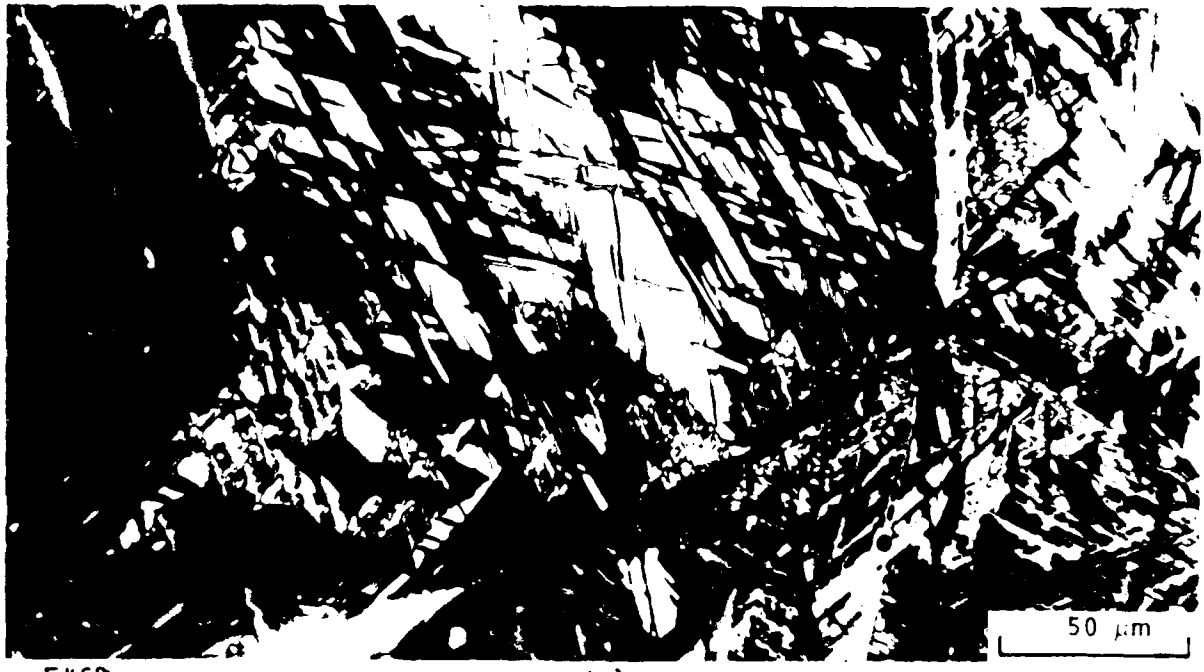

Fig. 20 Microstructure of FQC-7 Showing (a) Twins in Massive α-appearing Patches and (b) Absence of Massive Slip Even between Close-proximity Secondary Cracks (polarized light; etchant is chromic acid)

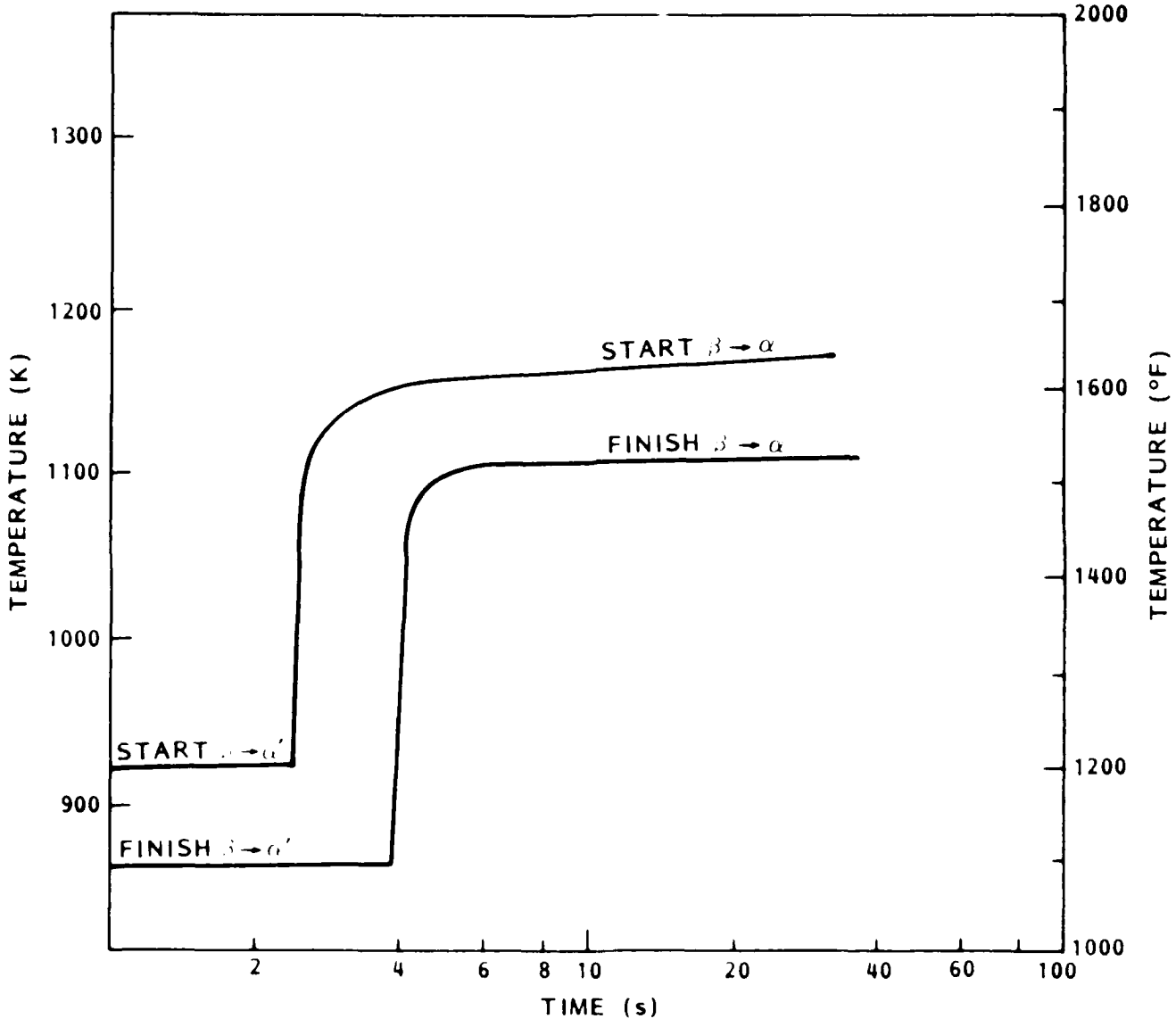

Fig. 29 Continuous Cooling Diagram for Ti-6Al (after Gourdine, Ref. 2)

Fracture appearance of this specimen is shown in Fig. 30. The prevalence of brittle fracture by separation along prior β-grains is evident. Some fracture facets show very little microvoid nucleation and coalescence [right side of Fig. 30 (b)]. This most likely is a surface corresponding to the matrix side of the grain boundary α/matrix fracture interface. The large linear markings on this fracture facet have the same morphology as the larger α' platelets in the microstructure.

4.3.3.5 Specimen FQC-6. Both the microstructure and fracture appearance of this specimen are similar to FQC-7. Compare Figs. 31 and 32 with 27, 28 and 30. As described in Section 1, the factors affecting loss in Ti-6211 hot ductility in the 760 to 871°C (1400 to 1600°F) range are not modified by cooling to room temperature and reheating. This suggests that irreversible segregation of an embrittling impurity such as S to the β grain boundary may be a significant contributing factor, as on heating from RT in a second cycle, upon reaching the break temperature employed here the matrix would not be β but would be α' or overaged α' along with the scattered patches which appear to be α. The apparent irreversibility of S segregation to the free surface of CP-Ti and to grain boundaries in 304 SS has been observed previously (Refs. 20 and 21. See also Fig. 11, Appendix B).

4.3.3.6 Specimen FQC-20. Microstructure and fracture appearance of this specimen are similar to both FQC-7 and FQC-6 and are shown in Figs. 33 and 34. The loss in hot ductility observed during the first thermal cycle (specimen FQC-7, for example) is possibly made somewhat more severe by the second cycle (as in this specimen). It should be noted that the apparent β-grain size does not change because of the second cycle; compare the fracture appearance shown in Figs. 34 and 30. If segregation of an impurity species occurs in the first cycle, but tension is not applied, then reheating to 871°C (1600°F) either does not redissolve the segregated impurity or segregation occurs reversibly upon cooling from the high peak temperature - and the same susceptibility to intergranular fracture is manifested.

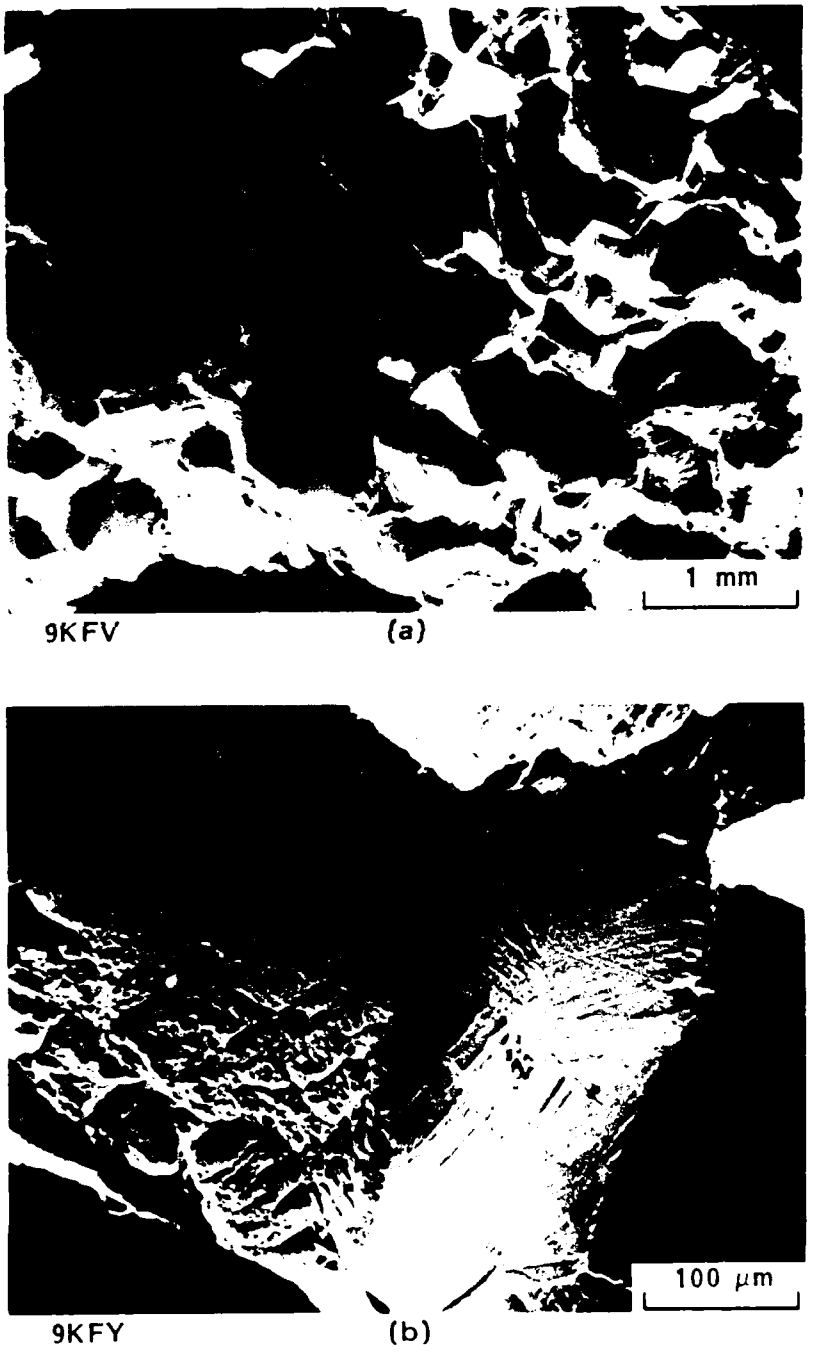

Fig. 30 Fracture Appearance of Specimen FQC-7

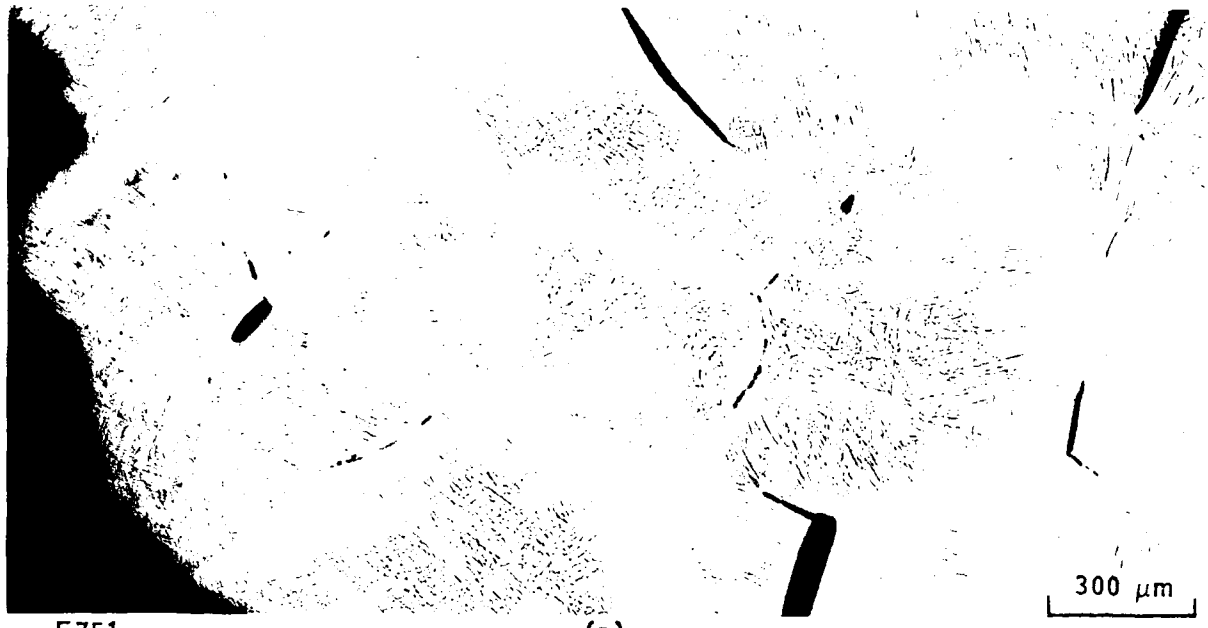

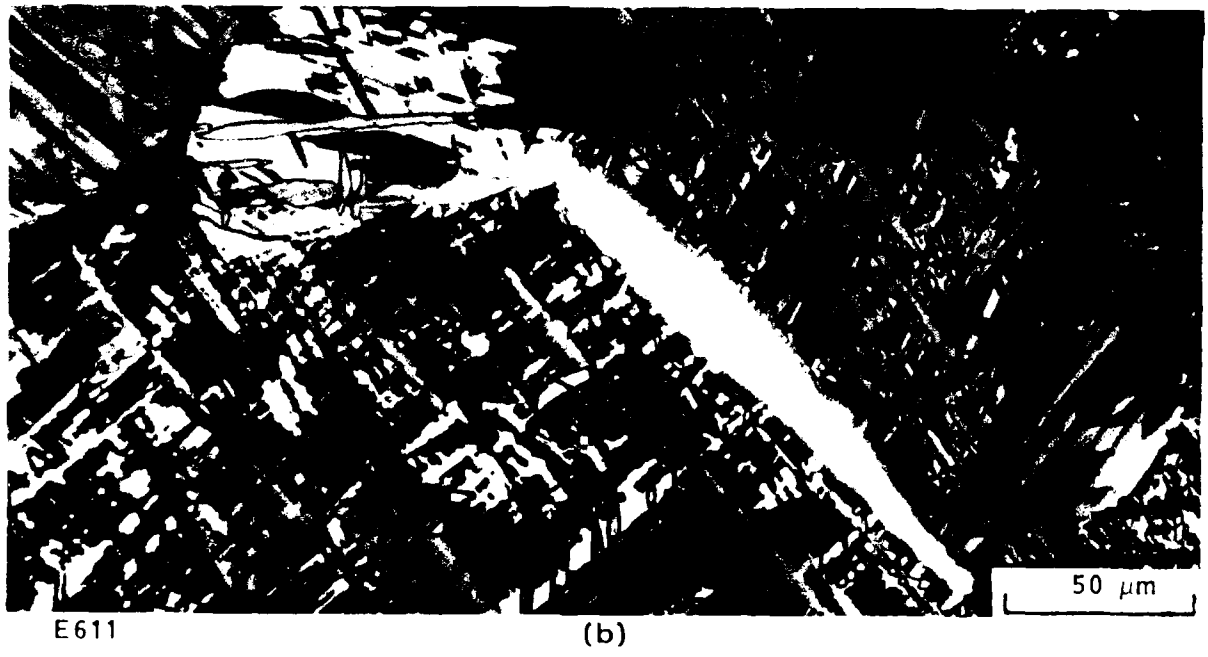

.. 31 Specimen FQC-7 (a) Section Containing Fracture Surface (etchant is HF-methanol), (b) Microstructure in Vicinity of Secondary Crack (polarized light; etchant is chromic acid)

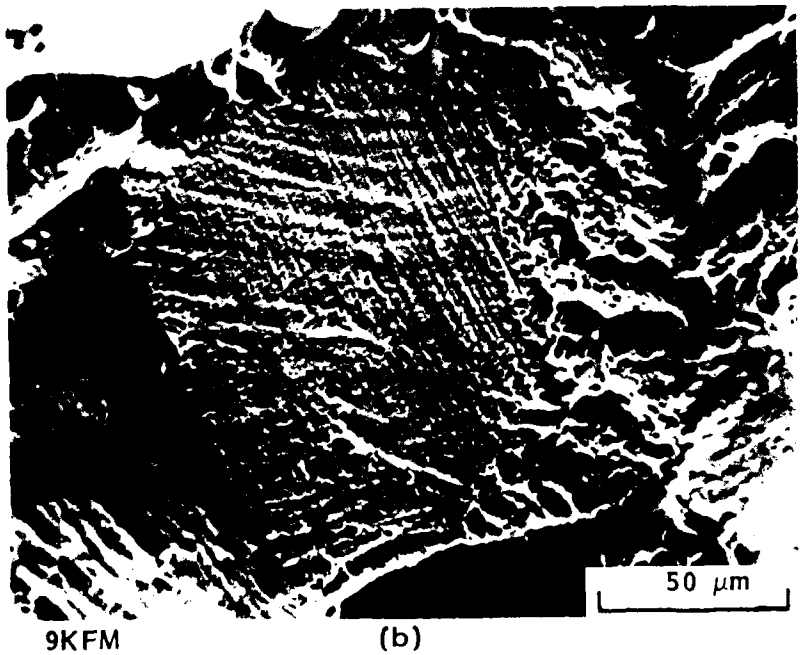

Fig. 32 Fracture Appearance of Specimen FQC-6

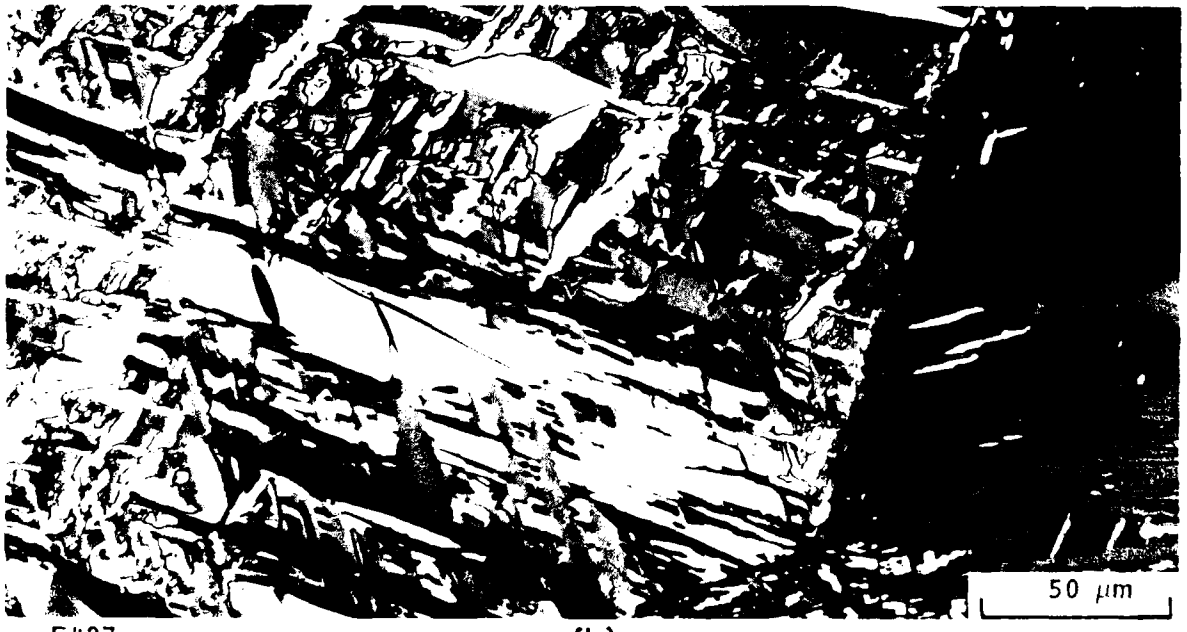

Fig. 33 Specimen FQC-20 (a) Section Containing Fracture Surface (etchant is HF-methanol), (b) Microstructure Near Fracture Surface Containing Prior β-grain Boundary Having Fine Array of Voids (polarized light; etchant is chromic acid)

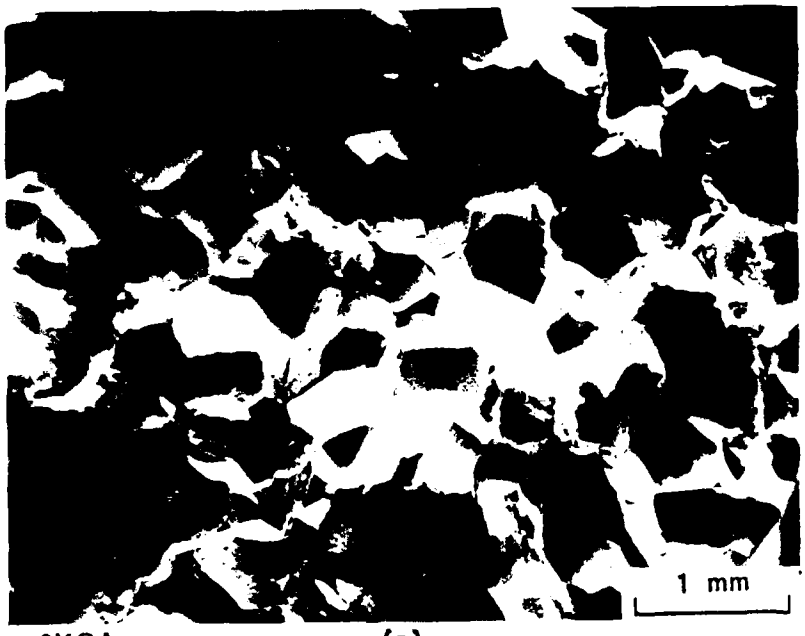

9KGA (a)

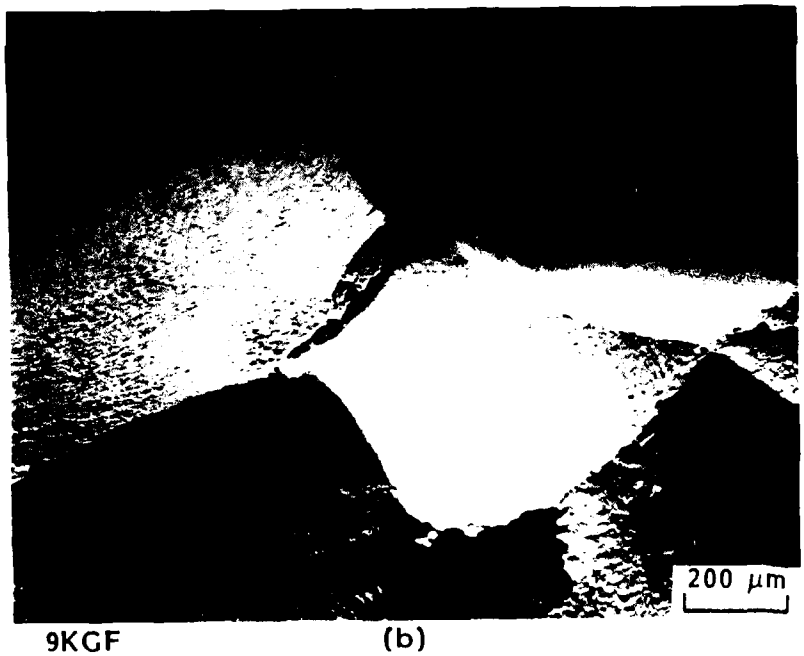

9KGF (b)

Fig. 34 Fracture Appearance of Specimen FQC-20

2.3.3.7 Specimen FJH-186. The addition of Y_2O_3 to the melt in this material causes a number of interesting changes. Compared to FQC-6 which had an identical thermal cycle, this specimen exhibits a significantly higher hot ductility (45 versus 3.4 percent R.A.). The microstructures and fracture appearances are noticeably different than FQC-6. As shown in Fig. 35, the fracture surface is comprised largely of ductile transgranular fracture. Some intergranular fracture is present, but it obviously did not dominate the fracture sequence. Because the apparent size of the prior β-grains is not readily deduced from the fracture surface appearance in Fig. 35, one can see from the fracture surface of specimen FJH-180 (Fig. 36) that the grain size in the FJH series specimen is comparable to the FQC series specimens. Specimens FJH-186 and -180 are expected to have similar size of prior β-grains.

Microstructural features of this specimen are shown in Figs. 37, 38 and 40. the presence of a rather large number of voids scattered about the matrix of the grains is one of the features distinctively different from the FQC specimens series. These voids may be associated with Y_2O_3 particles but such identification has not been made. Some small particles are visible in voids in Fig. 39(a) and are about 1 μm in size; these may be Y_2O_3 particles. Note also the absence of large patches of α as are observed in the FQC-series microstructures.

The subsurface voids seen above may be embryonic void cavities which formed along the primary fracture path. Note in Fig. 35(a), the many examples of deep holes scattered about the fracture surface, particularly along prior β-grain boundaries and in transgranular locations on ductile rupture surface areas.

At high magnifications as revealed by TEM, the microstructure of FHJ-186 appears to be similar to the FQC series. A small pool apparently of β is shown in Fig. 40 with some segregation of β between the α' platelets. In Fig. 41, the structure within coarse and fine α' platelets of FHJ-186 and FQC-6 is compared. In both cases, there is a relatively high density of dislocations within the coarse α platelet. This suggests that the high reduction in area exhibited by FJH-186 is not simply attributable to

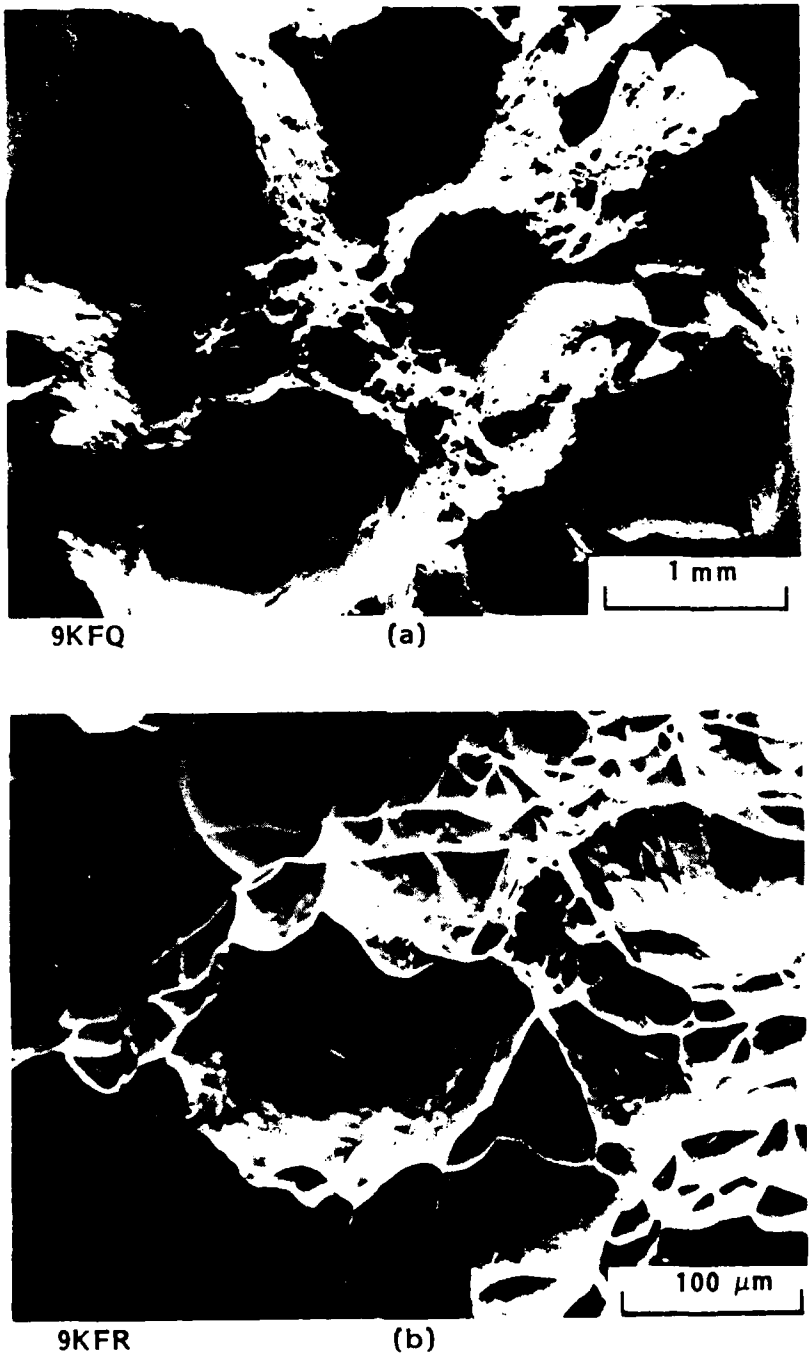

Fig. 35 Fracture Appearance of Specimen FHJ-186

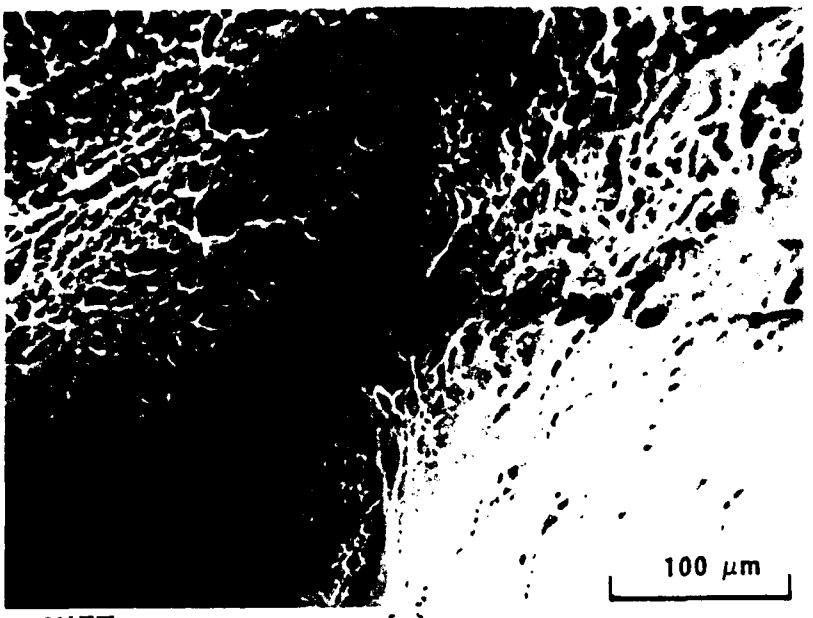

Fig. 35 (Cont.)

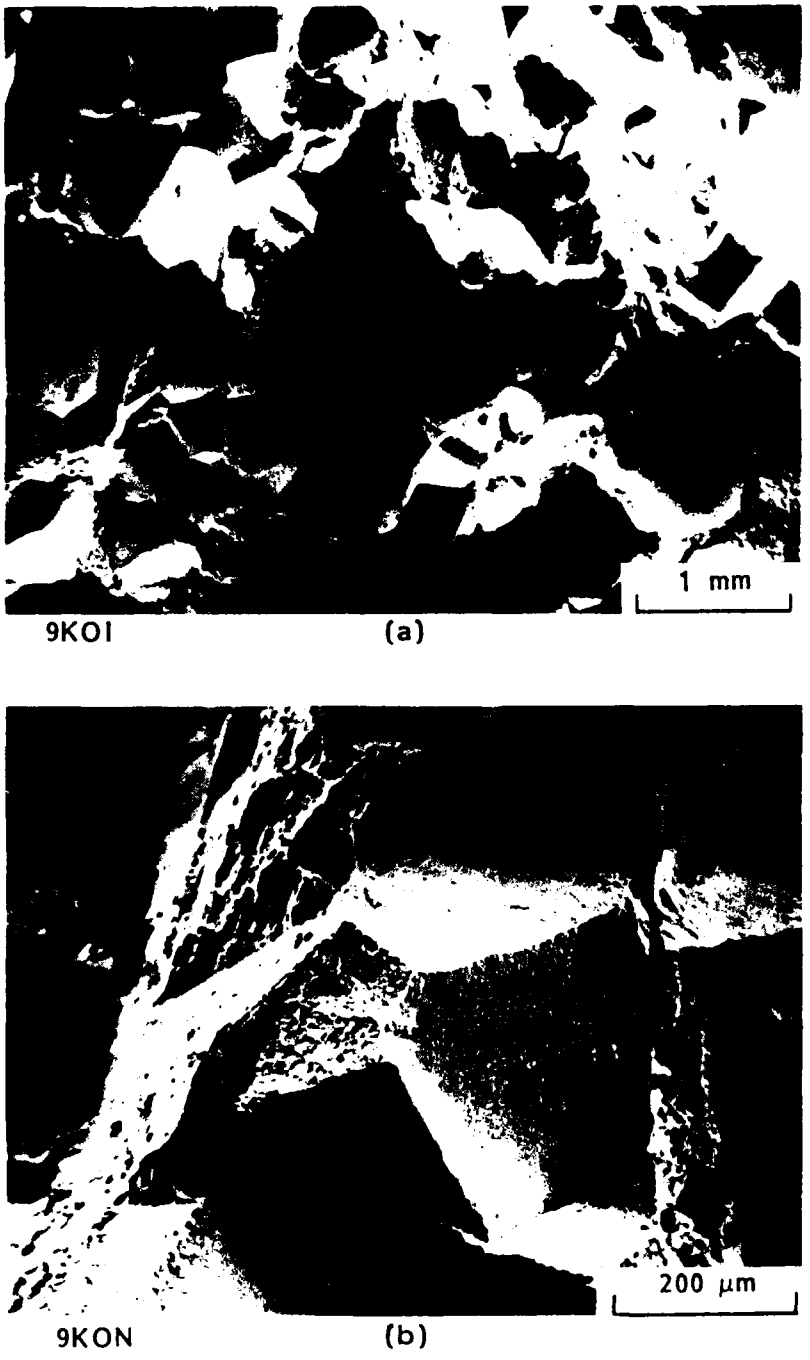

Fig. 36 Fracture Appearance of Specimen FHJ-180

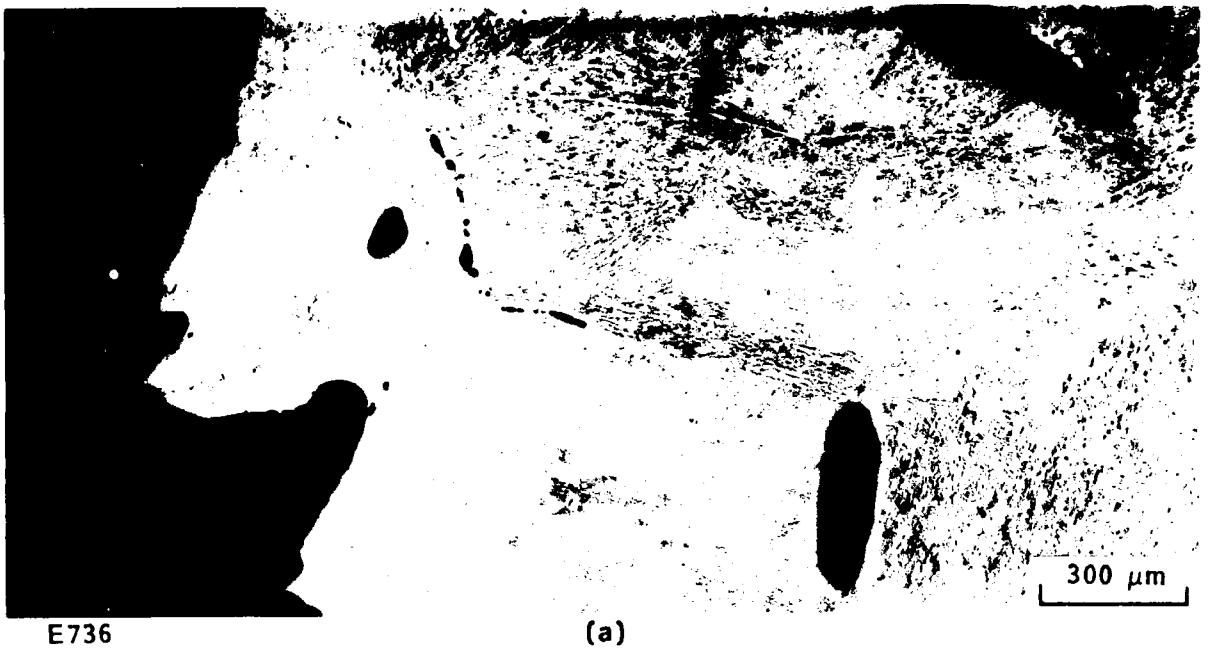

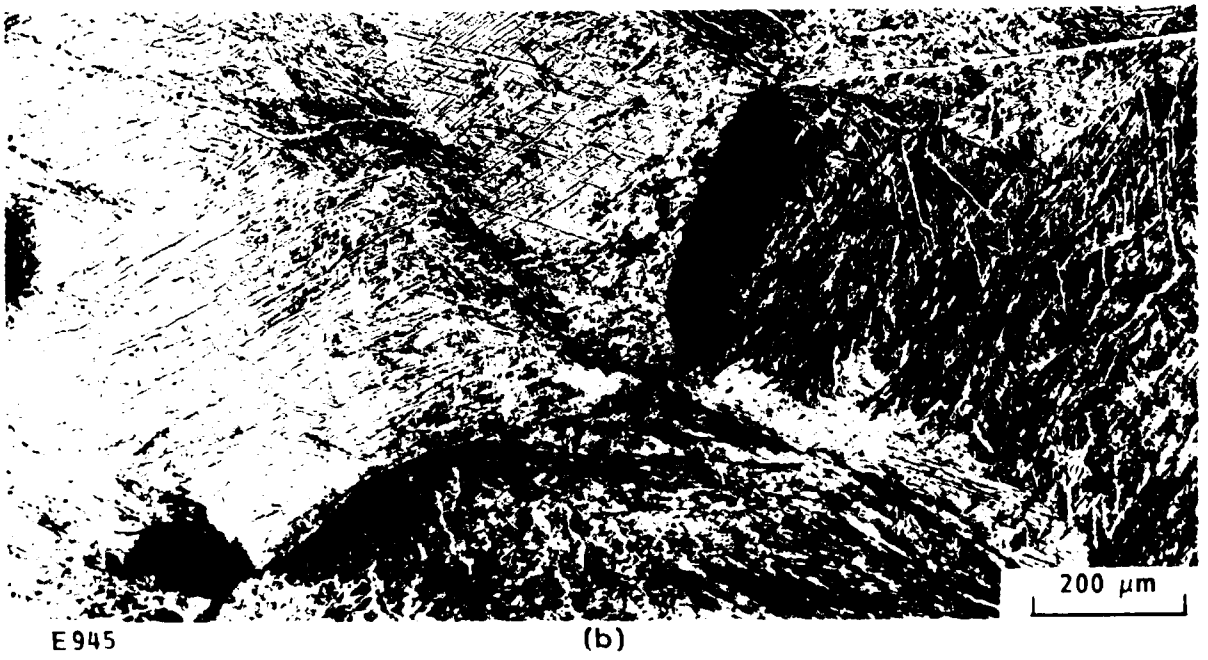

Fig. 37 Specimen FHJ-18b (a) Section Containing Fracture Surface, (b) Microstructure Close to Fracture Surface and Containing Voids at Various Locations (etchant is HF-methanol)

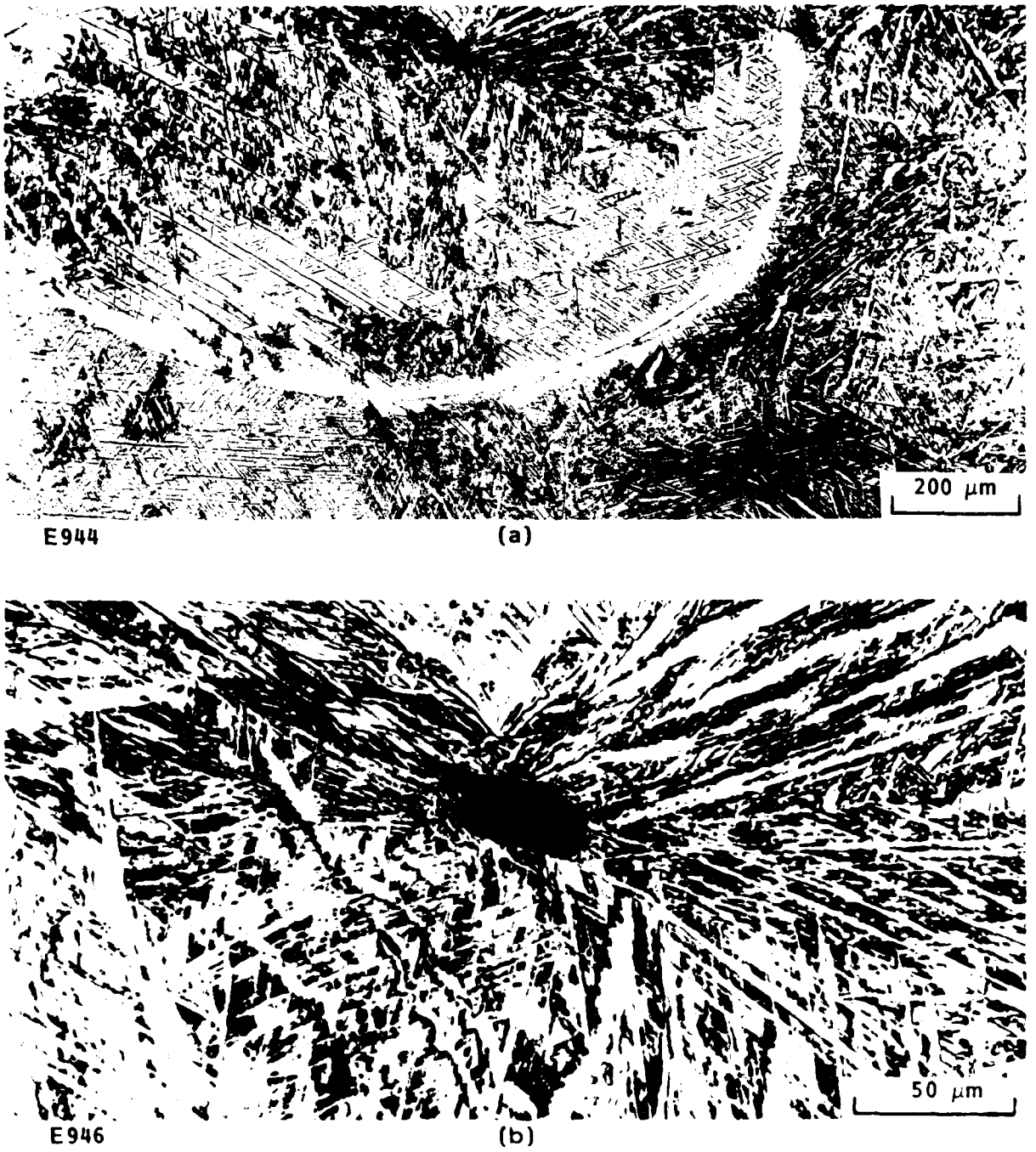

Fig. 38 Microstructure of Specimen FHJ-186 Containing Voids. Region is near the primary fracture surface (etchant is HF-methanol)

Fig. 39 Microstructure of Specimen FHJ-18b Containing Voids. Note preferential location of voids along coarse α' platelets and deformation of α' platelets due to plastic flow

Fig. 40 Transmission Electron Micrograph of Fnd-186 (a) Bright Field, (b) Dark Field

Fig. 40 (Cont.)

L548 (a)

Fig. 41 Transistor [illegible]

AD-A184 286 METALLURGICAL INVESTIGATION OF HOT DUCTILITY LOSS IN TI-6211 ALLOY(U) LOCKHEED MISSILES AND SPACE CO INC PALO ALTO CA R E LEWIS 15 JAN 86 LMSC-F108004 2/3

UNCLASSIFIED N00014-79-C-0449 F/G 11/6 NL

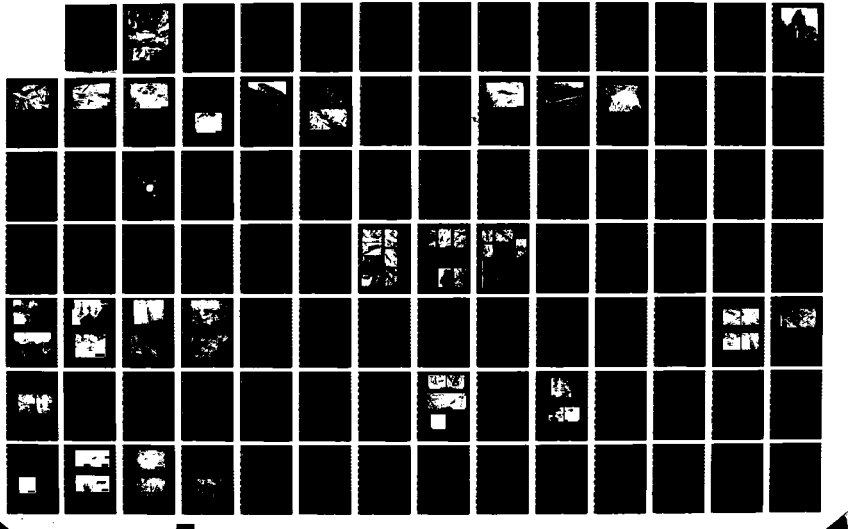

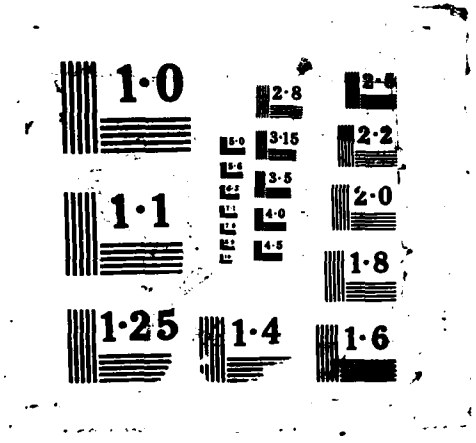
1·0
1·1
1·25
1·4
1·6
1·8
2·0
2·2
2·8
3·15
3·5
4·0
4·5

Fig. 41 (Cont.)

microscopic shear within the α' platelets, but also the high cohesive strength of the prior β-grain boundaries, which, in turn, promotes slip to occur rather uniformly throughout the matrix. This is in contrast to the localization of plastic flow in the FQC series which occurs by twinning in the large, clear etching patches of α.

It is reasonable to suggest that the presence of a number of randomly located, relatively coarse (1 to 10 μm in size) particles of Y_2O_3 may provide at least two benefits. One benefit is to provide additional interfaces in the titanium alloy matrix to attract impurity species which might segregate during an elevated temperature thermal cycle. Such interfaces are an alternative place for impurity segregation rather than just to prior β-grain boundaries. If the segregating species causes a local reduction in elevated temperature cohesive strength, then the presence of Y_2O_3 particles scattered about randomly may also increase the grain boundary strength, while the particle/matrix boundaries would have lower strength.

The other benefit obtains from the effect of the oxide particles on local stress fields as a result of differential thermal contraction on cooling from high above the β transus. Kayno et al. found 0.3 to 1 weight percent addition of lanthanum or cerium increased the yield strength of CP-Ti by 80 percent (Ref. 22). The cerium and lanthanum both form globular oxides ranging in size from 0.01 to 0.1 μm, and upon cooling from elevated temperature, dislocation loops were found around each inclusion. The thermal expansion coefficient of these oxides is approximately one half that of titanium. In the case of titanium alloys containing Y_2O_3, the oxide particles would set up local compressive stress normal to the oxide/matrix interface and tensile stresses tangent to the same interface. Such local stresses may accelerate the $\beta \rightarrow \alpha$ transformation on cooling, and may be the reason for such unusual directionality of α' platelets surrounding the void in Fig. 38 (b), presuming that cavity initiated at a Y_2O_3 particle. Such localized strain concentrators having weakly bonded interfaces and randomly located would provide ideal sites for random void nucleation (as observed in FHJ-186), rather than localized void nucleation only or preferentially at prior β-grain

boundaries (as observed in the FQC series), and at the elevated temperature in which the hot ductility dip phenomenon is manifested.

2.4 CONCLUSIONS

1. A small amount of Y_2O_3 (150 ppm) added to the melt in Ti-6211 significantly increases the tensile ductility (reduction in area) of specimens prepared from plate and broken at a temperature of about 843°C (1550°F) on heating or cooling in the second cycle of a simulated weld heat affected zone thermal excursion to about 1621°C (2950°F) peak temperature. This improvement from 0-10 percent RA for non-Y_2O_3-containing plate to 23-45 percent RA for the Y_2O_3 containing plate may be attributable to the following.

   a. Presence of Y_2O_3 globular particles randomly dispersed in the microstructure provides additional interfaces for segregation of impurities during thermal cycles well above the β transus, which otherwise may segregate primarily to the β-grain boundaries. This would increase the cohesive strength of the grain boundary α/matrix interface at about 843°C (1550°F) and promote the formation of voids at numerous locations away from the grain boundary α region.

   b. Existence of scattered, hard oxide particles in the β-grains during cooling from above the β transus provides local stresses around the particles due to differential thermal contraction and such stresses would promote plastic deformation around the particles upon application of tensile stress in the hot ductility test.

2. Simulated weld heat-affected zone thermal cycling to high peak temperatures produces a complex Widmanstatten α' microstructure which also contains relatively large, clear-etching regions that appear to be α. These latter regions twin extensively during the hot ductility test at about 843°C (1550°F), either on cooling or heating. Specimens similarly thermal cycled from plate to which 150 ppm Y_2O_3 was added

have more uniform size, relatively fine α' platelets, and no significant amount of the interspersed α (apparent massive α) regions.

This latter material does not form coarse twins during the hot ductility test. A tentative conclusion is that the Y_2O_3 addition suppresses the localized twinning phenomenon within the prior β grains and promotes more uniform plastic deformation in the matrix of the grains.

3. Evidence in this study suggests the published continuous cooling diagram for Ti-6211 is in question, and verification is needed.

2.5 RECOMMENDATIONS

1. Direct measurement of impurity elements segregation to prior β-grain boundaries is needed.

2. The effects of cooling rate and strain rate on the phase transformations, fracture mode, and the factors affecting fracture need to be assessed. The hot ductility test techniques presently employed are an efficient way to study these effects.

3. The variation in size and distribution of rare-earth oxides added to the Ti-6211 microstructure should be investigated further regarding their effect on the hot ductility dip phenomenon.

Section 3

EFFECT OF COOLING RATE, STRAIN RATE AND TEST TEMPERATURE ON THE HOT DUCTILITY OF Ti-6Al-2Cb-1Ta-0.8Mo*

3.1 SUMMARY

Cylindrical specimens of the Ti-6Al-2Cb-1Ta-0.8Mo (Ti-6211) alloy (composition in weight percent), 6.4 mm in diameter, were rapidly heated to a peak temperature of 1593°C (2900°F) and cooled using a high-speed thermal cycling apparatus (the "Gleeble"), simulating a particular weld-heat-affected zone time-temperature history. Specimens were broken on cooling at various temperatures and for different cooling rates and strain rates. The effects of these variables on hot ductility (percent RA) were determined and related to the continuous cooling phase transformation diagram for this alloy. Both optical and scanning electron microscopy were performed to identify the plastic deformation and microscopic fracture features associated with microstructures present at time of fracture.

The most important factor affecting hot ductility was the temperature at which load was rapidly applied. Above the $\beta \rightarrow \alpha$ transformation temperature, ductility was high, between 80 and 100 percent RA, with large plastic flow exhibited by the all beta phase microstructure. Within the $\beta \rightarrow \alpha$ transformation temperature range, intermediate ductility was exhibited, 31 to 75 percent RA, with microvoids nucleating at many different locations. Between 815 and 760°C (1500 and 1400°F) just below the $\beta \rightarrow \alpha$ transformation temperature range, the lowest ductility, usually 20 percent RA, was exhibited, with fracture characterized by nucleation and coalescence of microvoids along the grain boundary alpha layer. No significant effect of strain rate on hot ductility

*Based on the paper published in Creep and Fracture of Engineering Materials and Structures, Proceedings of the Second International Conference; University College, Swansea, UK, April 1984, B. Wilshire and D.R.J. Owen, eds., Pruneridge Press, Swansea, 1984, pp. 433-450

was found. Cooling rate did not affect hot ductility significantly except for break temperatures within 100°C (180°F) below the $\beta \rightarrow \alpha$ transformation temperature range; in this region the hot ductility increased with decreased cooling rate. Of all the conditions evaluated, the lowest hot ductility, <20 percent RA, was exhibited by specimens cooled at a rate of ~45°C s^{-1} and fractured between 815 and 760°C (1500 and 1400°F). These results indicate the importance of void nucleation and growth on the hot ductility dip phenomenon where conditions obtain that suppress volume plastic flow within the prior beta grains.

3.2 BACKGROUND

The Ti-6211 alloy was developed for the U.S. Navy for use in various marine structural applications. Fabrication requirements will involve forming and joining procedures, including fusion welding, hot spinning, shear forming, forging or bending operations and various combinations of these.

As in many high strength titanium alloys, certain fabrication and processing procedures may cause cracking in the Ti-6211 alloy. An understanding of the factors affecting such cracking would provide a useful basis for either suppressing or eliminating their occurrence during fabrication. Studies conducted by the authors show that simulated weld heat-affected zone thermal cycles having peak temperatures of 1593°C (2900°F) cause a significant loss in tensile ductility when tested on cooling to between 760 and 815°C (1400 and 1500°F) (Appendices B and C). This phenomenon has been termed the hot ductility dip (HDD) phenomenon. It is important to establish whether any relationship exists between the observed loss in hot ductility and cracking induced by fabrication of mill forms or structural parts.

In the preliminary investigation of metallurgical factors affecting the HDD phenomenon in the Ti-6211 alloy, fracture in a low ductility specimen was found to occur predominantly along the prior beta grain boundaries (Section 1 and Appendices B and C). Such intergranular fracture occurs from microvoids nucleating at the edge of the grain boundary alpha layer followed by coalescence of the microvoids. Transmission electron microscopy failed to

reveal any obvious cause of such preferred crack initiation. From this study, two main metallurgical factors were proposed which could control or promote the intergranular fracture (HDD) phenomenon: (1) localized segregation of an impurity species such as sulfur, or (2) alloy partitioning on cooling below the beta transus, or a combination of both.

Microstructural study of the phases formed from beta on cooling in the Ti-6211 HDD specimens has revealed numerous, large clear-etching features distributed throughout the prior beta grains (Appendix D). One of these is lenticular in shape and has been identified as martensite; the other is irregular in shape and appears to be massive alpha.

The purpose of the present study was to evaluate the effects of cooling rate, strain rate and break temperature on the hot ductility during the cooling portion of a simulated weld heat-affected zone thermal cycle. The microstructures and fracture surfaces were studied to determine plastic deformation and microscopic fracture features associated with the specific test conditions and were related to the continuous cooling phase transformations of the alloy. From this study, a better understanding of the conditions which produce a low hot ductility in the alloy was obtained.

3.3 EXPERIMENTAL PROCEDURE

Cylindrical test specimens, 6.4 mm in diameter, were machined from the Ti-6211 alloy plate which had been beta processed and given a sub-beta anneal for 1 h at 927°C. The composition of the plate material in weight percent is as follows: 5.5Al-2.16Nb-0.94Ta-0.78Mo-<0.01Cu-<0.01Mn-<0.01Si-<0.002Y-0.4Fe-0.2Cu-0.0046H-0.066(O)-0.007N. The specimens were tested in a high-speed thermal cycling apparatus (the Gleeble) and protected from oxidation in dry argon gas. This apparatus is able to accurately simulate the time-temperature history of a location in a weld near heat-affected zone. The thermal cycle used was similar to that shown in Appendix B, Fig. 1, but having a peak temperature of 1593°C (2900°F). This hot ductility test technique selected is that developed by Nippes et al. (Refs. 14, 23 and 24).

Specimens were fractured on cooling at test temperatures ranging from well above the $\beta \rightarrow \alpha$ transformation temperature range to 760°C (1400°F) which is below the reported $\beta \rightarrow \alpha$ transformation range (Ref. 2). Various cooling rates and strain rates were included in the test conditions. The recorded time-temperature and load-time traces were analyzed to determine accurately the conditions at load application, peak load, and at fracture.

Fracture surfaces were examined in a scanning electron microscope using magnifications from 20 to 2000X. Longitudinal sections through the middle of each fractured specimen were examined using optical microscopy. Surfaces were examined in both the as-polished and etched conditions. For bright field illumination, an etching solution consisting of fluoboric acid, nitric acid, and methyl alcohol was used. For polarized light examination, electrolytic etching was performed in a chromic acid aqueous solution. See Appendix A for a complete description of the metallographic procedures used.

3.4 RESULTS

The hot ductility tests were organized into three series as follows. All tests were conducted on cooling from 1593°C (2900°F).

- Test Series 1 - The tensile load was initiated at temperatures well above the $\beta \rightarrow \alpha$ transformation range. The cooling rate was constant at 45°C (81°F) s^{-1} and the strain rate varied from 12 to 1.2 s^{-1}.
- Test Series 2 - The tensile load was initiated at temperatures within and just below the $\beta \rightarrow \alpha$ transformation range. The cooling rate was the same as in test series 1 and the strain rate was varied from 25 to 1.2 s^{-1}.
- Test Series 3 - The tensile load was initiated at temperatures above, within, and just below the transformation range. The cooling rate was varied from 23 to 7°C (45 to 12°F) s^{-1} and the strain rate was constant at 25 s^{-1}.

3.4.1 Test Series 1

The results of tests of the specimens in this series are presented graphically in Fig. 42 and include specimens FQC-40, -41 and -54. Large, uniform plastic deformation occurred in each of the specimens in this test series and resulted in extensive necking. The highest ductility, 99 percent RA, was exhibited by specimen FQC-41. Upon application of load and initial plastic deformation, the temperature of this specimen increased rapidly from 948 to 1000°C (1738 to 1832°F) then dropped off to 963°C (1765°F) at fracture. This anomalous effect is probably due to adiabatic heating during the initial plastic deformation.

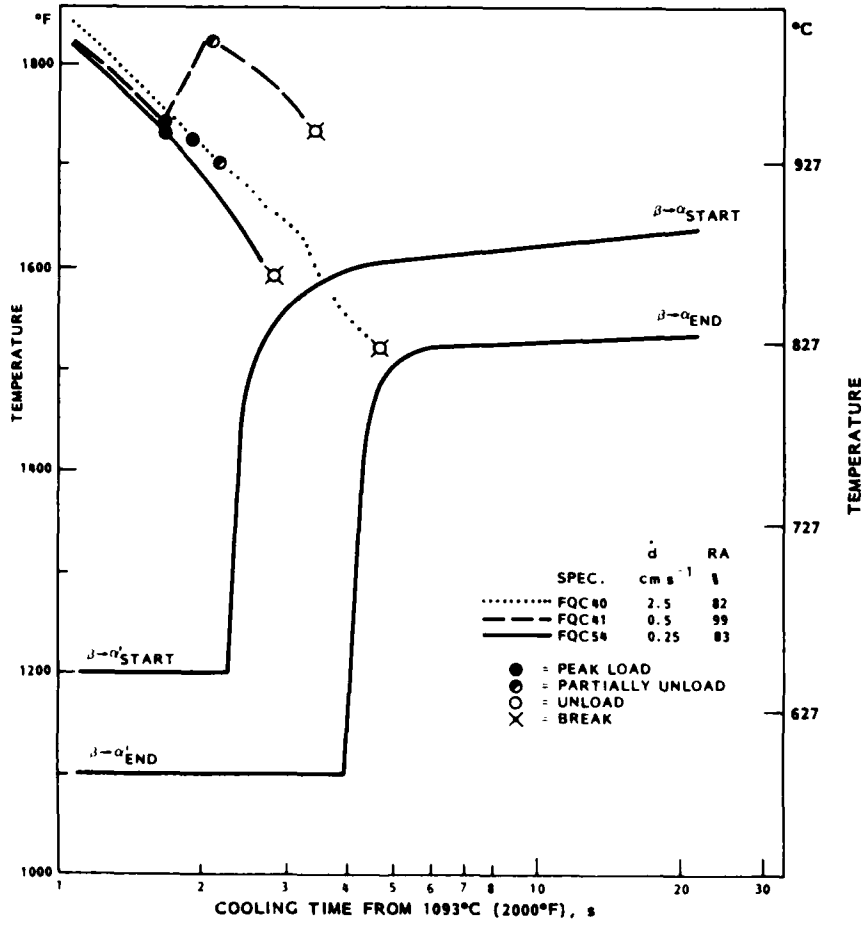

Fig. 42 On-Cooling Hot Ductility Series 1 Tests Results; The Average Cooling Rate from 1093°C (2000°F) to Load Application Was -228°C (81°F) s^{-1}. The continuous cooling transformation diagram for Ti-6211 is after Gourdine (Ref. 2).

In this series where tensile load was initiated at temperatures well above the $\beta \rightarrow \alpha$ transformation range there was no obvious effect of strain rate on the hot ductility.

3.4.2 Test Series 2

The hot ductility of the seven specimens in this test series range from 8 to 61 percent RA, see Fig. 43. The highest ductility was exhibited by specimen FQC-51 which was loaded at 848°C (1558°F) and fractured at 821°C (1510°F) relatively high in the transformation range.

Figures 44 through 47 show a number of important microstructural features of this specimen. As shown in Fig. 44, the fracture mode is a combination of both transgranular and intergranular ductile rupture. The transgranular ductile rupture is attributable to the large number of discontinuous, small and large microvoids scattered throughout the prior beta grains. (See Figs. 45, 46 and 47.) The small, scattered microvoids are often located at the boundaries between both the large lenticular martensite and massive alpha patches and the adjoining small martensite platelets. The large, scattered microvoids are at the boundary between the rather large lenticular or "rabbit-ear" shape patches and the matrix as shown in Figs. 44 and 46. These "rabbit-ear" patches have been identified as martensite (Appendix D), and in steels are sometimes called "butterfly" martensite (Ref. 25). Another microstructural feature exhibited by this specimen is extensive evidence of cross slip and wavy slip as illustrated by the distortion of many of the small martensite platelets and irregular-shape massive transformation patches shown in Figs. 44, 46 and 47.

The intergranular ductile rupture features in specimen FQC-52 are comparable to that observed in the low hot ductility Ti-6211 alloy specimens described in Appendices B and C. This fracture mechanism is characterized by microvoid nucleation along prior beta grain boundaries (actually along the interface between grain boundary alpha and the matrix), followed by coalescence.

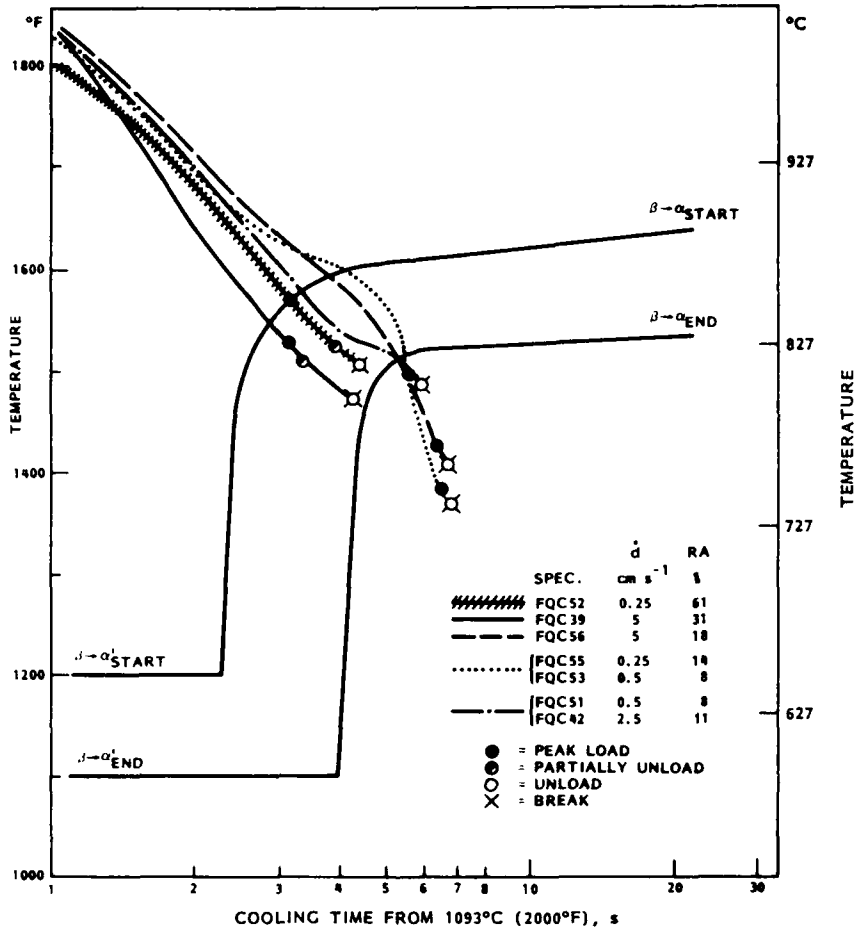

Fig. 43 On-Cooling Hot Ductility Series 2 Test Results; The Average Cooling Rate From 1093°C (2000°F) to Load Application Was -228°C (81°F) s^{-1}

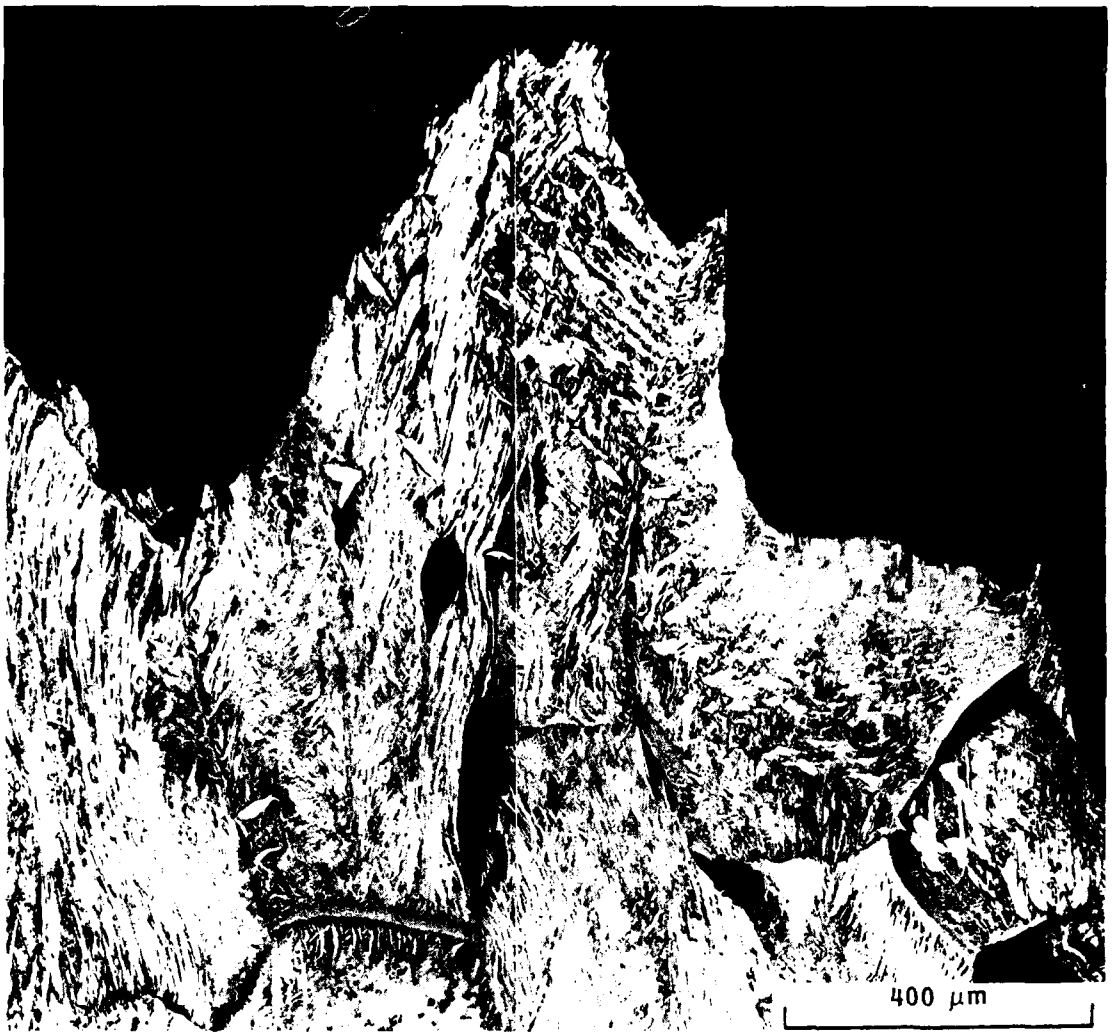

E8009, 10

Fig. 44 Optical Micrograph of Ti-6211 Hot Ductility Specimen FQC 52

Fig. 45 Optical Micrograph of Ti-6211 Hot Ductility Specimen FQC-52 Showing Numerous Small Microvoids Within the Prior Beta Grains as Well as Crack Growth Along a Prior Beta Grain Boundary

E8026

Fig. 46 Optical Micrograph of Ti-6211 Hot Ductility Specimen FQC 52 Showing a Large Microvoid Formed in the Matrix Adjacent to Large Lenticular Martensite. Note the irregular-shaped twin within the latter

Fig. 47 Optical Micrograph of Ti-6211 Hot Ductility Specimen FQC-52

Specimen FQC-39 was also loaded relatively high in the $\beta \rightarrow \alpha$ transformation range, 821°C (1510°F), but fracture was not complete until 800°C (1472°F). It was tested at a strain rate about 20 times faster than FQC-52 and the hot ductility was only half that of FQC-52, 31 versus 61 percent RA, respectively. The microscopic fracture features of specimen FQC-39 are similar to FQC-52, except the amount of intergranular fracture in the former is higher.

Specimen FQC-55 was loaded at a temperature high in the $\beta \rightarrow \alpha$ transformation range, but at the low strain rate, 1.2 s^{-1}. The maximum load did not occur until the temperature dropped to 758°C (1396°F) which is below the phase transformation range. Consequently, the hot ductility was very low, only 14 percent RA. The fracture mode is predominantly intergranular fracture along the prior beta grain boundaries, having the same microvoid nucleation and coalescence ductile rupture features previously described.

All other specimens in this series, FQC-42,-51,-53 and -56 were loaded and fractured at temperatures within -100°C (180°F) below the transformation range. The hot ductilities were low, 8 to 18 percent RA, and the fracture mode was predominantly intergranular separation along prior beta grain boundaries. See Fig. 48, for example. The predominant plastic deformation mode within the prior beta grains is twinning which occurs within the large irregular patches of massive alpha and lenticular martensite. These are shown in Figs. 49 and 50. Unlike specimens FQC-52 and -39) tested within the transformation range, there are very few microvoids that formed within the prior beta grains and there is little evidence of slip within the martensite platelets due to slip.

In test series 2, there was no significant effect of strain rate on the hot ductility.

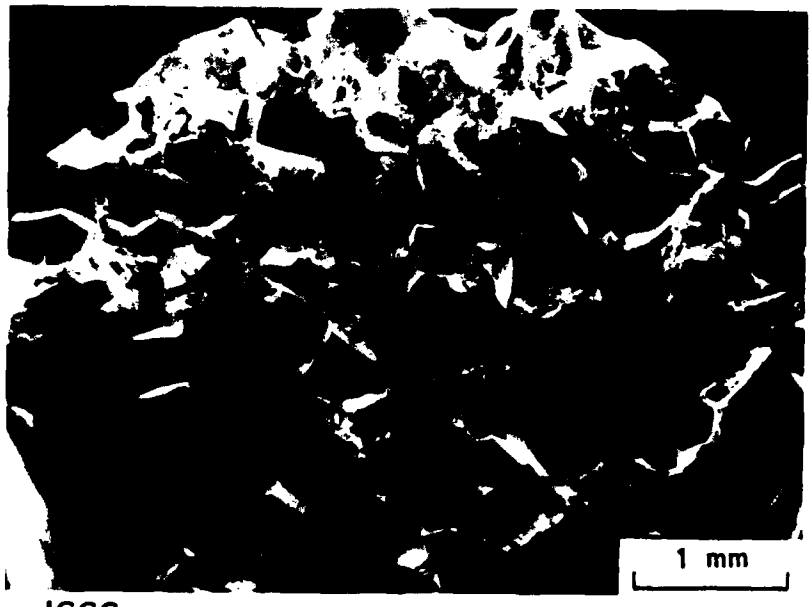

Fig. 48 Fracture appearance of Ti-6211 specimen FQC-51 after hot ductility testing about 50°C (90°F) below the beta → alpha transformation temperature range. Fracture is predominantly intergranular.

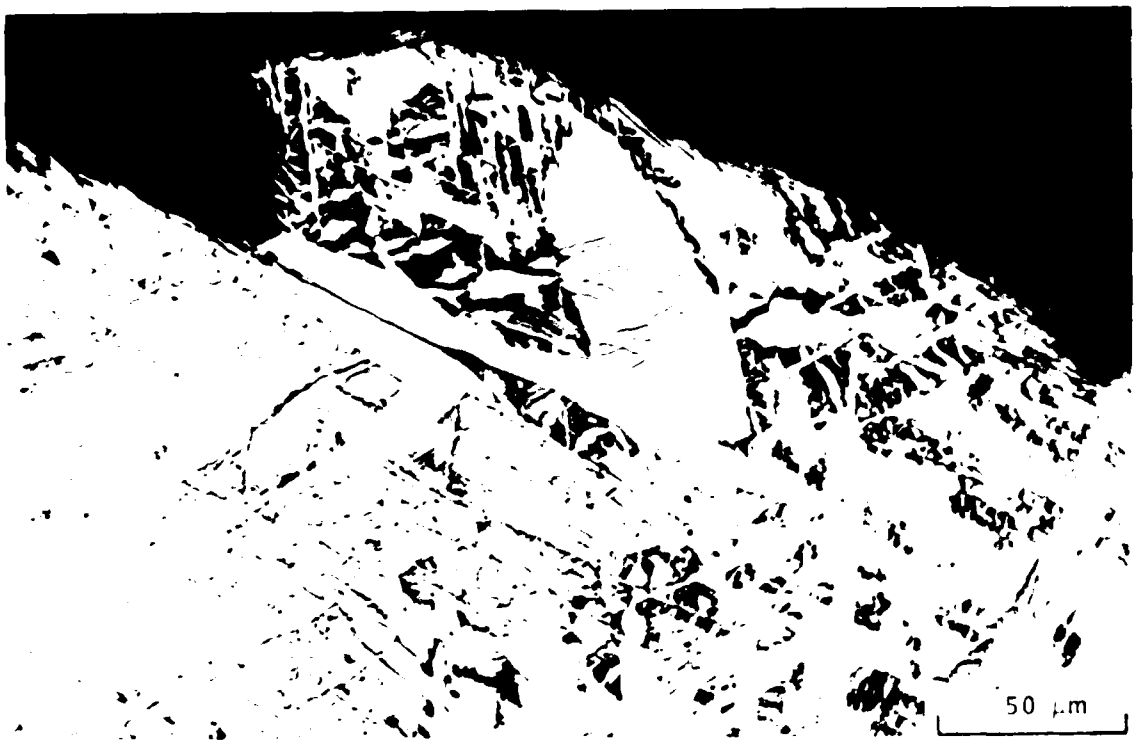

Fig. 49 Optical Micrograph of Ti-6211 Specimen FQC-51. Note extensive twinning in the large, lenticular martensite

3.4.3 Test Series 3

The five specimens in test series 3 exhibited hot ductilities ranging from 12 to 99 percent RA as shown in Fig. 51. The major test variables in this series are cooling rate and break temperature. In this test series, the peak load and fracture occurred almost simultaneously with the application of load. Consequently, the temperatures and times for peak load and fracture are almost identical.

Specimen FQC-49, tested at a temperature well above the $\beta \rightarrow \alpha$ transformation range, exhibited a high ductility, 99 percent RA. The macroscopic and microscopic deformation and fracture features of this slowly cooled specimen are closely comparable to the more rapidly cooled Series 1 test specimens, FQC-40, -41 and -54, also fractured in the single phase (beta) region.

FQC-50, the one specimen fractured within the $\beta \rightarrow \alpha$ transformation range in this series, also exhibited high ductility, 75 percent RA. Numerous microvoids

Fig. 50 Optical Micrograph of Ti-6211 Specimen FQC-56 After Hot Ductility Testing About 60°C (108°F) Below the Beta → Alpha Transformation Temperature Range, (a) Bright Field, (b) Polarized Light. Note the extensive twinning present, revealed clearly in (b)

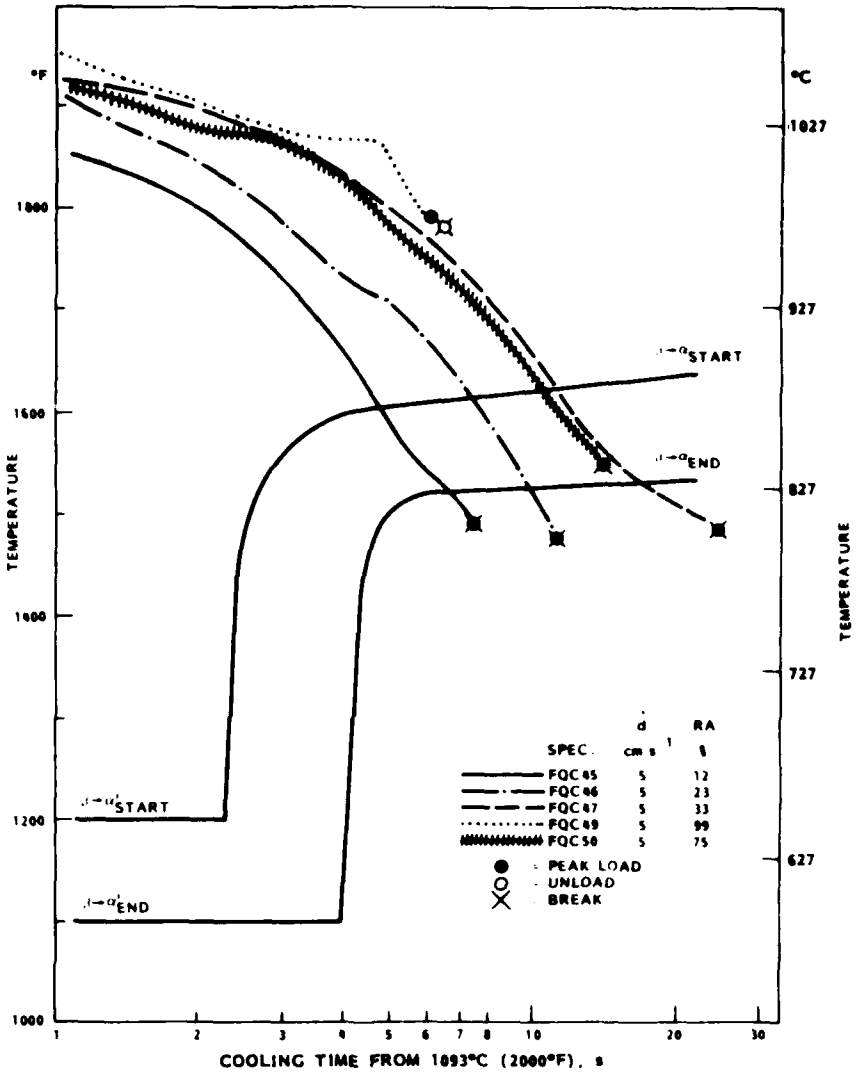

Fig. 51 On-Cooling Hot Ductility Series 3 Test Results. The average cooling rate from 1093°C (2000°F) to load application was 23, 20 and 7°C s^{-1}

were formed discontinuously, scattered along grain boundaries and within the grains. The ductility, deformation characteristics and fracture mode of this specimen closely parallel that of series 2 specimen FQC-52 which was also fractured within the β→α transformation range.

The other three specimens in this series, FQC-45, -46 and -47, were all tested at temperatures within 100°C (180°F) the transformation range. All exhibited rather low ductility, 12 to 33 percent RA. In each case, the predominant fracture mode is intergranular along prior beta grain boundaries, but with a decreased cooling rate there is increased evidence of plastic deformation by slip. Also, the twinning observed in the large lenticular martensite and massive alpha patches is different in the slowly cooled specimens. There are fewer twins, their thickness-to-length ratio is higher, and they show significantly more evidence of superimposed slip deformation than the faster cooled series 2 specimens tested at temperatures just below the $\beta \rightarrow \alpha$ transformation range. For example, compare Fig. 50 with Figs. 52 and 53.

Some of the microstructural features in the deformed region adjacent to the fracture surface are quite unusual. One of these features is shown in Fig. 54, where an array of lenticular features traverses a prior beta grain boundary. These features are believed to be deformation twins which have partially dissipated at high temperature immediately after fracture occurred in the hot ductility test.

Thus, the effect of decreased cooling rate for specimens fractured in tension at temperatures just below the $\beta \rightarrow \alpha$ transformation range is to increase the hot ductility. This is apparently due to increased plastic deformation by slip within the grains, rather than a shift in fracture mode. Note also that this increase in slip occurs at a relatively high strain rate, 25 s^{-1}.

A variation in strain rate was not included in the test conditions for the series 3 specimens. Consequently, only a limited evaluation of this factor can be made by comparing the results with similar tests conducted in the other two series. Such evaluation does not result in any obvious or consistent correlation of ductility with strain rate.

Fig. 52 Optical Micrograph of Ti-6211 Specimen FQC-46 After Hot Ductility Testing. Note the irregular shape of deformation twins in the large, clear-etching patch (massive alpha)

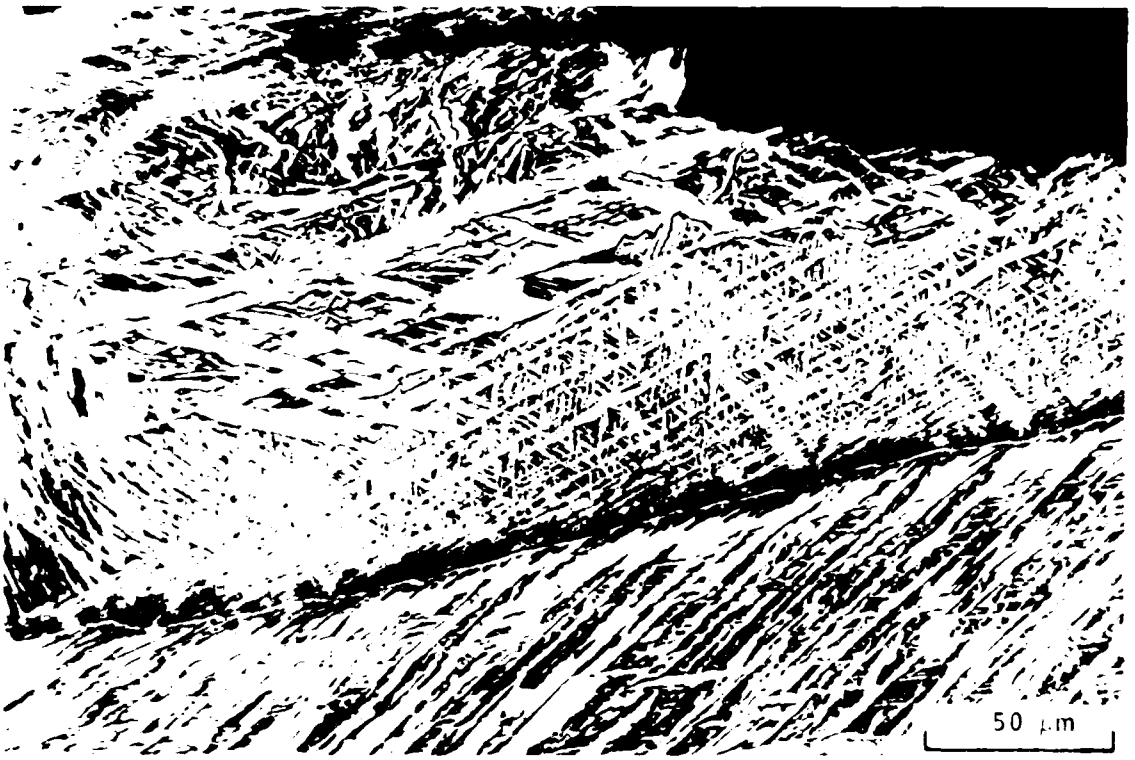

Fig. 53 Optical Micrograph of Ti-6211 Specimen FQC-47 After Hot Ductility Testing. Note array of slip bands above the prior beta grain boundary. The tensile axis is vertical

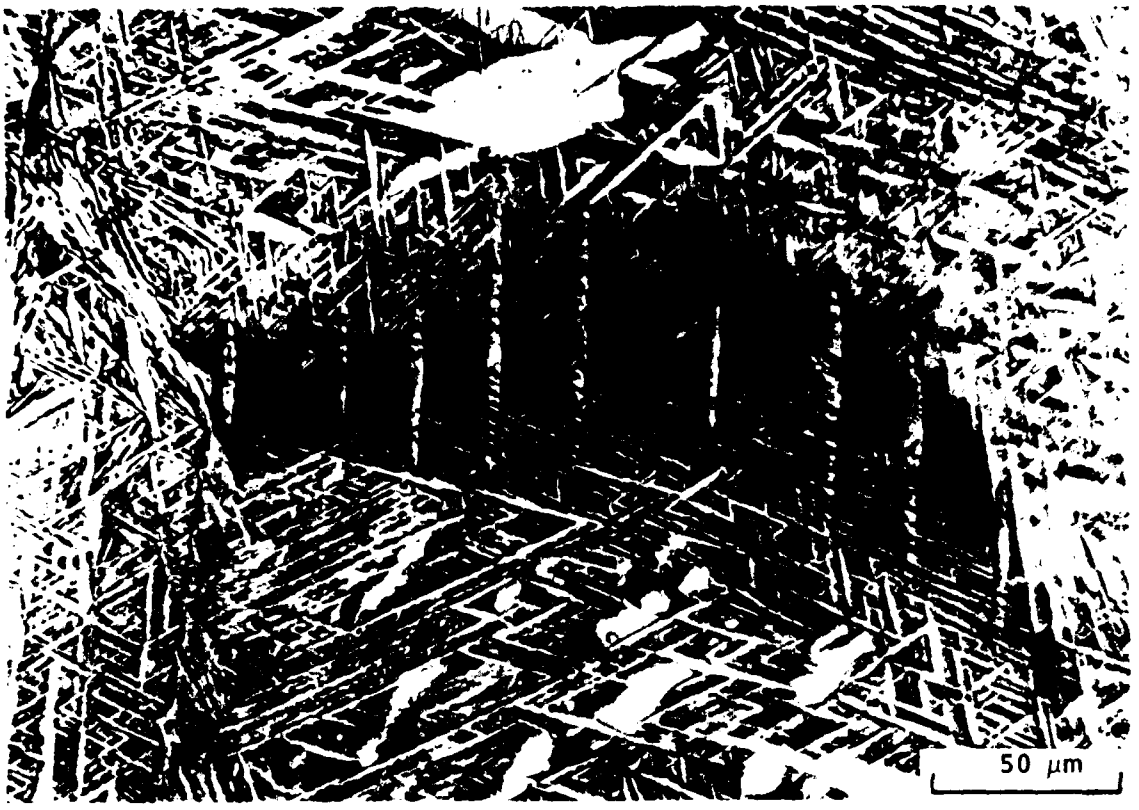

Fig. 54 Optical Micrograph of Ti-6211 Specimen FQC-47 After Hot Ductility Testing. Note array of lenticular features traversing the prior beta grain boundary. These are believed to be deformation twins which have partially dissipated.

3.5 DISCUSSION

Discussion of the results is organized into three parts with respect to the continuous cooling transformation characteristics of the alloy: hot ductility test conducted above the $\beta \rightarrow \alpha$ transformation range; within the transformation range, and just below the transformation range.

3.5.1 Hot Ductility Above the $\beta \rightarrow \alpha$ Transformation Range

The on-cooling hot ductility in this temperature range is as expected - high ductility (>80 percent RA) due to large plastic deformation of the large grained, ductile body centered cubic beta phase and with no evidence of intergranular microvoid nucleation or fracture. There is no significant effect of the variation in cooling rate from 45 to 7°C s^{-1} or strain rate from 1.2 to 25 s^{-1} on the hot ductility of Ti-6211. Significantly higher or lower cooling rates or strain rates could conceivably alter the hot ductility but would not be representative of fabrication processes likely to be used.

3.5.2 Hot Ductility Within the $\beta \rightarrow \alpha$ Transformation Range

The on-cooling hot ductility in this transformation range exhibits a lower ductility than above the $\beta \rightarrow \alpha$ transformation range and a higher ductility than just below the $\beta \rightarrow \alpha$ transformation range. For a constant cooling rate, the ductility decreases with decreasing test temperature. A major source contributing to ductility within the transformation range is the low flow strength of the highly ductile beta phase matrix surrounding the grain boundary alpha layer, the large lenticular martensite, massive alpha patches, and finer features. The latter includes colonies of nucleation and growth transformation (N&GT) alpha platelets adjacent to some portions of the grain boundary alpha and martensite throughout the remainder of the matrix. The untransformed beta phase at these high temperatures acts to accommodate an imposed tensile load by large plastic flow so that the strain localization at phase interfaces is relatively low but increases with decreasing test temperature. The stresses are high enough at some interface locations to

nucleate voids, some of which coalesce to form short cracks preferentially at the edge of tne grain boundary alpha layer. At the same time, extensive plastic flow occurs throughout the matrix. These two competitive processes result in tne observed mixture of intergranular and transgranular ductile rupture.

Very few deformation twins were observed in the large, clear-etching patches (large lenticular martensite and massive alpha) distributed throughout the prior beta grains in these specimens. The major reason for this is that in this particular test temperature range, the shear strength of the large patches is apparently low. As seen in Fig. 47, the large amount of plastic deformation in the massive alpha patches and the martensite platelets indicates these microstructural features were formed high in the $\beta \rightarrow \alpha$ transformation range. For example, specimen FQC-52 was broken on cooling at 948°C (1558°F) and at a cooling rate of 45°C (81°F) s^{-1}. This temperature is close to the beginning of the $\beta \rightarrow \alpha$ transformation reported by Gourdine (Ref. 2). Thus, on cooling at 45°C (81°F) s^{-1} from the beta phase field, the large, lenticular martensite and the massive alpha are believed to form at about the same time as tne grain boundary alpha layer.

Microstructural features are similar in both the fast- and slow-cooled samples, witn some notable exceptions. The slow-cooled specimen has extensive colonies of N&GT alpha platelets distributed along the length and on both sides of the grain boundary alpha layer. In the fast cooled specimen [45°C (81°F) s^{-1}], colonies of this type and location were either not seen at all or were uncommonly seen. Thus, the planar interface between alpha formed at the prior beta grain boundaries in the fast-cooled specimens did not form in the slow-cooled specimen. In the slow-cooled case, the interface between the grain boundary alpha and the beta matrix was highly irregular and serrated due to tne extensive formation on cooling of the N&GT alpha platelet structure.

A second difference in microstructure between the fast and slow cooled specimens is the fineness and morphology of the last-to-transform microstructure. In the fast-cooled specimen, this structure is comprised of

narrow, lenticular martensite. In contrast, the structure in the slow-cooled specimen is coarser and may be a mixture of martensite and N&GT alpha or all N&GT alpha.

Both of the above two microstructural features unique to the slow-cooled specimen may contribute to a higher plastic strain to fracture. First, the formation of N&GT colonies adjacent to the prior beta grain boundary alpha layer probably improves the cohesive strength of the grain boundary alpha/matrix interface as a result of the geometric irregularity. Second, the cooling rate would affect the solute distribution on either side of the grain boundary alpha/beta matrix as a result of alloy partitioning, with the slower cooling rate expected to have a closer equilibrium distribution. Third, the coarser size and presence of N&GT alpha platelets distributed throughout the prior beta grains in the slow-cooled material improve the hot ductility because the slip distances within the matrix are increased. Also, the flow strength of the N&GT platelet structure is probably lower than the martensite platelet structure at the same high temperature.

The results in this test series suggest that a high hot ductility can be enjoyed by avoiding the application of high tensile loads at temperatures within 100°C (180°F) below the $\beta \rightarrow \alpha$ transformation range. This should be considered when undertaking manufacturing processes such as rolling, forging, or spinning.

3.5.3 Hot Ductility Within 100°C (180°F) Below the $\beta \rightarrow \alpha$ Transformation Temperature Range

The on-cooling hot ductility in this temperature range is the lowest exhibited by the Ti-6211 alloy (excluding the low hot ductility close to the melting point) and exemplifies the HDD phenomenon. Microvoids nucleate along much of the grain boundary alpha/beta matrix boundary and coalesce to form continuous cracks along the prior beta grain boundaries. This fracture sequence is similar to that exhibited by many single phase metals where at high temperature voids form along grain boundaries (Ref. 26). A number of factors may have an important contribution to this localized fracture mode. One

factor can be the segregation of alloying elements on either side of the interface due to partitioning of solute during planar growth of the grain boundary alpha phase upon cooling from the beta phase. Such segregation can locally affect the flow strength of both phases, thereby affecting the degree of strain localization and which, in turn, affect the nucleation and growth of voids at the interface.

The flow strength of the region within each prior beta grain at the break temperature is an important factor affecting void nucleation and growth at the grain boundary alpha-matrix interface. Below about 815°C (1500°F) the gross section fracture strength of Ti-6211 increases significantly with decreasing temperature as shown in Fig. 12 of Appendix B. The highest rate of change, however, occurs between 1000 and 815°C (1832 and 1500°F). In this range, beta is transforming on cooling to both alpha and martensite, which increases the flow strength of the prior beta grain. Below about 815°C (1500°F), the flow strength continues to increase, probably due to an increase in the critical resolved shear strength of each of the phases present. This increase in strength is probably the reason for the deformation twinning observed in the large lenticular martensite and massive alpha phases of specimens broken just below the $\beta \rightarrow \alpha$ transformation range, and illustrated in Fig. 50. Twinning in these phases would increase their resistance to slip, as twin boundaries inhibit dislocation glide as effectively as a grain boundary.

The critical range of break temperature for low hot ductility (<20 percent RA) is indicated as Zone A in Fig. 55. In this zone, the cooling rate has a moderate effect on hot ductility, as described above. Individual HDD data for specimens exhibiting hot ductilities greater than 20 percent RA are also included in this figure. Using all the data, four zones of hot ductility are proposed. The hot ductility zones relate to Gourdine's continuous cooling transformation diagram for Ti-6211 (Ref 2.). The resulting relationship is not unexpected as the on-cooling hot ductility is clearly related to the amount and kind of phases present. Gourdines's work, however, did not recognize on-cooling transformations from the beta phase to either the large, lenticular martensite or the large irregular patches of massive alpha, as

observed in the present study. The formation of these phases at cooling rates of 45°C (81°F) s^{-1} and slower is indicative of an unusually high degree of metastability of the beta phase in the Ti-6211 alloy. The metastability associated with these cooling rates may be described as a highly competitive process where the beta phase can transform on cooling to (1) alpha at the prior beta grain boundaries, (2) large, lenticular martensite at heterogeneous locations within the prior beta grains, (3) large, irregular patches of massive alpha also at heterogeneous locations within the prior beta grains, and (4) nucleation and growth transformation alpha platelets adjacent to some portions of the grain boundary alpha layer.

3.6 CONCLUSIONS

The following conclusions are based on the results of hot ductility tests for Ti-6211, tested on cooling from a peak temperature of 1593°C (2900°F) in a simulated weld thermal cycle, with break temperatures from 763 to 1015°C, (1405 to 1860°F) cooling rates from 7 to 45°C (12 to 81°F) s^{-1}, and estimated strain rates from 1.2 to 25 s^{-1}.

1. The hot ductility is affected primarily by break temperature, with high ductility exhibited above the $\beta \rightarrow \alpha$ transformation temperature range, intermediate ductility within the transformation range, and low ductility within 100°C (180°F) below the transformation range.

2. Cooling rates between 7 and 45°C (12 and 81°F) s^{-1} do not affect hot ductility above the $\beta \rightarrow \alpha$ transformation range and have only a moderate effect on ductility within and just below this range, where a slower cooling rate increases ductility.

3. Regardless of test temperature, strain rates between 1.2 and 25 s^{-1} have little effect on hot ductility.

4. The critical microstructural feature affecting low hot ductility is the interface between the prior beta grain boundary alpha layer and the matrix. This interface is the preferred site for void nucleation and coalescence. Void coalescence results in intergranular cracking and separation, the predominant fracture mode just below the $\beta \rightarrow \alpha$ transformation temperature range.

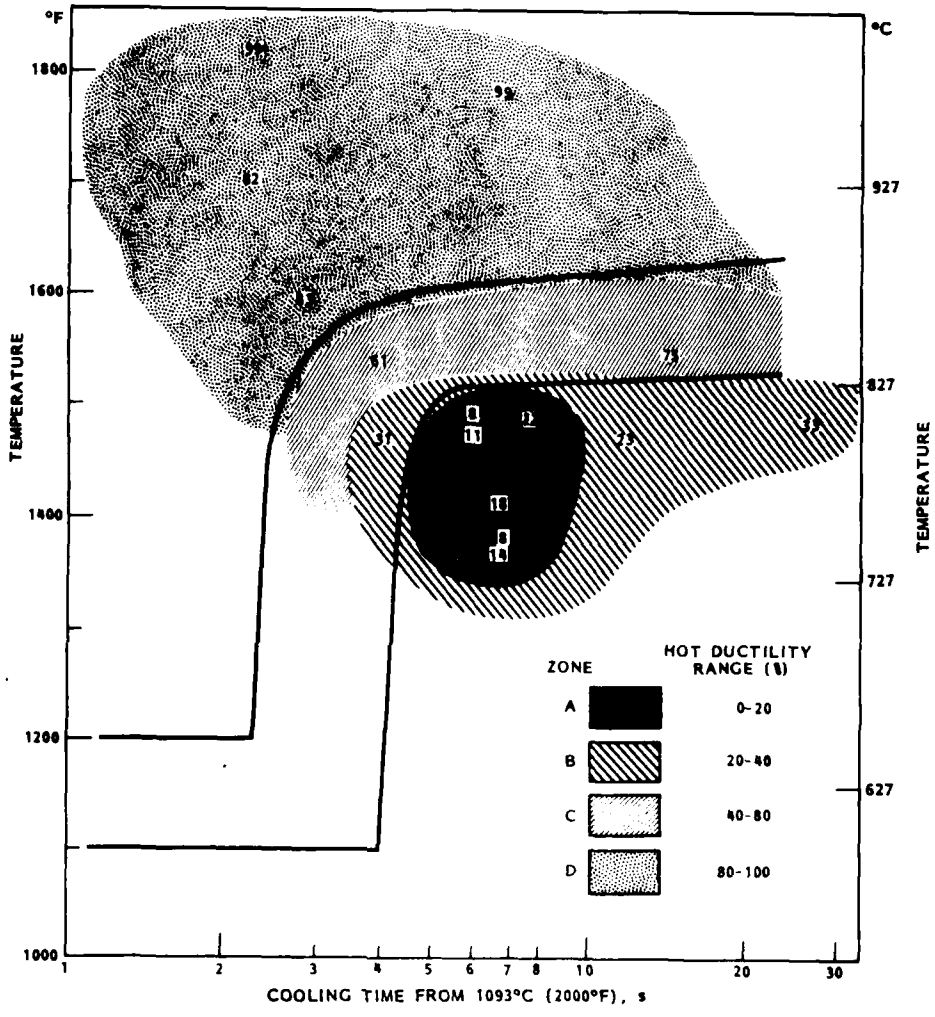

Fig. 55 On-cooling Hot Ductility of the Ti-6211 alloy, Based on Results in the Present Study. Four zones are proposed, one for each major range of not ductility. The numbers appearing in the figure are percent reduction in area values for individual test specimens

Section 4
SURFACE SEGREGATION STUDIES

4.1 INTRODUCTION

Prior gain boundary fracture surface analysis studies of the Ti-6211 alloy subjected to treatment in the hot-ductility minimum temperature and fractured at room or lower temperatures indicated the presence of sulfur at prior beta grain boundaries. See Section 1 and Appendices B and C, for example. These observations suggested that sulfur plays a deleterious role on the hot ductility of this alloy by segregating to grain boundaries. The hot ductility phenomenon was pronounced, however, only when fractured in tension within a narrow temperature range. The direct evidence of the role of sulfur in the hot ductility phenomenon would thus require AES examination of grain boundaries of specimens subjected to fracture at high temperature.

Grain boundaries and surfaces, both being highly energetic interfaces, behave much alike in many respects, particularly in their solute segregation behavior. Solute segregation to surfaces has generally been found to be qualitatively similar to segregation at grain boundaries. The term qualitative is used here to indicate that the nature of alloying elements and temperature ranges at which segregation occurs is analogous for both surfaces and grain boundaries. In the few systems explored previously, quantitative surfaces segregation of selected solutes has been found to be higher than corresponding grain boundary segregation (Refs. 27 to 29). This may be explained on the basis that surface energies are generally higher than average grain boundary energies. Experimentally, the surface segregation studies are less cumbersome and can be interpreted with less complexity than the grain boundary segregation studies requiring fracture at high temperatures. When fresh surfaces are exposed at high temperature, they are subject to solute segregation, which in itself requires an understanding and be distinguished from segregation that may have occurred just prior to fracture. Thus,

understanding the surface segregation behavior of solute elements is a necessary prerequisite to complete the understanding of grain boundary segregation occurring at high temperatures. These segregation studies have the following objectives:

1. To understand the nature of surface segregation, viz., the type of solutes and temperatures at which segregation becomes predominant, so tnat their tendency toward grain boundary segregation may be deduced.
2. To understand the interactions (Refs. 29, 30) among solute elements and with alloying elements, as these factors strongly influence grain boundary segregation. Of particular interest to the subject study is to understand any interactions present between sulfur and yttrium. If they have attractive interaction it may be expected that segregation of one of the elements is likely to enhance the segregation of the other. The converse is also true. Examples of these include attractive interactions exhibited by nickel and antimony in low alloy steels (Ref. 31) and sulfur and calcium in nickel (Ref. 29). Repulsive interactions are exhibited between silicon, sulfur, and phosphorous in 304 stainless steels (Ref. 32) as well as sulfur and carbon in nickel (Ref. 29).
3. To provide basic information on the surface segregation kinetics, information that is necessary for correctly interpreting any high temperature grain boundary segregation study in this or related alloys. Specific interest is to learn how rapidly the segregation of sulfur occurs at freshly formed hot fracture surfaces and to distinguish it from that present at grain boundaries just prior to fracture.

4.2 EXPERIMENTAL PROCEDURE

The experiments were conducted at an ultrahigh vacuum in the Perkin Elmer model PHI 560 ESCA/SAM surface analysis system. The specimen introduction stage was used to manipulate an in situ specimen heater, consisting of a tantalum ribbon heater 12.7 mm long x 25.4 μm thick x 3.175 mm wide (0.5 x 0.001 x 0.125 in.) on which a specimen was directly spot welded. Specimens

from various Ti-6211 alloys were cut into shapes approximately 1 cm x 1 cm x 1 mm (0.394 x 0.394 x 0.394 in.). The specimen temperatures were read directly using a Pt-Pt/10 Rh thermocouple spot welded to the top surface of the specimen. Surface analyses were conducted using Auger electron spectroscopy (AES) or x-ray photoelectron spectroscopy (XPS or ESCA) from a region adjacent to the thermocouple weld. AES was used for rapid determination of surface compositional changes during heating and for obtaining compositional-depth profile after cooling to room temperature. XPS was used to determine the chemical state of surface species, for example, whether sulfur was present in an elemental or a sulfide form. The studies were conducted using specially modified Ti-6211 alloys designated herein 20056-3B (containing, by weight, 20 ppm sulfur and 71 ppm yttrium) and 20057-3A (containing 60 ppm sulfur and 74 ppm yttrium). See Appendix F for the detailed metallurgical processing history and chemistry of these alloys.

4.3 EXPERIMENTAL RESULTS

4.3.1 Kinetics of Segregation

Figure 56 shows typical AES peak-to-peak height segregation data obtained from the 20057-3A alloy at 800°C (1472°F). The sulfur concentration rises to near its maximum value (estimated at 33 atomic percent) using elemental sensitivity factors (Ref. 33) in approximately 2 min. Yttrium segregation occurred only in specimens heated to higher temperatures. Figure 57 shows the summary of sulfur and yttrium surface concentration maxima (t_{max} < 30 min) observed at heating temperature in the alloy 20057-3A. Observable sulfur segregation occurs at temperatures as low as 400°C (752°F). The sulfur segregation rate increases rapidly to the highest temperature examined, 1100°C (1832°F); the reliable data [up to 900°C (1652°F)] is shown in Fig. 58. At high surface coverages, typically over 10 atomic percent, the coverage rate (not shown) decreases. At temperatures of 800°C (1472°F) and above, the maximum coverage by sulfur (see Fig. 57) is actually lower than that occurring at 700°C (1292°F) and is coincidental with the increase in yttrium surface coverage.

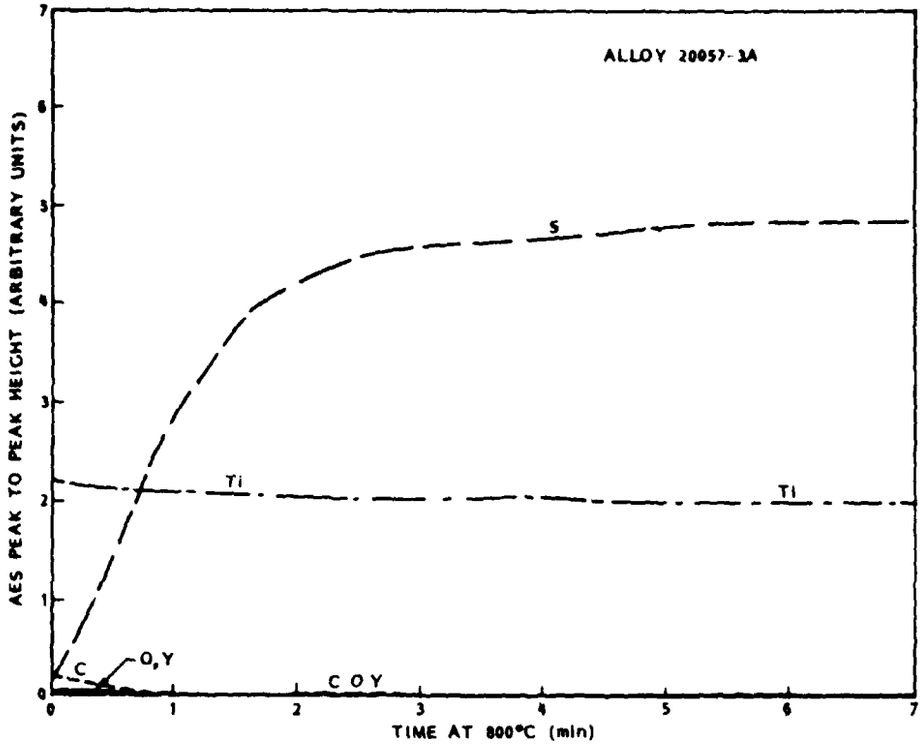

Fig. 56 Variation in Surface Composition of Ti-6211 Alloy Specimen 20057-3A With Time at 800°C (1472°F) as Measured by AES

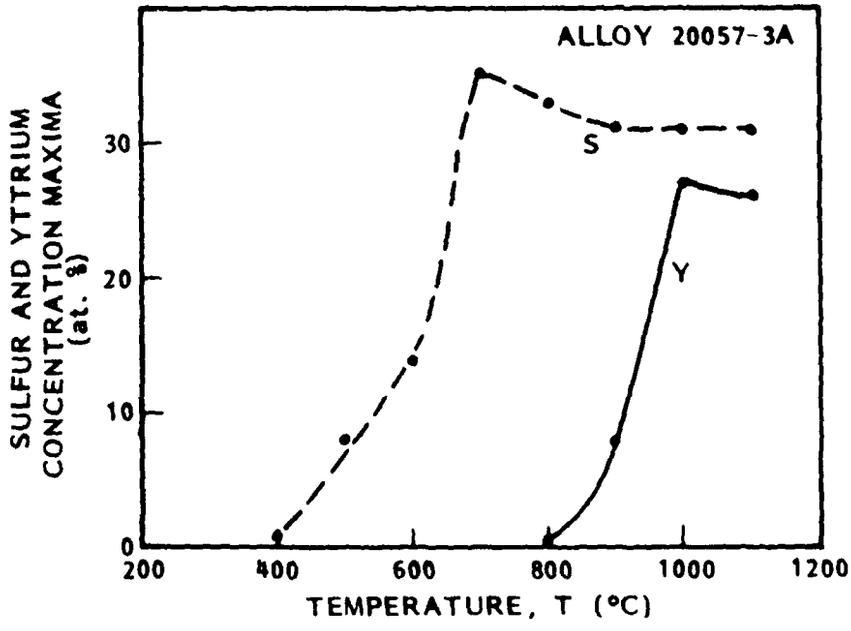

Fig. 57 Sulfur and Yttrium Concentration Maxima as a Function of Temperature in Alloy 20057-3A

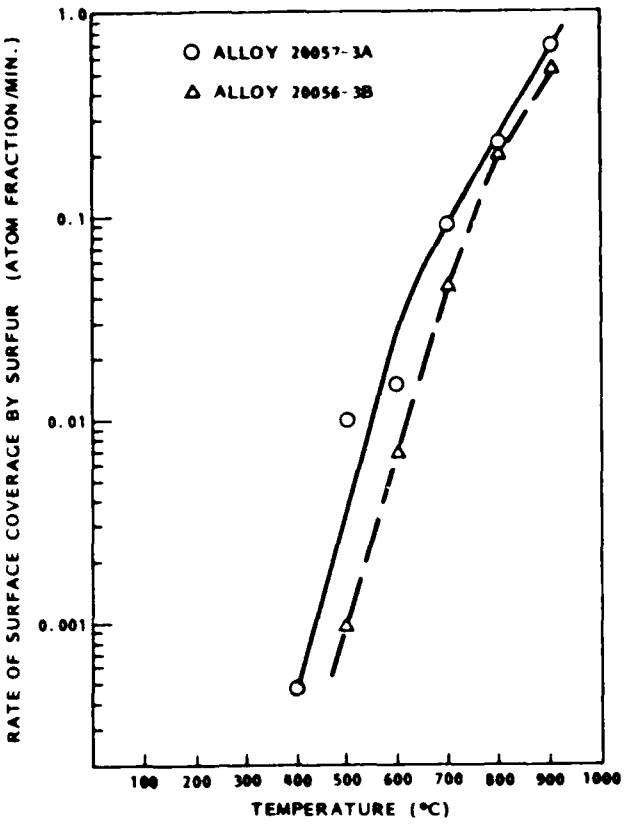

Fig. 58 Initial Rate of Surface Segregation of Sulfur as a Function of Temperature

Since no other elemental segregation is observed, these results suggest surface accommodation by sulfur for yttrium. Assuming that the driving force for segregation in this case is the lowering of surface free energy, it follows that yttrium apparently fits surface sites better and lowers the surface energy to a greater degree than does sulfur in this temperature range. This aspect and its implications on yttrium grain boundary segregation and influence on mechanical properties are discussed below. The absence of collaborative segregation of sulfur and yttrium suggests the absence of attractive atomic interactions between sulfur and yttrium.

4.3.2 Nature of Segregation

To study the segregation kinetics after heating to high temperature, each specimen was cooled to room temperature and the surface chemistry was examined in detail using AES and XPS. An XPS spectrum from the surface of the 20056-3B

specimen cooled after holding at 1000°C (1832°F) for 7 min. is shown in Fig. 59. Segregation of yttrium and sulfur are evident in the top spectrum, as compared to the bottom one, obtained from the same surface after sputtering 1.4 nm. AES depth profiles, obtained in selected specimens (example shown in Fig. 60) are in agreement with XPS data and indicate sulfur and yttrium are localized to within 1.0 nm of the surface, possibly as little as one atomic layer. The high resolution XPS S_{2p} peak indicates that sulfur is present in a sulfide form (probably TiS). The XPS Y_{3d} peaks indicate that yttrium is at the surface in an oxide form. AES data obtained immediately after cooling suggest, however, that yttrium is in an elemental form. Since yttrium segregation occurred in atomic dimensions and since no segregation of oxygen was observed, it is concluded that yttrium segregates in elemental form and oxidizes subsequently upon holding at room temperature.

4.4 SUMMARY

These studies indicate that, upon heating, sulfur and yttrium both segregate readily to free surfaces, with sulfur segregation becoming predominant above 400°C (752°F) and yttrium segregation being predominant above 800°C (1472°F). Both elements segregate in their atomic form, but sulfur forms a surface sulfide phase (TiS, most likely). No attractive interaction was observed between the two elements. Yttrium appears to displace sulfur present at the surface, indicating that in the 800 to 1100°C (1472 to 2012°F) range yttrium more readily lowers the surface free energy than does sulfur. If a similar interaction were to occur at grain boundaries, the presence of yttrium in the alloy would be expected to result in grain boundary segregation of yttrium in that temperature range, thereby reducing the deleterious effect of sulfur in the hot ductility behavior. This may explain the beneficial role of yttrium in this alloy in increasing the hot ductility as described in Section 2 and Appendix C. Another possible explanation involves the presence of some of the yttrium in the form Y_2O_3 as a fine dispersoid, which would provide additional interfaces for the segregation of sulfur and result in a net lowering of sulfur segregation at the beta grain boundaries. This latter hypothesis may be examined by further segregation studies of compositions

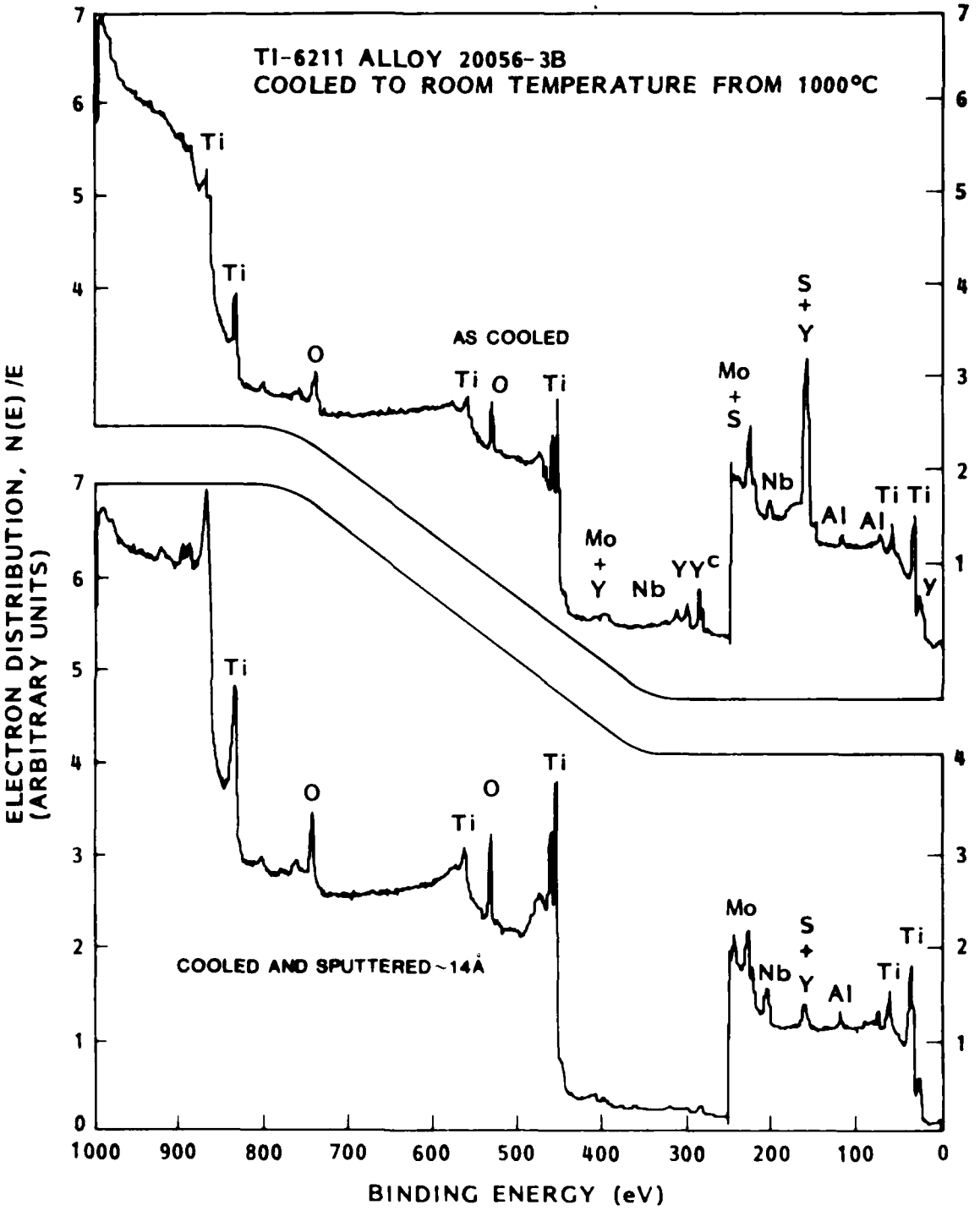

Fig. 59 XPS Spectra of a Ti-6211 Alloy 20056-3B Cooled From 1000°C (Holding Period 7 Minutes) and After Sputtering about 1.4 nm From the Surface

involving no yttrium additions and comparison of the results with the present studies. TEM examination is also likely to aid in understanding whether or not dispersions of Y_2O_3 are present in the alloy.

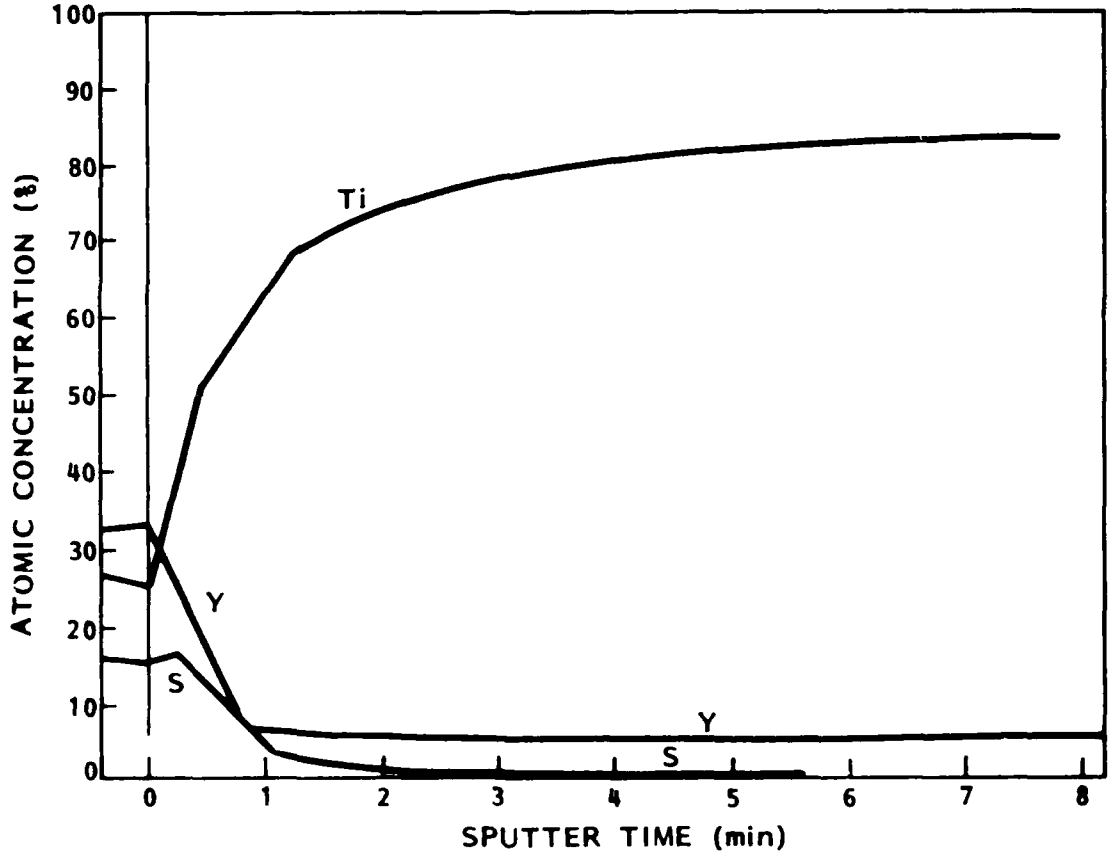

Fig. 60 AES Depth Profile of Ti-6211 Alloy Specimen 20057-3A Cooled From 1100°C (2012°F). Estimated Sputtering Rate about 1.4 nm/min for Ta_2O_5 Standard

Section 5
CONCLUSIONS

1. A low hot ductility (0 to 20 percent RA) occurs in the Ti-6211 alloy when fractured in tension in the temperature range 760 to 843°C (1400 to 1550°F) upon cooling from above 1204°C (2200°F) in the first thermal cycle or on heating from RT on a second thermal cycle.

2. The fracture mode associated with the hot ductility dip (HDD) phenomenon is microvoid nucleation and coalescence preferentially at the interface between the grain-boundary alpha and the beta matrix, resulting in intergranular ductile rupture along prior beta grain boundaries. This fracture surface has a sulfur concentration of over 300 times the bulk concentration, but is limited to a few atom layers deep.

3. Ti-Al alloys otner than Ti-6211, namely Ti-6Al and Ti-6Al-4V, appear to exhibit a similar, but not so severe, HDD phenomenon.

4. A small amount (150 ppm) of yttria added to the melt in Ti-6211 significantly increases the tensile ductility (RA) in Ti-6211, tested in a manner which normally produces a low hot ductility.

5. XPS and AES analyses of free surfaces in Ti-6211 heated in situ at 10^{-10} torr indicates that sulfur segregation becomes predominant above 400°C (752°F). When yttrium is present, it segregates predominantly above 800°C (1472°F), and appears to displace sulfur at the surface, and without attractive interaction.

6. The phase transformations occurring in Ti-6211 when tested to produce a low hot ductility during simulated weld heat-affected zone thermal cycles include (a) large lenticular martensite platelets, including the "butterfly" martensite morphology, and (b) large, irregular,

clear-etching patches of alpha, believed to be massively transformed. Both of these transformation products twin profusely when tested in tension in the low hot ductility temperature region.

Section 6
REFERENCES

1. Private Communication, J. Cavallaro and F. Lengenfelder, DTNSRDC-Annapolis.

2. J. Gordine, Welding J., 53, Res. Suppl., March 1974, p. 117-s.

3. Private Communication, I. L. Caplan, DTNSRDC-Annapolis.

4. F. A. Crossley and R. E. Lewis, "Correlation of Microstructure With Fracture Toughness Properties in Metals," Report No. LMSC-D346114, Lockheed Palo Alto Research Laboratory, Palo Alto, California, to Naval Air Systems Command. Contract N00019-72-C-0545, 30 September 1973.

5. J. C. Chesnutt, J. D. Frandsen, A. W. Thompson, and J. C. Williams, "Influence of Metallurgical Factors on the Fatigue Crack Growth Rate in Alpha-Beta Titanium Alloys," Quarterly Report (Oct. 1, 1974 to December 31, 1974) on Contract F33615-74-C-5067, Rockwell International Science Center, Thousand Oaks, California, p. 2.

6. N. E. Paton, J. C. Williams, J. C. Chestnut, and A. W. Thompson, "The Effects of Microstructure on the Fatigue and Fracture of Commercial Titanium Alloys," Specialists Meeting on Alloy Design for Fatigue and Fracture Resistance, Brussels, Belgium, 13-19 April 1975, AGARD Conference Proceedings No. 185, p. 4-1.

7. C. G. Rhodes, and J. C. Williams, "Observations of an Interface Phase in the α/β Boundaries in Titanium Alloys," Met. Trans., 6A, 1975, p. 1670.

8. M. Hansen, Constitution of Binary Alloys," Second Edition, McGraw-Hill Book Co., N.Y., 1958, p. 1167.

9. G. Hägg and N. Schönberg, Archiv Kemi, 7, 1954, p. 371.

10. R. M. Goldhoff, H. L. Shaw, C. M. Craighead, and R. I. Jaffee, Trans. ASM, 45, 1957, p. 941.

11. L. W. Berger, D. N. Williams, and R. I. Jaffee, Trans. ASM, 49, 1957, p. 300, discussion p. 312.

12. R. P. Elliott, Constitution of Binary Alloys, First Supplement, McGraw-Hill Book Co., N.Y., 1965, p. 795.

13. S. F. Bartram, Ph.D. Thesis, Rutgers University, 1958.

14. E. F. Nippes, W. F. Savage, H. F. Mason, B. J. Bastien and R. Curran, Welding Journal, 34, Res. Suppl., April 1955, p. 183-s.

15. Unpublished research, DTNSRDC-Annapolis.

16. Private communication, W. Lukens, DTNSRDC-Annapolis, Md.

17. R. E. Lewis and K. C. Wu, Welding Journal, 42, Res. Suppl., June 1963, p. 241-s.

18. F. H. Froes, J. C. Chestnutt, C. G. Rhodes, and J. C. Williams, Toughness and Fracture Behavior of Titanium, ASTM STP 651, American Society for Testing and Materials, 1978, p. 115.

19. G. R. Yoder and D. Eylon, Met. Trans., 10A, 11, November 1979, p. 1808.

20. Private Communication, A. Joshi, Lockheed Palo Alto Research Laboratory, Palo Alto, CA.

21. Private Communication, B. B. Rath, U.S. Naval Research Laboratory, Washington, D.C.

22. H. Kanyo, T. Amano, and S. Yajima, Titanium Science and Technology, Plenum Press, 3, 1973, p. 1869.

23. E. F. Nippes and W. F. Savage, Welding J., 1949, 28, Res. Suppl., p. 534-s.

24. E. F. Nippes, L. L. Merrill and W. F. Savage, Welding J., 28, Res. Suppl., 1949, p. 556-s.

25. A. Entwisle, University of Sheffield, private communication. See also Department of Metallurgy, University of Sheffield Research Review 1965 - 74, p. 22.

26. A. W. Mullendore and N. J. Grant, Deformation and Fracture at Elevated Temperatures, N. J. Grant and A. W. Mullendore, eds., M.I.T. Press, 1965, p. 165.

27. M. P. Seah and C. Lea, Phil. Mag., 31, 1975, p. 627.

28. A. Joshi, unpublished research.

29. A. Larere, M. Guttmann, P. Dumoulin and C. Roques-Carmes, Acta. Metall., 30, 1982, p. 685.

30. M. Guttmann and D. McLean, "Interfacial Segregation," Eds., W. C. Johnson and J. M. Blakely, ASM, 1977.

31. A. Joshi, Scripta Metall., 9, 1975, p. 251.

32. A. Joshi, Modern Surface Analysis, Metallurgical Applications of AES and XPS, TMS-AIME, 1979, p. 13.

33. L. E. Davis, N. C. MacDonald, P. W. Palmberg, G. E. Riach and R. E. Weber, Handbook of Auger Electron Spectroscopy, Physical Electronics Industries, Eden Prairie, 1976.

APPENDIX A

PROCEDURES FOR PREPARATION OF Ti-6211 ALLOY SPECIMENS FOR EXAMINATION BY OPTICAL MICROSCOPY

by

W. C. Coons, Consultant
San Jose, CA

PROCEDURES FOR PREPARATION OF Ti-6211 ALLOY SPECIMENS FOR EXAMINATION BY OPTICAL MICROSCOPY

Thermally cycled but untested "Gleeble" samples are first cut adjacent to the thermocouple attachment. A second cut is made about 6 mm (1/4 in.) away rendering a sample approximately 6 mm (1/4 in.) long by the diameter of the test specimen, 6.35 mm (1/4 in.). A surface transverse to the length of the test specimen at the location of the thermocouple is exposed in the face of a 2.54 cm (1-in.) diameter bakelite mount faced with "Klarmount" mounting media.

Thermally cycled and tested* samples are cut approximately 12.7 mm (1/2 in.) from the fracture on one of the two fracture pieces. These sections are mounted in 2.54 cm (1-in.) diameter "Klarmount"-faced bakelite mounts exposing a longitudinal surface on the mount face. The mounts are then ground almost to the longitudinal midsection of the test sample with one end of course revealing the fracture surface cross-section.

A sample approximately 6 mm (1/4 in.) long containing the mating fracture surface is cut from each tested sample and used for scanning electron microscope evaluation of the fractures.

All the bakelite-mounted samples are ground through 600-grit silicon carbide paper prior to polishing.

Abrasive polishing of the ground specimens is performed as follows:

1. Rough polishing consists of placing the samples in a cylindrical metal holder weighing about 300 g, and placing the weighted

---

*Hot ductility test Gleeble specimens, for example

sample on a nylon cloth containing 1-?m diamond paste. The weighted sample is held in place by a fixture containing holes which is placed in a secure position about 10 mm (3/8 in.) above the surface of the nylon-cloth-covered wheel which revolves at about 300-400 rpm.

2. Final polishing is accomplished by placing the diamond polished sample into a 40-g PVC weight and inserting the weighted sample into a LECO "Fini-Pol" automatic polisher onto a "Lecloth" or "Mirroclotn" containing a slurry of "C-RO" Metallographic Polishing Abrasive to which is added several ml of a solution of $NaOH$-$K_3Fe(CN)_6$-H_2O in the proportion of 2 g/35 g/200 ml, respectively. Polishing is continued until a bright, shiny surface is obtained free of all grit and rough polishing artifacts. After polishing, the sample is washed in water, then alcohol, then warm air dried.

3. Electropolishing is an alternative to abrasive polishing and is preferred. (However, it can not be used if the contour of a fracture cross-section is to be examined, as electropolishing rounds off the edges of the specimen.)

   Electropolishing is done in an electrolyte consisting of 10-15 ml H_2SO_4-200 ml methyl alcohol, 15 g of aluminum chloride and 5 g of zinc chloride.

   The sample size should not be more than an area 10 mm (3/8-in.) square and should be as-ground through 600-grit SiC.

   Polishing is conducted at 20-25 Vdc input for 1-1/2 min. Contact is made at the edge of the sample with its face positioned in a horizontal plane. Do not soak the surface after polishing, just rinse in alcohol and dry in warm air stream.

Etching of polished samples is performed as follows:

1. For low-magnification, bright-field examination, a polished sample is first immersed in a saturated solution of oxalic acid for 45 s to 1 min. This is a required step to remove the residue film left by the polishing slurry. The sample is then etched for 1-1/2 to 2 min in a solution of 5 ml fluoboric acid (48-50%), 2 ml HNO_3-50 ml H_2O and 50 ml methyl alcohol. For very high magnification work (1000 to 3000X), a shorter etching time may be best.

2. For polarized light examination (up to about 500X), an as-polished surface is etched for 2 s in a 1 vol % chromic acid aqueous solution at a voltage about 18 Vdc. The voltage required for any given sample is that which will produce a dark blue-violet anodized film on the surface. The surface of the polished sample must be in a vertical position so that the etching reaction is evenly distributed. Anodic contact with the sample is made by a wire inserted into a hole drilled in the side of the specimen mount.

In the following three pages, illustrations of application of these etching procedures are presented. The illustrations were exhibited at the 40th annual technical meeting of the International Metallographic Society, San Francisco, CA, July 21-22, 1981.

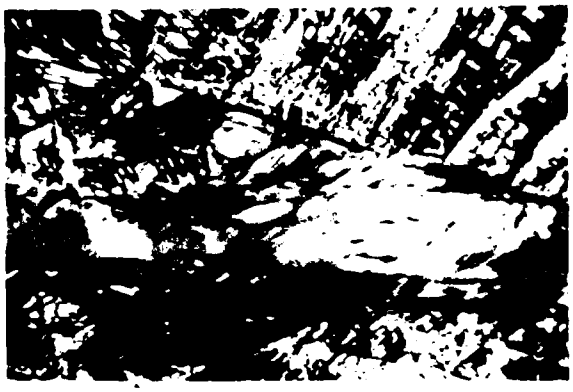

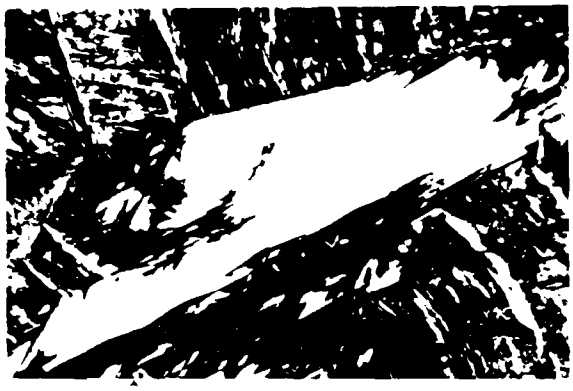

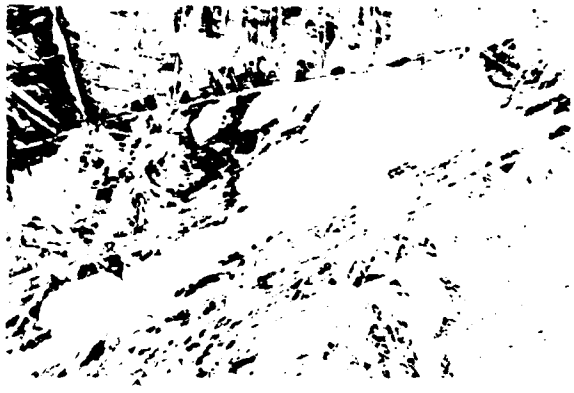

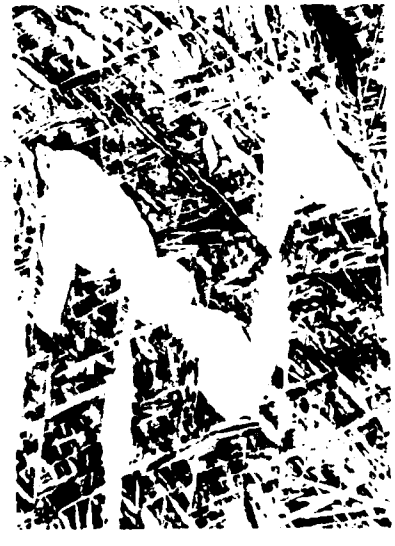

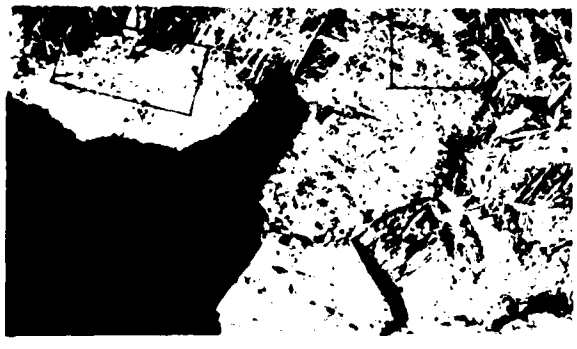








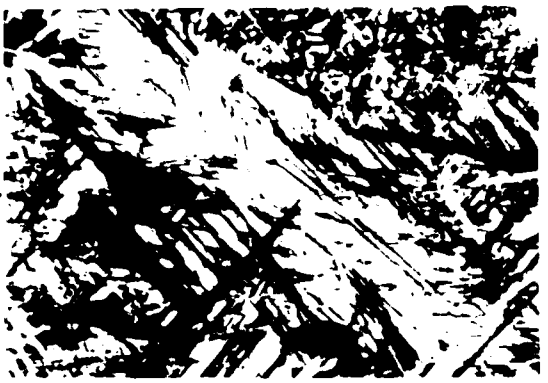

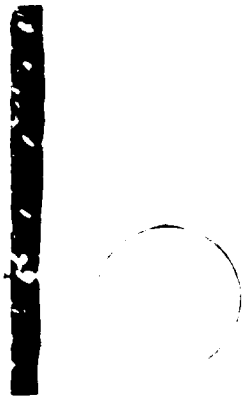

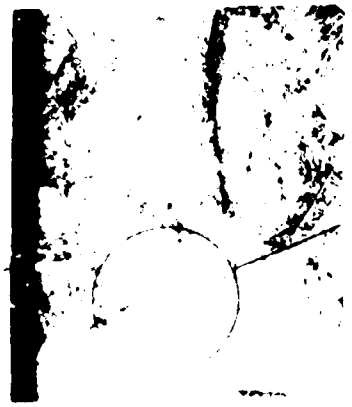

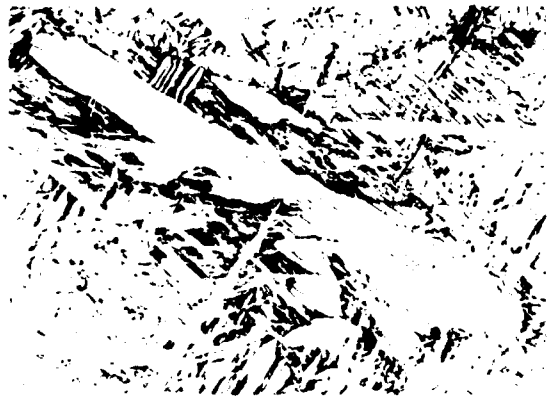

APPENDIX B

THE HOT DUCTILITY LOSS IN A TITANIUM ALLOY

(Paper published in Creep and Fracture of Engineering Materials and Structures, Proceedings of the Second International Conference, University College, Swansea, UK, April 1984, B. Wilshire and D. R. J. Owen, eds., Pineridge Press, Swansea, 1984, pp. 419 - 431).

THE HOT DUCTILITY LOSS IN A TITANIUM ALLOY

R. E. Lewis*, W. C. Coons+ and I. L. Caplan**

* Metallurgy and Composites Laboratory, Lockheed Palo Alto Research Laboratory, Palo Alto, California 94304, U.S.A.
+ Consultant, San Jose, California 95117, U.S.A.
** Ship Materials Engineering Department, David W. Taylor Naval Ship Research & Development Center, Bethesda , MD 21402 USA

SUMMARY

Fabrication methods for titanium alloy structures typically involve welding, hot forming, and other elevated temperature processing techniques. In evaluating new alloys, it is helpful to anticipate potential fabrication limitations. For the Ti-6Al-2Cb-1Ta-0.8 Mo (Ti-6211) alloy, a hot ductility test procedure was selected which permits useful modeling of the material's resistance to plastic deformation and fracture behavior during thermal excursions representative of welding, forming, and other elevated temperature fabrication procedures.

The hot ductility of Ti-6211 was examined on both heating and cooling, and results were compared with Ti-50 (commercially pure titanium), Ti-3Al-2.5V, Ti-6Al-4V, and Ti-6Al. Ti-50 exhibited a negligible hot ductility loss, Ti-3Al-2.5V a small hot ductility loss, Ti-6Al-4V and Ti-6Al a moderate hot ductility loss, and Ti-6211 a significant loss. When heated rapidly to about 1900K and tested in tension on cooling to about 1100K, the hot ductility of Ti-6211 is 0 to 15 pct. reduction in area, with fracture characterized by intergranular ductile rupture along prior beta grain boundaries. A number of factors are being studied that may contribute to or cause this hot ductility loss, namely, localized alloy partitioning at the beta→alpha interface on cooling below the beta-transus, irreversible segregation of impurity elements during thermal excursions above the beta-transus, and dynamic mechanical properties of the microstructural constituents present. Preliminary evidence has been obtained of sulfur segregation to prior beta grain boundaries as a result of thermal excursions high above the beta-transus but below the liquidus. This segregation is apparently irreversible, consistent with the observed irreversible nature of the hot ductility loss in Ti-6211.

1.0 EXPERIMENTAL PROCEDURE AND RESULTS

The hot ductility test technique selected for previewing hot cracking propensity in Ti-6211 was the high speed, programmable thermal cycling and loading method developed by Nippes et al. [1-3] In this technique, a 6.4 mm diameter by 108 mm long specimen is resistance heated over a 16 mm gage length according to a preselected thermal cycle. The test apparatus has the capability of pulling the specimen in tension during any part of the thermal cycle. The load required to break the specimen is measured as well as the reduction in area of the specimen.

The first topic investigated was propensity for weld cracking. Hot ductility tests were conducted on heating and on cooling during a simulated weld heat affected zone thermal cycle having a peak temperature of about 1900K. The thermal cycle used represents a position in the near heat-affected zone about 250 μm from the fusion line of a weld having an energy input of 940 kJm^{-1}. The thermal cycle used is similar to the 1755 K peak temperature cycle shown in Figure 1. Typically, the hot ductility is determined by applying a tensile load rapidly during

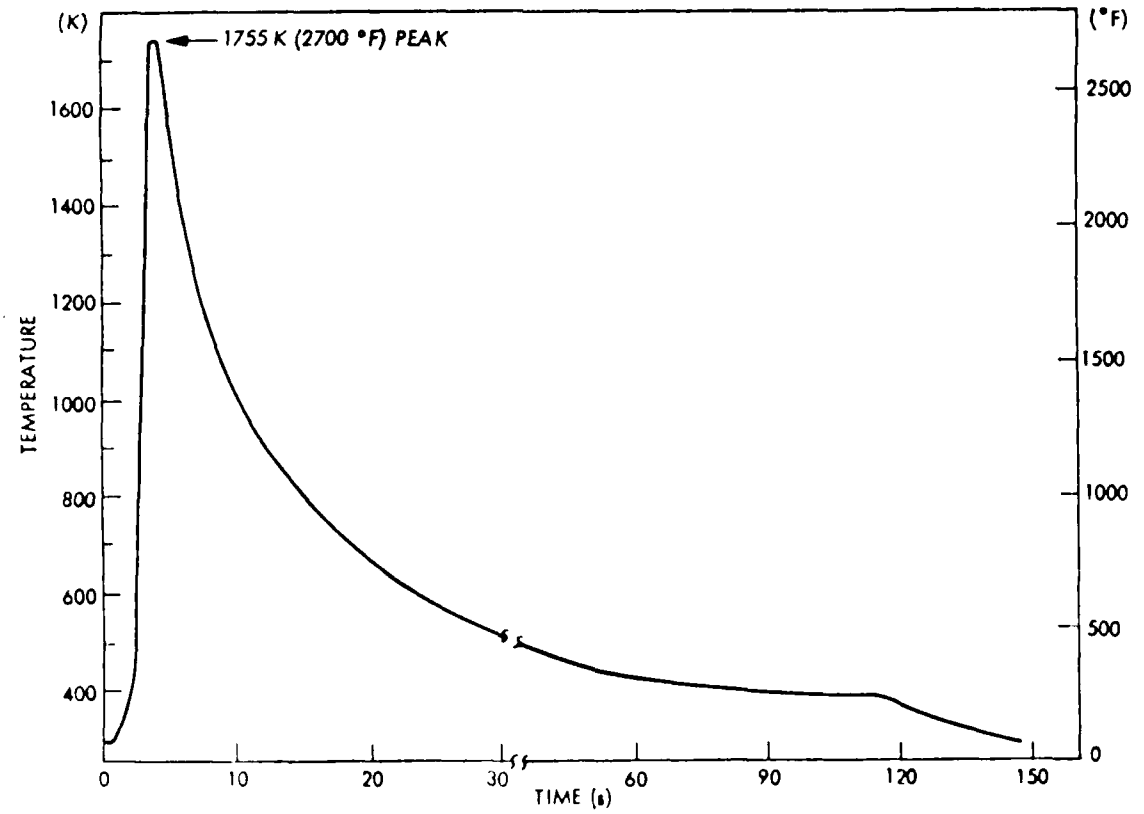

Figure 1. Typical Weld Thermal Cycle in Titanium Plate.

heating or cooling over a wide enough temperature range to identify minimum ductility regions. For Ti-6211 plate, the hot ductility on heating and on cooling in the first thermal cycle is shown in summary form in Figure 2. Note the loss in ductility down to 0 to 15 percent reduction in area when tested on cooling to about 1110K. In addition, the on-cooling hot ductility of Ti-50, Ti-3Al-2.5V, Ti-6Al-4V, and Ti-6Al alloys was determined using test conditions comparable to Ti-6211, and these results also appear in Figure 2. The only significant loss in hot ductility was observed in the alloys containing 6 wt % aluminum.

Observation of the hot ductility loss in Ti-6211 led to initiation of a study to determine factors associated with the hot ductility "dip" and to provide a basis for suppressing or avoiding it. It is assumed that the ductility loss indicates a propensity for hot cracking that may occur in welding, hot forming, rolling, and other related processes.

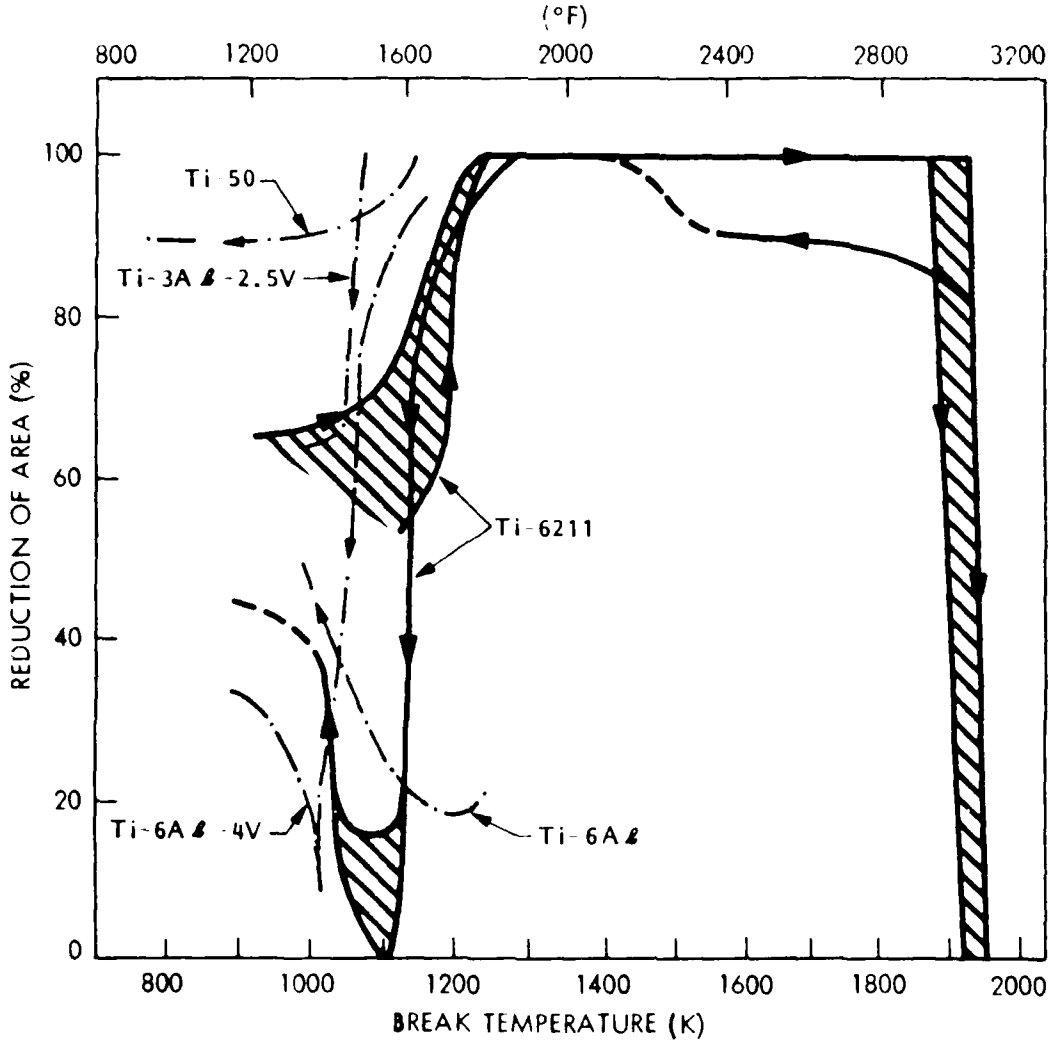

Figure 2. Illustration of Hot Ductility Exhibited by Ti-6211 Plate, Tested on Heating and on Cooling in the First Thermal Cycle

A number of specimens prepared from Ti-6211 plate and welds were thermally cycled, then examined by various techniques. The plate material was found to exhibit good hot ductility when tested on heating in the first thermal cycle, but exhibited poor hot ductility when tested on heating at 1100 K in a second thermal cycle. Welds, however, were found to exhibit low hot ductility when tested at the same temperature on heating in the first thermal cycle. Thus, the first thermal cycle, either simulated weld thermal cycle or an actual weld cycle, causes an irreversible loss in hot ductility in Ti-6211 at about 1100K.

Plate and weld specimens, thermally cycled and tested on cooling at about 1100K were examined by optical and scanning electron microscopy. Both materials fractured along prior beta grain boundaries as shown in Figures 3 and 4. This fracture mode was also exhibited by base metal when tested on heating in a second thermal cycle. (See Figure 5.) The typical fracture surface appearance of the low hot ductility specimens is illustrated in Figures 6 and 7. Note the predominance of microvoids on the fracture surface indicating the fracture mode is intergranular ductile rupture. This sequence is shown even more clearly by optical microscopy of sections close to the primary fracture surface. (See Figure 8.) The locus of microvoid nucleation is clearly the interface between the grain boundary alpha and the matrix. At the temperature of test, the matrix was probably beta, but at room temperature it is predominantly fine martensite with some large lenticular patches of martensite. Some microvoids nucleated within the prior beta grains as shown in Figures 9 and 10. In this case, microvoids preferentially nucleated at the boundary of the course lenticular martensite, possibly when the matrix was predominantly beta at the test temperature.

High-resolution scanning electron microscopy and transmission electron microscopy failed to reveal any particles or features which clearly provided nucleation sites for microvoid formation. Consequently, Auger electron microscopy was performed on specimens thermally cycled in the manner described above, but then tested in situ at RT and at 77K. Except for sulfur, the composition of the fracture surface was in close agreement with the typical ingot composition. Bulk concentration of sulfur in the ingot was below the detection level of 0.0015 at%. On the fracture surface, however, a sulfur concentration of 0.47at% was found, over 300 times the bulk concentration.

2.0 DISCUSSION

The preliminary evidence of sulfur concentration on the fracture surface of specimens failing by intergranular ductile rupture is significant. Sulfur has been identified as an embrittling species in many alloy steels and other metals, but has not been previously identified as a problem in commercial purity titanium alloys. Thermal cycles promoting sulfur embrittlement at grain boundaries in steel involve heating to above 1366K

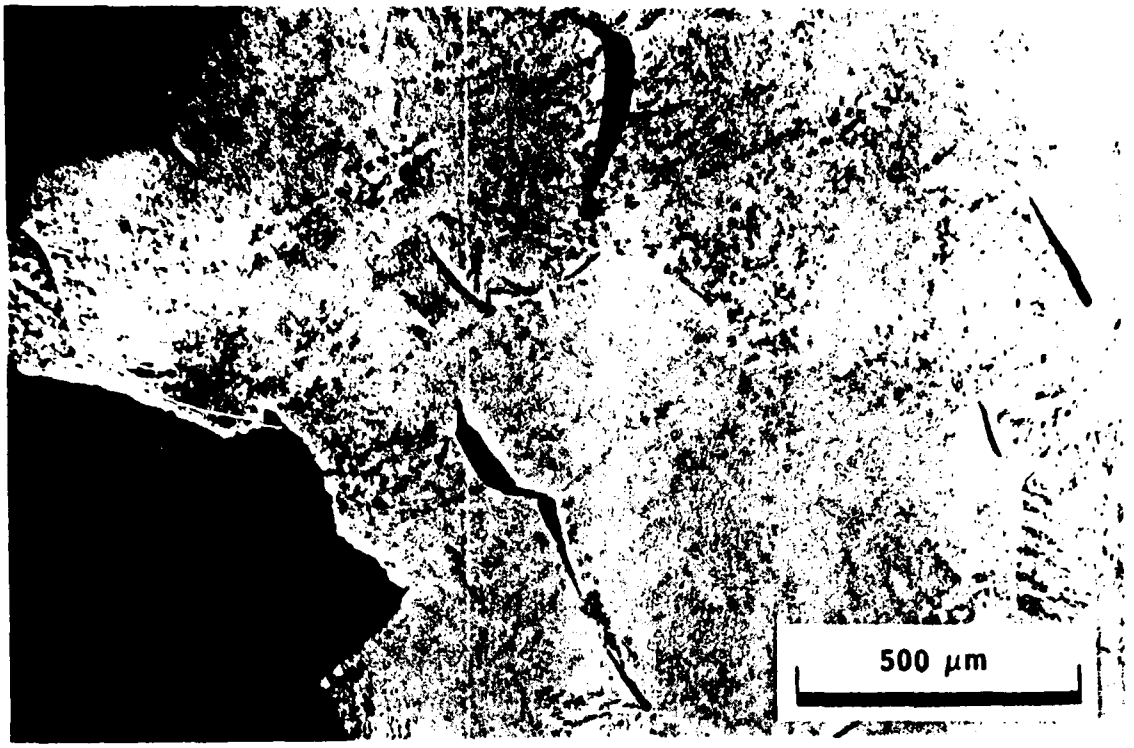

Figure 3. Section Through Fracture Surface in Ti-6211 Plate Specimen. Thermally Cycled, RT-1900K, Break on Cooling at 1091K. Reduction in Area = 9.5%.

Figure 4. Section Through Fracture Surface in Ti-6211 Weld Specimen. Thermally Cycled, RT-1800K, Break on Cooling at 1116K. Reduction in Area = 21%.

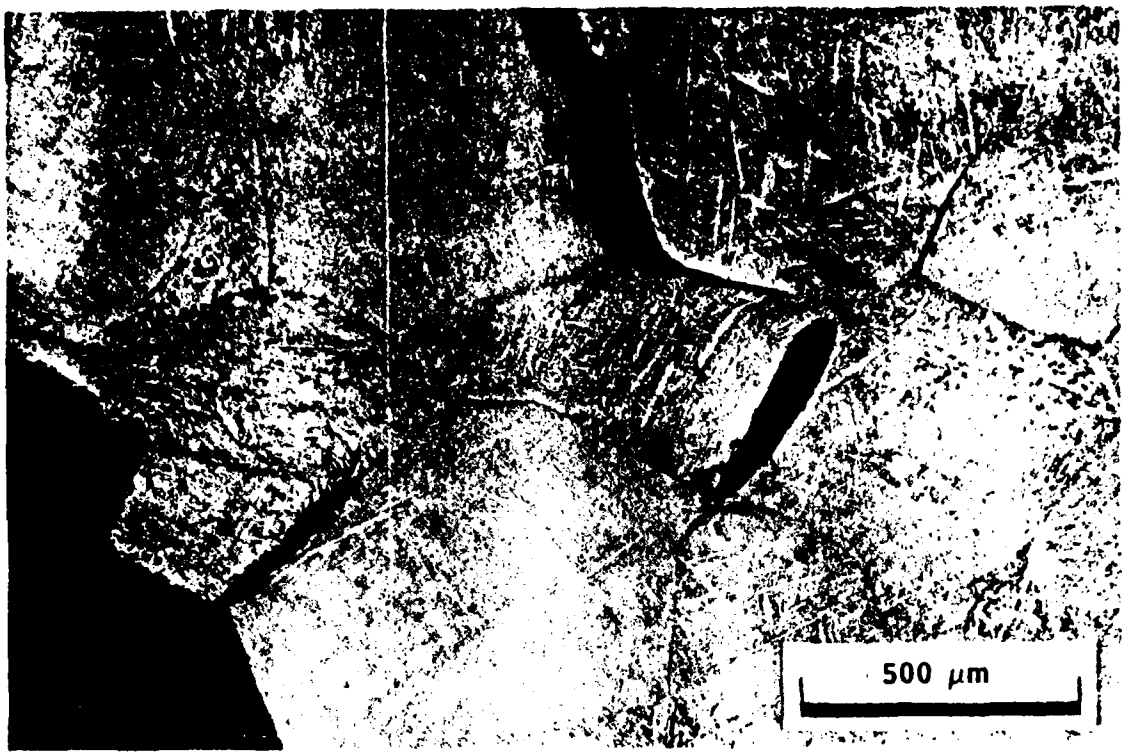

Figure 5. Section Through Fracture Surface in Ti-6211 Plate Specimen. Thermally Cycled, RT-1815K-RT, Break on Heating at 1089K. Reduction in Area = 9.2%.

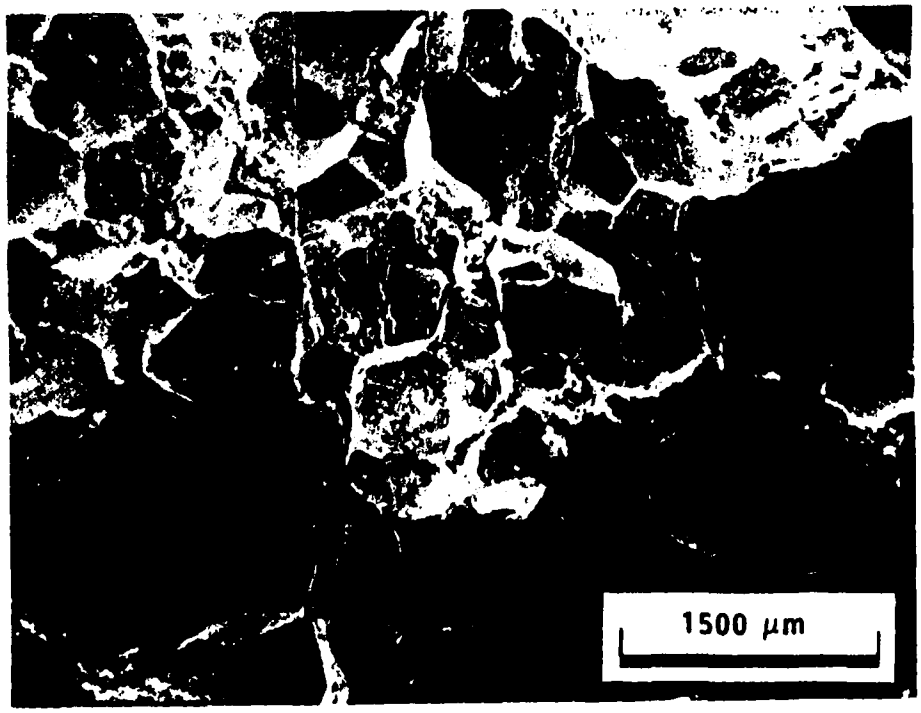

Figure 6. Fracture Surface Appearance of Ti-6211 Plate Specimen. Thermally Cycled, RT-1886K-RT, Break on Heating at 1094K. Reduction in Area = 12%.

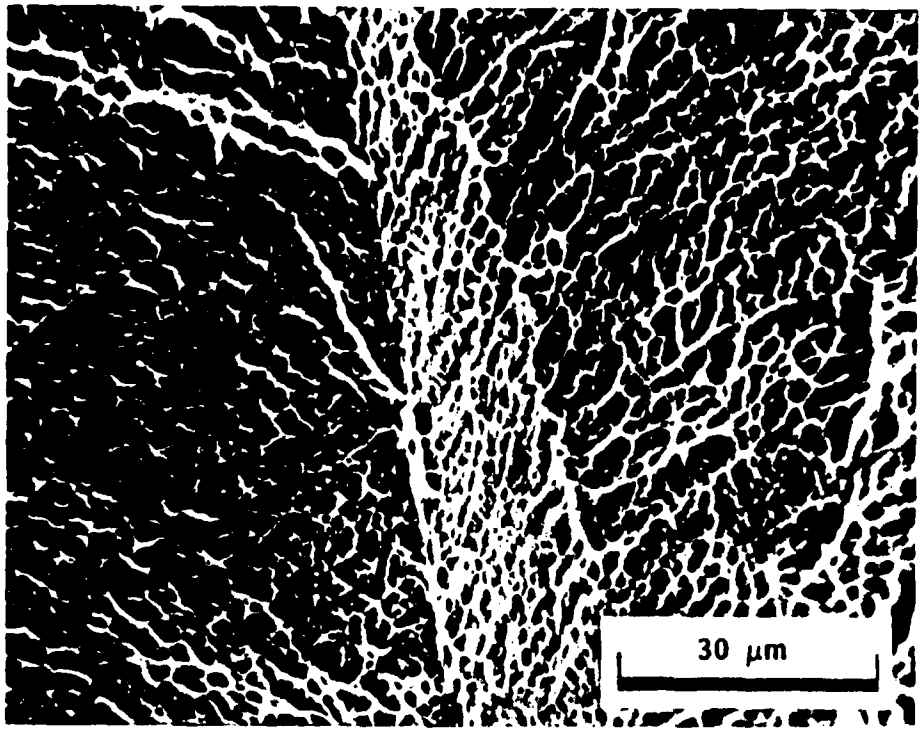

Figure 7. Higher Magnification of Fracture Surface Shown in Figure 6.

Figure 8. Microstructure Near Fracture Surface of Ti-6211 Plate Specimen Thermally Cycled, RT-1922K, Break on Cooling at 1094K. Reduction in Area was 10%. Note nucleation of microvoids along edge of grain-boundary alpha.

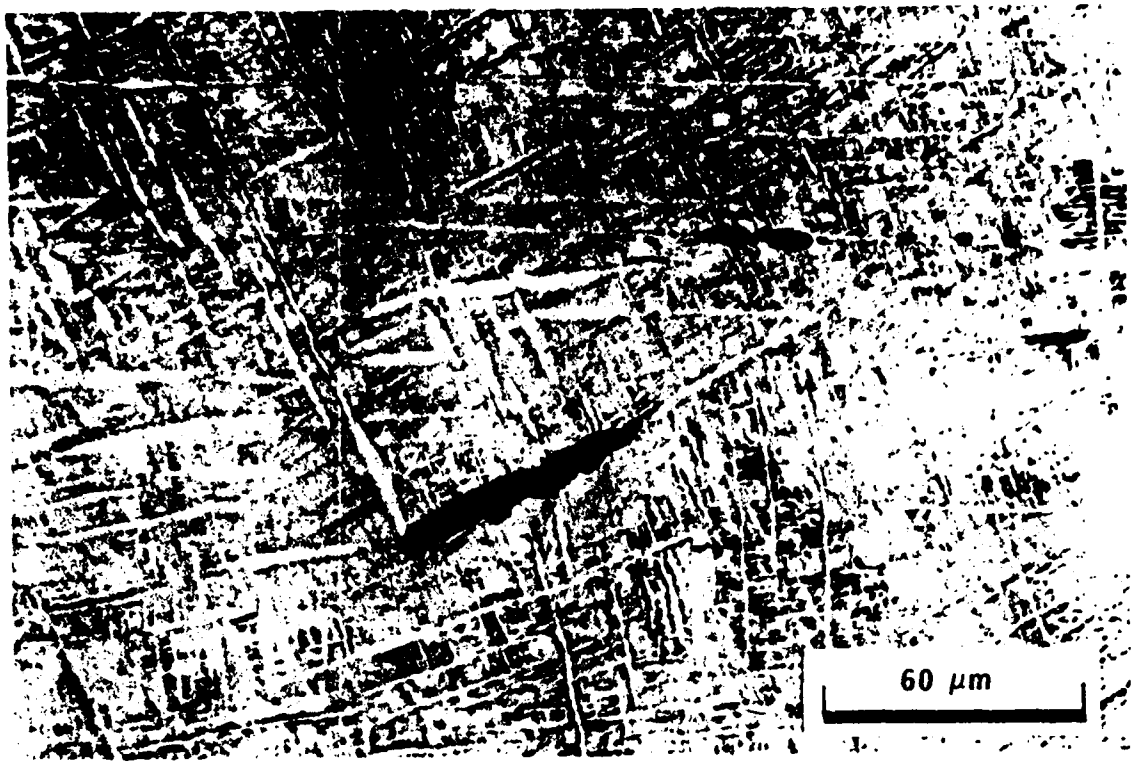

Figure 9. Microstructure Near Fracture Surface of Ti-6211 Plate Specimen Thermally Cycled, RT-1886K-RT, and Broken on Heating at 1094K. Reduction in Area was 12%.

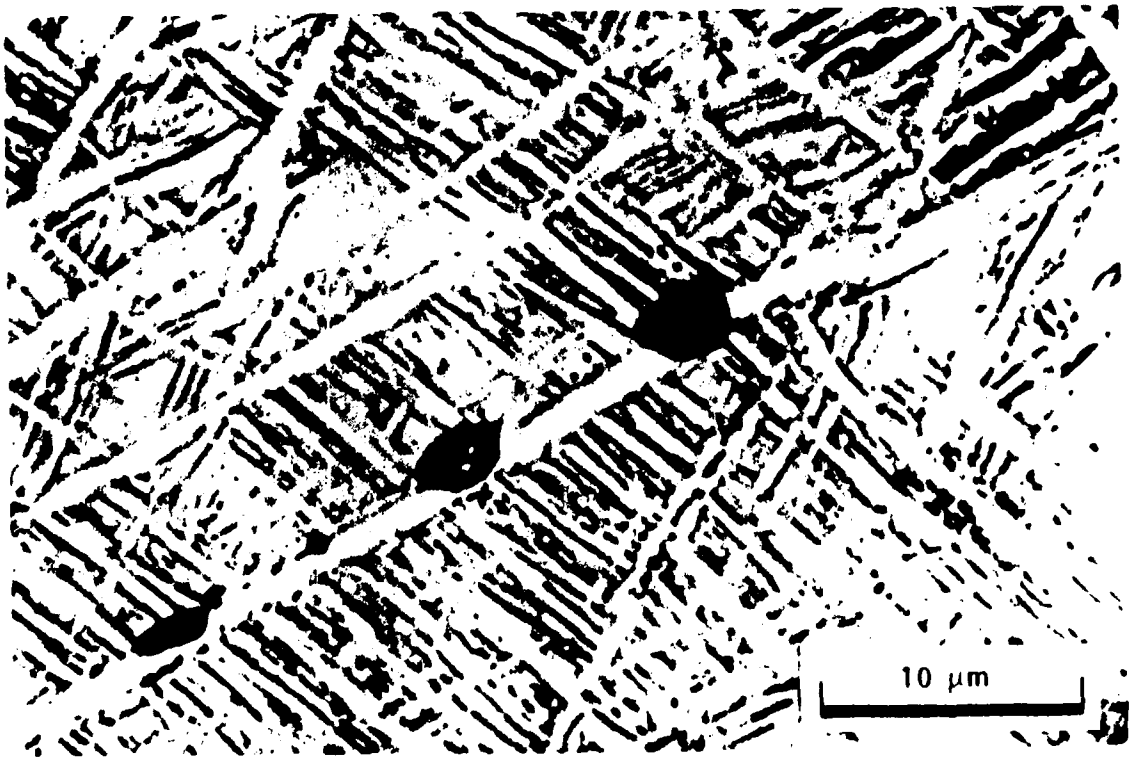

Figure 10. Higher Magnification of Region Shown in Figure 9.

which promotes the diffusion of sulfur to the austenite grain boundaries. The two ways to avoid this problem in steel have been (1) to reduce sulfur content to very low levels, or (2) to conduct thermal-mechanical treatments at temperatures below that required for grain boundary segregation of sulfur, so that the grain boundaries in the final product are not enriched in sulfur. The first technique applicable to steels is probably not viable for titanium alloys, and the second technique is not practical for almost all fabrication requirements.

These results suggest that when welding Ti-6211, some portion of the weldment will incur such grain boundary enrichment. Consequently, some sensitization of grain boundaries in the weld heat-affected zone may be expected. Similarly, when other fabrication processes are employed, such as drawing, bending, or spinning at elevated temperatures, embrittlement of grain boundaries may occur during the preheating cycle. The specific conditions of thermal history required to cause such embrittlement probably depend primarily on the combination of temperature and time above the beta-transus and secondarily on the cooling rate below the beta-transus. Some investigators have observed irreversible segregation of sulfur in metals resulting from elevated temperature thermal cycling. Joshi observed surface segregation of sulfur in 304 stainless steel [4], and his findings are shown schematically in Figure 11. Rath observed similar results in titanium [5]. The irreversible segregation sequence is consistent with the observed irreversible loss in hot ductility of Ti-6211, and is illustrated by the low hot ductility at 1100 K when tested on heating in a second simulated weld thermal cycle.

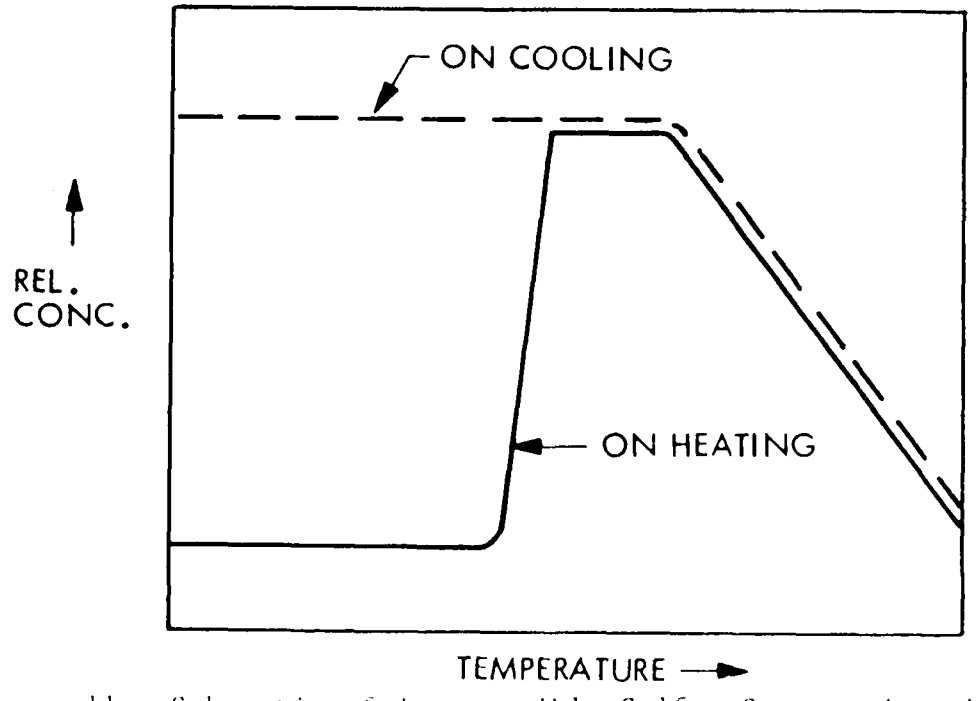

Figure 11. Schematic of Irreversible Sulfur Segregation Observed in 304 Stainless Steel by Joshi (4) and in Titanium by Rath (5).

Another factor involved in the grain boundary fracture mode associated with the observed loss in hot ductility is the elevated temperature strength of the grain boundary alpha and matrix (beta or predominantly beta with some alpha present). Tensile strength changes rapidly when tested on cooling over the temperature range of interest. This is illustrated in Figure 12 by the rapidly changing gross section strength at temperatures below 1280K, the beta-transus. The minimum net section strength occurs at about 1100K, which also corresponds to the minimum reduction in area exhibited in the hot ductility test. Analysis of the strength of the individual phases and their relation to the hot ductility is inhibited by the inadequate knowledge of the continuous cooling transformation diagram for the Ti-6211 alloy. Only one investigator [6] has reported any pertinent data for the continuous cooling transformations in this alloy,see Figure 13. In the on-going study of phase transformations by the authors, it has recently been established that this diagram is probably incomplete.

The literature available on sulfur in titanium is sparse and controversial. According to Hansen [7], a subsulfide with unknown structure and approximate conposition Ti_2S has been identified. The lowest concentration at which sulfur appears as an insoluble compound, Ti_2S, is 0.02 wt% detected in magnesium-reduced Ti-base alloys, hot-rolled and annealed at 1060K. According to Berger et al. [8], the solubility of sulfur in alpha-titanium is between 0.009 and 0.017 wt% at 1173K. However, the same authors suggest that "...there are some indications from grain-size studies that sulfur is less soluble in beta than in alpha titanium...."

In addition, Elliott [9] reports the finding by Bartram of another solid solution phase having an approximate stochiometric ratio Ti_6S, but structure and solubility in alpha and beta titanium are unidentified.

According to the results of the present study, the solubility of sulfur in alpha and beta titanium is an important question. Since the hot ductility is high in Ti-6211 specimens thermally cycled first to 1900K, then tested on cooling down to 1250K (see Figure 2), it is possible that sulfur which has segregated to beta-grain boundaries is of inadequate concentration to cause embrittlement until alpha forms on cooling. The concentration of sulfur in the beta-grain boundaries may be increased on cooling below the beta-transus, as the grain-boundary alpha layer grows in thickness. Such increase would require the solubility of sulfur to be lower in alpha than in beta titanium, contrary to that postulated by Berger et al. [8]. The lower solubility of sulfur in alpha would cause a progressive enrichment of sulfur in beta at the alpha-beta interface during the growth of alpha into beta. But if the solubility of sulfur is higher in alpha than in beta titanium, as Berger et al. propose, then no significant enrichment of sulfur due to partitioning would be expected during the growth of the grain-boundary alpha on cooling below the beta-transus.

Additionally, the observed on-cooling tensile ductility increase below 1030K is probably related to the progressive increase in strength of the grain-boundary alpha region so that fracture is preceded by significant plastic strain throughout the grains. This is in contrast to the localized plastic flow along the prior beta-grain boundaries when tensile stress is applied at a temperature where low hot ductility is exhibited.

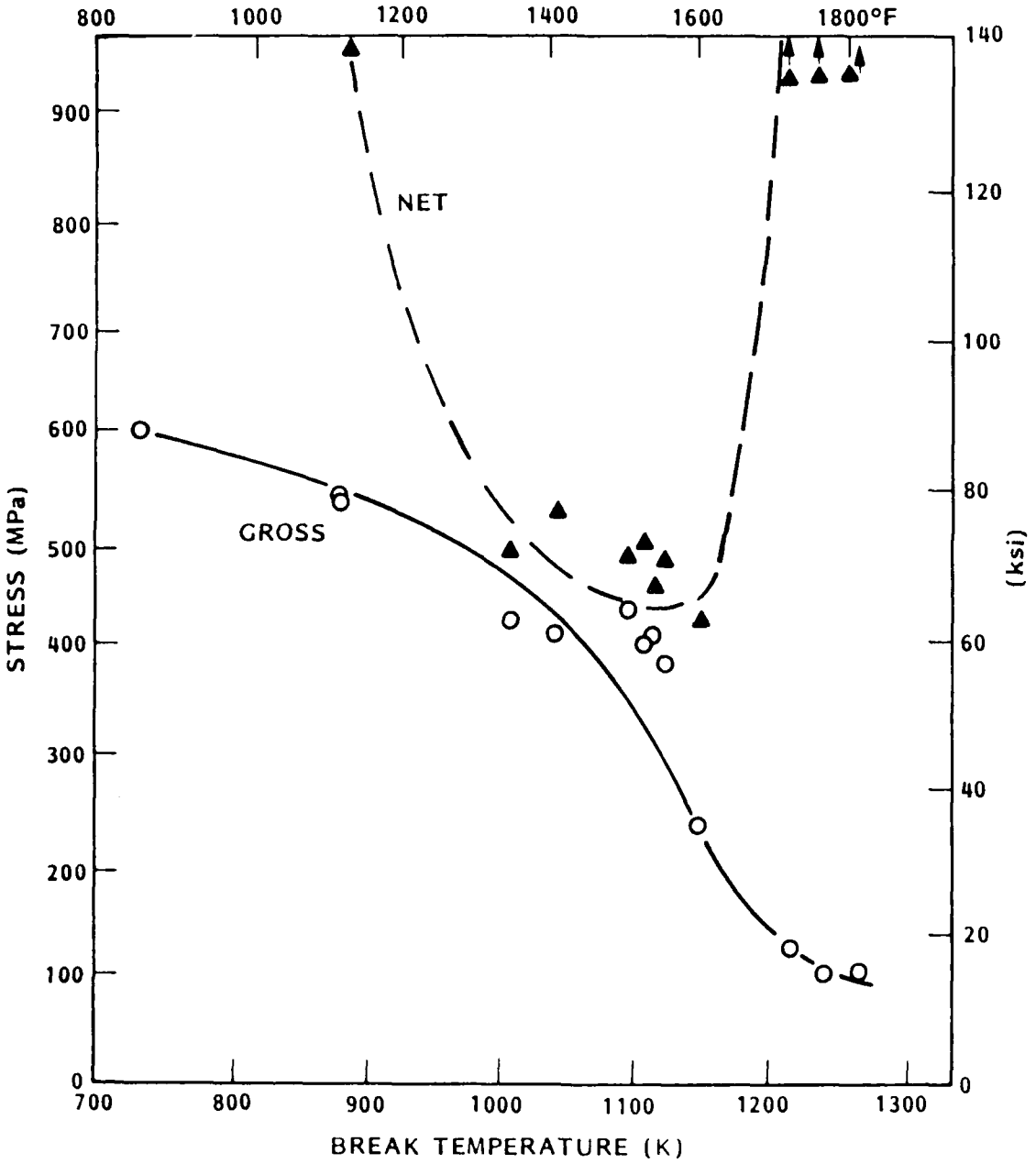

Figure 12. Effect of Break Temperature on Net and Gross Section Stress in Ti-6211 Plate Specimens Thermally Cycled From RT to About 1866K and Broken on Cooling at Indicated Temperature.

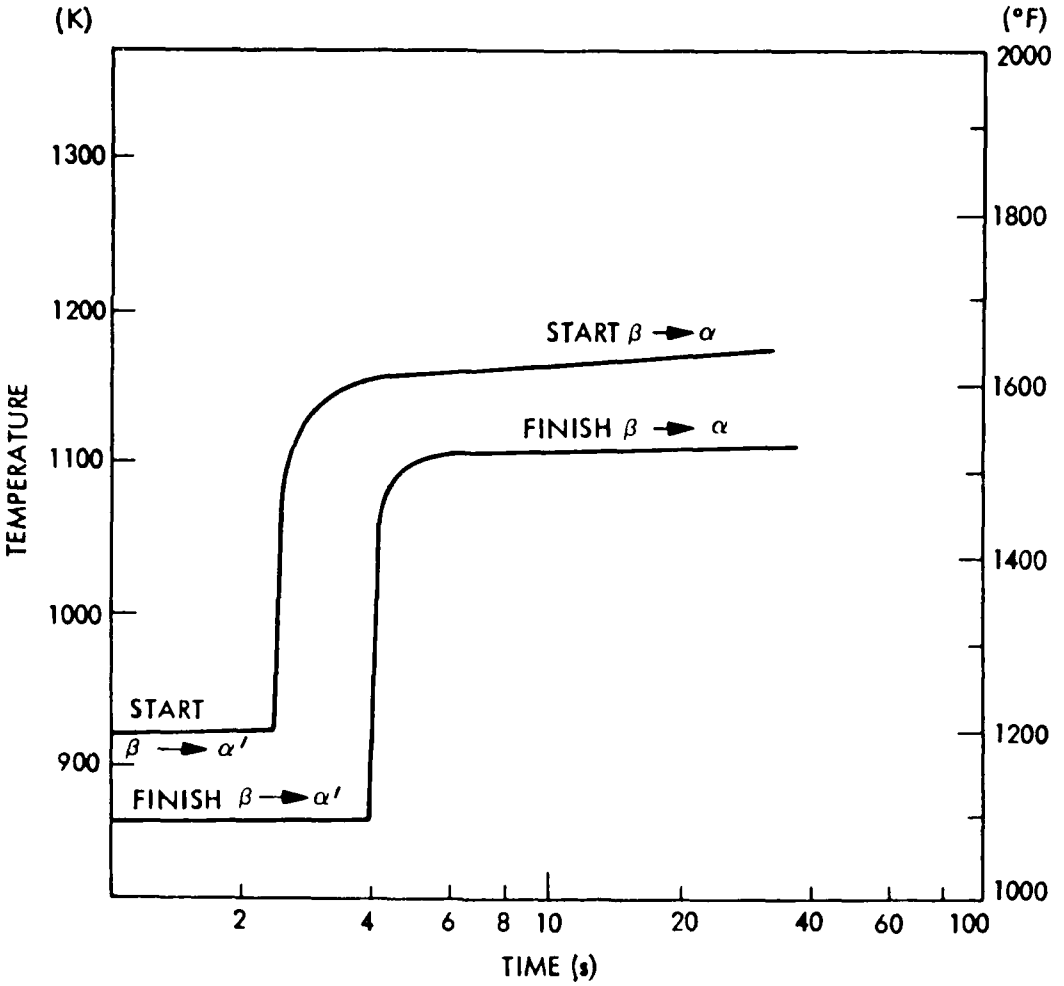

Figure 13. Continuous Cooling Diagram for Ti-6211 (After Gourdine [6]).

CONCLUSIONS

1. Simulated weld thermal cycles for the near-heat-affected zone result in a significant loss in hot ductility in titanium alloys containing 6 wt% aluminum. A necessary requirement for such a ductility dip is a previous thermal excursion well above the beta-transus, particularly to between 1470 to 1920K.

2. The fracture observed in Ti-6211 in the hot ductility dip region, 1030 to 1120K , is microvoid nucleation and coalescence preferentially along the prior beta-grain boundaries, causing intergranular fracture. This fracture mode produces a low tensile ductility as measured by reduction in area, when tested either on heating or cooling to about 1100K,, provided the necessary prior thermal excursion has occurred.

3. The fracture surface of a Ti-6211 specimen, thermally cycled to a peak temperature of about 1900K, contains a significant concentration of sulfur, over 300 times higher than the bulk

ACKNOWLEDGEMENTS

The authors wish to thank Mr. J. L. Cavallaro, David W. Taylor Naval Ship Research and Development Center, Bethesda, MD, U.S.A., and Dr. B. A. MacDonald, Office of Naval Research, Washington, D.C. for their interest in and support of the subject study. This work was supported by the U.S. Office of Naval Research under Contract N00014-79-C-0449.

REFERENCES

1. NIPPES, E. F. and SAVAGE, W. F., Welding J. (Res. Supp.), November 1949, 28, 534s.

2. NIPPES, E. F., MERRILL, L. L. and SAVAGE, W. F., Welding J. (Res. Supp.), November 1949, 28, 556s.

3. NIPPES, E. F., SAVAGE, W. F., MASON, H. F., BASTIEN, B.J., and CURRAN, R., Welding J. (Res. Supp.), April 1955, 34, 183s.

4. Private Communication, Dr. A. Joshi, Lockheed Palo Alto Research Laboratory, Palo Alto, CA, U.S.A.

5. Private Communication, Dr. B. B. Rath, Metallurgy Division, U. S. Naval Research Laboratory, Washington, D.C., U.S.A.

6. Gourdine, J., Welding J. (Res. Supp.), March 1974, 53, 117s.

7. HANSEN, M., "Constitution of Binary Alloys", Second Edition McGraw-Hill, New York, 1958, 1167.

8. BERGER, L. W., WILLIAMS, D.N., and JAFFEE, R. I., Trans. ASM, 1957, 49, 300, discussion 312.

9. ELLIOTT, R. P., 'Constitution of Binary Alloys, First Supplement', McGraw-Hill, 1965, 795.

APPENDIX C

THE ELEVATED TEMPERATURE DUCTILITY DIP PHENOMENON IN ALPHA, NEAR-ALPHA, AND ALPHA-BETA TITANIUM ALLOYS

(Paper published in Titanium Science and Technology, Proceedings of the Fifth International Conference on Titanium, Munich, FRG, September 1984, G. Lutjering, U. Zwicker, W. Bunk, eds., Deutsche Gesellschaft fur Metallkunde, E. V., Oberursel, FRG, 1985, pp. 799 - 805).

THE ELEVATED TEMPERATURE DUCTILITY DIP PHENOMENON IN ALPHA, NEAR-ALPHA AND ALPHA-BETA TITANIUM ALLOYS

R. E. Lewis, Lockheed Palo Alto Research Laboratory, Palo Alto, CA., USA
I. L. Caplan, Research Metallurgist, Arnold, MD., USA
W. C. Coons, Consultant, San Jose, CA., USA

Background and Experimental Procedure

Many alpha, near-alpha and alpha-beta titanium alloys are sensitive to cracking when hot worked below the beta transus. The propensity for hot cracking in these alloys can be related to their ductility at these temperatures.

A high speed, programmable thermal cycling and loading method developed by Nippes, et al (1-3) was used in this study to measure hot ductility. In this technique, a 6.4 mm diameter by 108 mm long specimen is resistance heated over a 16 mm gage length according to a preselected thermal cycle. The test apparatus has the capability of pulling the specimen in tension during any part of the thermal cycle. The load required to break the specimen is measured as well as the reduction in area of the specimen.

Hot ductility tests were conducted on heating and on cooling during a simulated weld heat affected zone thermal cycle having a peak temperature of about 1900°K. The thermal cycle used represents a position in the near heat-affected zone about 250 m from the fusion line of a weld having an energy input of 945 kJm^{-1}. The thermal cycle used is similar to the 1755°K peak temperature cycle shown in Fig. 1. Typically, the hot

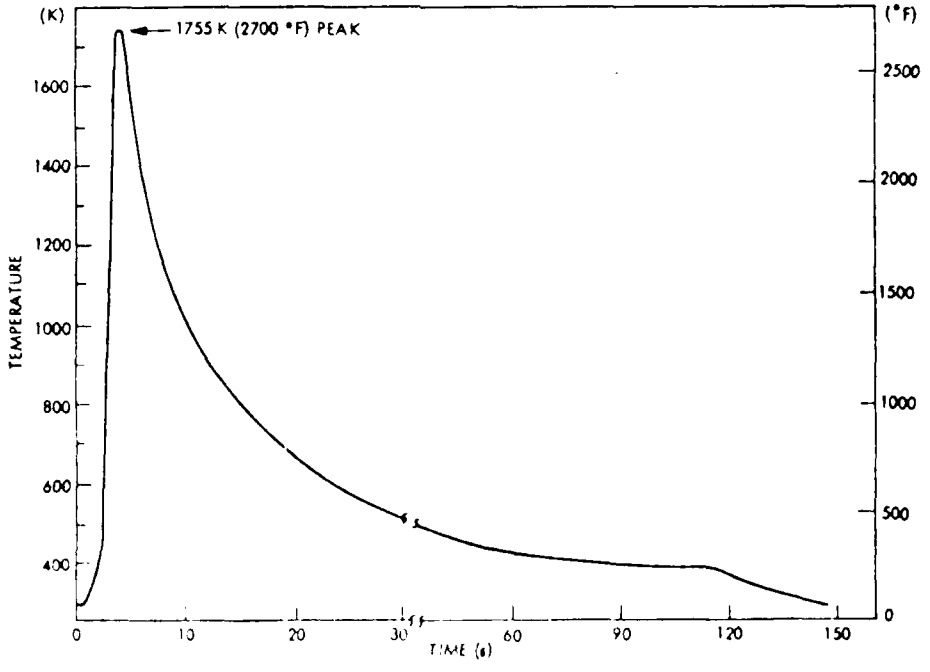

Fig. 1: Typical weld thermal cycle in titanium plate

ductility is determined by hydraulically applying a tensile load rapidly ($\dot{\epsilon}$ = 160/min.) during heating or cooling over a wide enough temperature range to identify minimum ductility regions.

Results and discussion

Discovery of the ductility Dip Phenomenon. Initial on-heating and on-cooling tests performed on the Ti-6Al-2Nb-1Ta-0.8Mo alloy (Ti-6211) revealed a significant hot ductility "dip" (HDD) in the material when tested on cooling in the temperature region of 1030 to 1120°K (4). This is shown in Fig. 2. The peak temperature in the simulated weld thermal cycle was 1870°K and the measured reduction in area of the fractured specimen was between 0 and 15 percent.* In contrast, when this alloy is heated directly from room temperature to the same temperature region and tested, the measured hot ductility is in excess of 50 percent reduction in area.

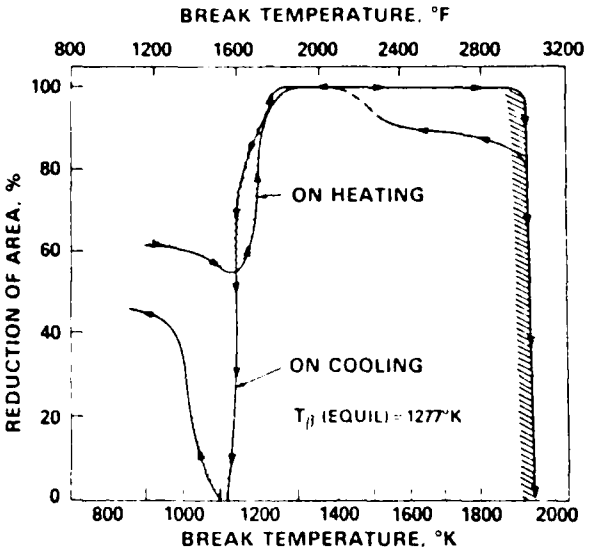

Fig. 2: On-heating and on-cooling hot ductility curves for Ti-6211 (beta processsed) plate

Fracture Mode. The fractured Ti-6211 specimens were examined by optical and scanning electron microscopy. Specimens that were broken on heating from room temperature displayed typical transgranular ductile rupture with substantial necking, see Fig. 3. By comparison, specimens fractured on cooling were markedly different as shown in Fig. 4a. The fracture mode of the latter is intergranular ductile rupture along prior beta grain boundaries. Note the predominance of microvcids on the surfaces of the prior beta grains seen at higher magnification as shown in Fig. 4b.

*The magnitude of the hot ductility is affected primarily by break temperature, with high ductility exhibited above the $\beta \rightarrow \alpha$ transformation temperature range, intermediate ductility within the transformation range, and low ductility within 100°K below the transformation range (5).

The locus of microvoid nucleation is clearly the interface between the grain boundary alpha and the matrix, see Fig. 5. At the temperature of test the matrix was predominantly beta, but at room temperature it is predominantly fine martensite with some large lenticular patches of martensite.

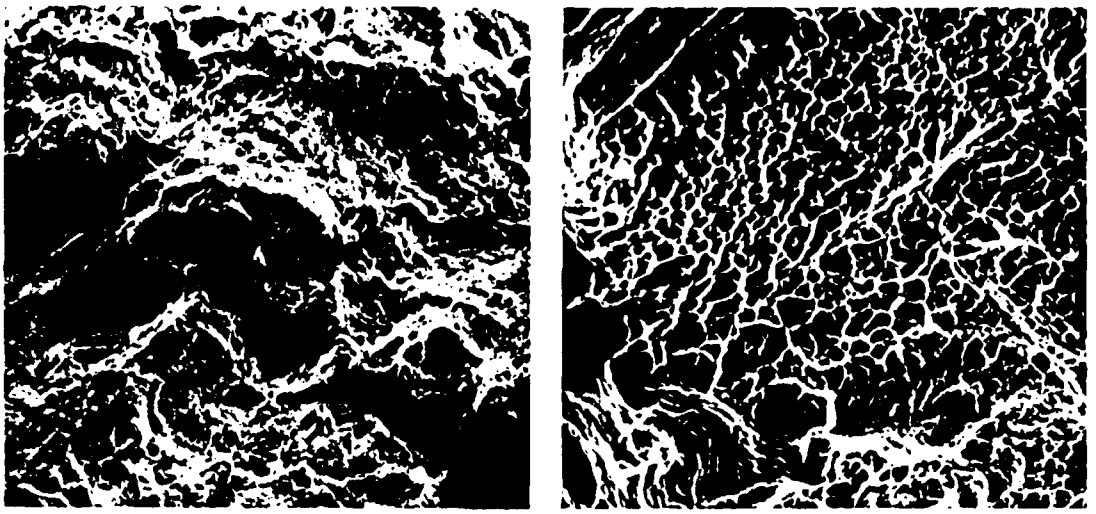

(a) (b)

Fig. 3: Fracture surface of Ti-6211 specimen broken on heating at 1110°K. Reduction in area = 59 percent

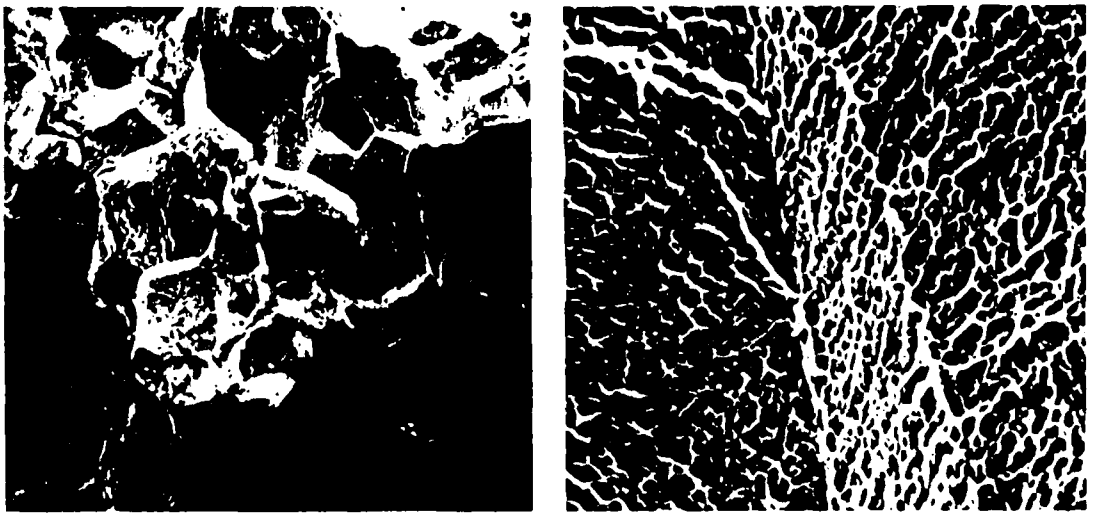

(a) (b)

Fig. 4: Fracture surface of Ti-6211 specimen thermally cycled, RT → 1886°K → broken on cooling at 1094°K. Reduction in area = 10 percent

During the application of the tensile load some microvoids are also nucleated within the prior beta grains as shown in Fig. 6. In this case, microvoids preferentially nucleated at the boundary of the course lenticular martensite when the matrix was predominantly beta at the test temperature.

Fig. 5: Microvoids nucleating along edge of grain boundary alpha

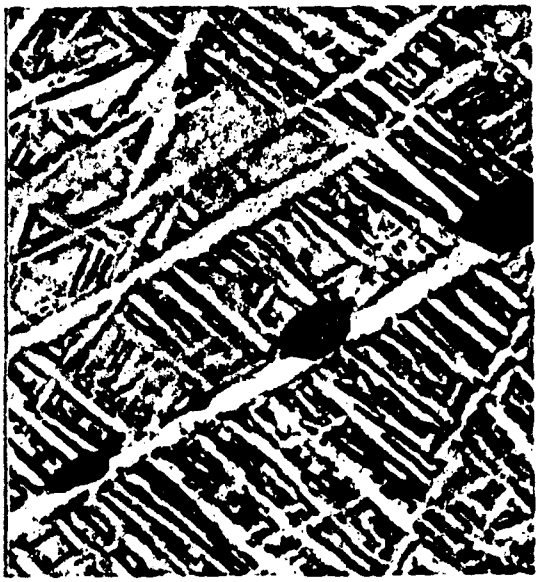

Fig. 6: Microvoids nucleating within prior beta grains at boundary of coarse lenticular martensite

High resolution scanning electron microscopy and transmission electron microscopy failed to reveal any particles or features which clearly provided nucleation sites for microvoid formation. Consequently, Auger electron microscopy was performed on specimens thermally cycled in the manner described above, but then tested in-situ at RT and at 77°K. Except for sulfur, the composition of the fracture surface was in close agreement with the typical ingot composition. The sulfur concentration measured was 0.47 atomic percent, over 300 times the bulk concentration (4). (Bulk concentration of sulfur in the ingot was below the detection level of 0.0015 atomic percent.)

Prior Material Condition. Hot ductility tests were performed on Ti-6211 material in different product forms and conditions.

Alpha-beta processed Ti-6211 plate was hot ductility tested on cooling from approximately 1900°K in a similar manner to the previous tests on beta processed material. The initial plate microstructures are shown in Fig. 7. The initial microstructure had no effect on the on-cooling hot ductility test results. The alpha-beta plate displayed a similar HDD to the beta processed material. The fracture appearance was similar to that shown in Fig. 4.

Cast Ti-6211 was evaluated by means of the hot ductility test apparatus. The cast material also was found to exhibit an on-cooling HDD with a very sharp drop at 1125°K; reduction in area was 8 percent. Above or below this temperature, the hot ductility rose considerably (>36 percent reduction in area). The fracture appearance of cast Ti-6211 tested in the HDD test region was intergranular ductile rupture, typical of the previously described low ductility fractures.

The hot ductility of Ti-6211 weld metal was obtained by testing both on heating and on cooling. As expected, the on-cooling behavior was similar to Ti-6211 plate: the minimum reduction in area was 15 percent at 1100°K. Interestingly, the hot ductility of the weld metal when tested on heating at 1100°K also displayed a substantial drop in ductility to 15 percent reduction in area similar to the on cooling behavior. This was not observed in the on-heating hot ductility tests of plate material.

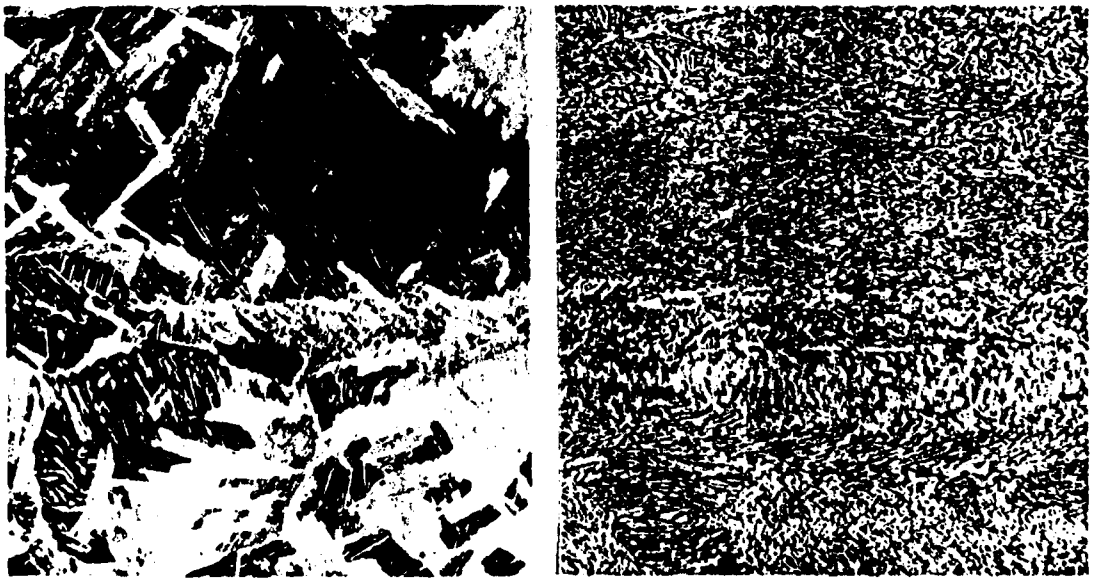

(a) Beta processed plate (b) Alpha-beta processed plate

Fig. 7: Initial microstructures of Ti-6211 plate materials

Tests were conducted to simulate the weld metal thermal history by heating plate material close to the melting point and followed by rapid cooling. This was accomplished by exposing the material in the hot ductility testing apparatus to a simulated weld thermal with a peak temperature of 1900°K. When these specimens were subsequently tested on heating from room temperature, the hot ductility test results were similar to the on-heating test results of weld metal. A substantial reduction in hot ductility was exhibited (9 percent minimum reduction in area) and the fracture appearance resembled that shown in Fig. 4.

Effect Of Alloy Composition. A number of alloys differing in composition were tested on cooling and compared to Ti-6211.

The effect of aluminum content is evident in the test results presented in Fig. 8. The loss in hot ductility appears to be related to the aluminum concentration. The greatest drop in ductility was observed in the alloys containing 6 weight percent aluminum, with the Ti-6211 alloy exhibiting the highest loss.

The effect of oxygen content on hot ductility was evaluated by examining the on-cooling hot ductility of two grades of Ti-6Al-4V plate containing 0.08 and 0.12 weight percent oxygen. These results are shown in Fig. 9. The lower oxygen Ti-6Al-4V plate material exhibited a greater dip in hot ductility than the material containing higher oxygen. The minimum hot ductilities obtained for the plates containing 0.08 and 0.12 weight percent oxygen were 8 and 31 percent reduction in area, respectively. It is important to note that the Ti-6211 plate, which exhibits the most severe ductility dip, has very low oxygen (0.07 weight percent).

Finally, the effect of yttria (Y_2O_3) on the hot ductility behavior of Ti-6211 was examined. Yttria is added to certain titanium alloys in order to improve their hot workability (6). Ti-6211 plate containing 150 ppm Y_2O_3 and 0.09 weight percent oxygen was tested in the thermal cycling apparatus. The on-cooling HDD behavior of this material is compared to the standard Ti-6211 plate in Fig. 10. The hot ductility of the yttria-containing material in the ductility dip region was 28 percent, substantially higher than that of the standard Ti-6211 plate.

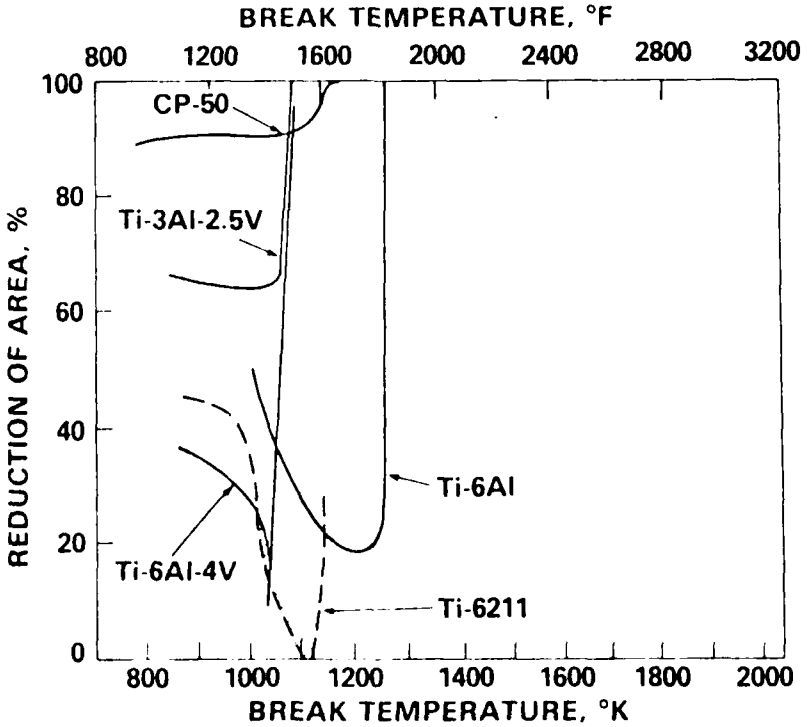

Fig. 8: The on-cooling hot ductility behavior of titanium alloys with varying aluminum content

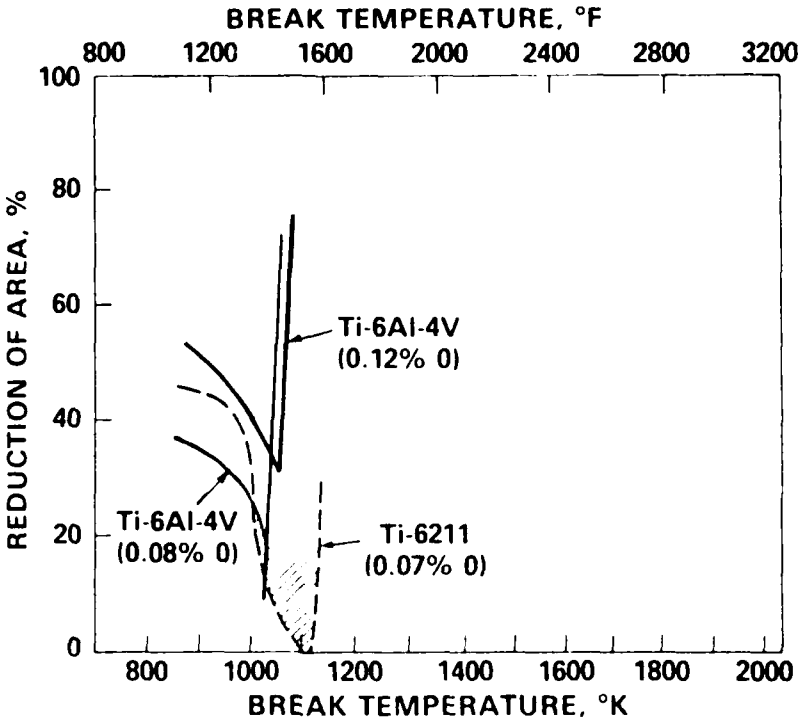

Fig. 9: The effect of oxygen on hot ductility

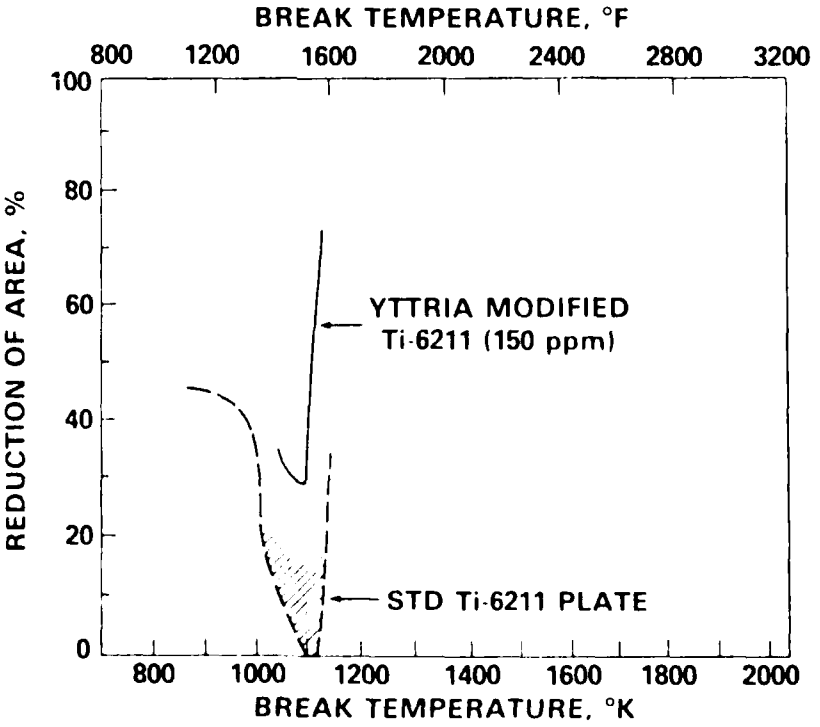

Fig. 10: The effect of yttria on hot ductility

Conclusions

o Elevated temperature thermal cycles imposed on titanium alloys containing 6 weight percent aluminum result in a significant loss in hot ductility when tested in the region of 1030 to 1120°K. A necessary condition for this ductility dip is a peak temperature well above the beta transus (1500°K).

o The HDD phenomenon does not appear to occur with alloys containing substantially lower levels of aluminum, viz, Ti-3Al-2.5V or CP titanium.

o The fracture mode observed in the hot ductility dip region is microvoid nucleation and coalescence preferentially along prior beta-grain boundaries causing intergranular fracture. This fracture mode produces a low tensile ductility, as measured by reduction in area, when tested either on heating or cooling to about 1100°K.

o The severity of the ductility dip may be reduced by adding yttria to certain titanium alloys. A slight increase in oxygen may also prove to be beneficial to the hot ductility of titanium alloys containing 6 weight percent aluminum.

References

(1) E. F. Nippes, and W. F. Savage: Welding Journal (Res. Supp.) 28 (1949) 534s.
(2) E. F. Nippes, L. L. Merrill, and W. F. Savage: Welding Journal (Res. Supp.) 28 (1949) 556s.
(3) E. F. Nippes, W. F. Savage, H. F. Mason, B. J. Bastien, and R. Curran: Welding Journal (Res. Supp.) 34 (1955) 183s.
(4) R. E. Lewis, W. C. Coons, and I. L. Caplan: "Proceedings of the Second International Conference on Creep Fracture of Engineering Materials and Structures", Pineridge Press Ltd., Swansea (1984) 419.
(5) R. E. Lewis, I. L. Caplan and W. C. Coons, "Proceedings of the Second International Conference on Creep and Fracture of Engineering Materials and Structures", Pineridge Press Ltd., Swansea (1984) 433.
(6) H. B. Bomberger, S. R. Seagle: U.S. Patent No. 3,697, 403 (1972).

APPENDIX D

CONTINUOUS COOLING TRANSFORMATIONS IN Ti-6Al-2Cb-1Ta-0.8Mo

(Paper published in Solid → Solid Phase Transformations, Proceedings of an International Conference, Carnegie-Mellon University, Pittsburg, USA, August 1981, H. I. Aaronson, D. E. Laughlin, R. F. Sekerka and C. M. Wayman, eds., The Metallurgical Society of AIME, Warrendale, USA, 1982, pp. 1499 - 1503).

CONTINUOUS COOLING TRANSFORMATIONS IN Ti-6Al-2Cb-1Ta-0.8Mo

R. E. Lewis*, W. C. Coons**, J. C. Williams*** and G. K. Scarr***

*Lockheed Missiles & Space Co., Inc., Palo Alto, California 94304
**Consultant, San Jose, California 95117
***Mellon Institute, Carnegie-Mellon University, Pittsburgh, PA 15213

Rapid thermal cycling of the titanium alloy Ti-6wt%Al-2wt%Cb-1wt%Ta-0.8wt%Mo between room temperature and about 1900K produced a microstructure with both large lenticular plates and irregular patches of hexagonal transformation product within the prior β grains. The irregular patches are tentatively identified as massive alpha (α_m). It is also suggested that this alloy forms α_m because it contains slower diffusing refractory elements which increase the kinetic differences between nucleation and growth α and α' formation. This α_m forms at intermediate cooling rates. The balance of the β-phase transformed to a much finer array of α' (martensite). This fine acicular martensite is the normally observed product of rapidly cooling such alloys through the β (bcc) to α (hcp) transformation. The unusual large plates were examined by conventional (TEM) and scanning transmission electron microscopy (STEM). They were found to be hcp α with the same composition as the base metal, with a high density of $\langle \bar{a} \rangle$ dislocations throughout the plate and a still higher density at a linear sub-boundary found close to the center of each plate. $\langle \frac{\bar{c}}{2} \rangle$ accommodation dislocations and associated stacking faults have also been identified. The large plates are often observed to intercept each other at a well-defined, planar interface. In these cases, they are shown to be $(10\bar{1}1)$ twin related. It is concluded that these large plates are also martensite. Because of the difference in morphology between these and the fine martensite, it is suggested that these have a different habit plane.

When α+β Ti alloys are heated to just above the β transus and water quenched, they typically transform to a fairly uniform size distribution of acicular martensite (1). The variations in martensite plate size which are observed are readily attributable to the physical partitioning of the parent β-phase. In the work reported here, cooling rates somewhat slower than those obtained in water quenching were employed with a rather surprising effect on the microstructure. It is the purpose of this paper to describe these results and to offer a qualitative explanation of them.

Experimental

Cylindrical specimens 6.3mm in diameter were resistance heated to about

1900K over about 25mm of their length and air cooled. The variation of temperature with time at the center of the heated zone was measured by an attached thermocouple. The central section of the hot zone was removed by sectioning with a diamond saw. This material was polished and etched for light metallography. Specimens for electron microscopy were polished in a perchloric-alcohol solution (3) and examined in a JEOL 120CX microscope.

Results and Discussion

Optical metallography showed four microstructural features which were morphologically distinct. These include:

1. large, clear martensite plates which typically contain a mid rib and which are similar in appearance to "butterfly martensite" in Fe-Ni alloys (2). These are referred to as large plates.

2. irregular large regions which are thought to be a massive transformation product similar to that reported in a number of binary Ti alloys (3). These are referred to as massive α, although the evidence for them being a massive transformation product is partly circumstantial.

3. small acicular plates which are typical of hexagonal α' martensite in $\alpha+\beta$ Ti alloys. These are referred to as small plates.

4. a fine layer of equilibrium α-phase heterogeneously nucleated on the grain boundaries.

These features are all observable in the light micrograph of Figure 1a. The large plates are shown in more detail in Figure 1b. Two additional features are noteworthy here: The mid rib in the large plates and the common occurrence of these plates in pairs. The individual plates in such pairs are separated by a very straight interface.

Transmission electron microscopy (TEM) was used to study the internal structure and crystallography of these features.

The small plates are shown in the TEM micrograph of Figure 2a. These can be seen to be irregularly shaped, presumably due to the impingement of smaller secondary plates. They seldom contain internal twins which suggests that the lattice invariant deformation is accomplished by slip.

The straight interfaces between two abutting large plates such as seen in Figure 1b also appear to be quite straight when examined by TEM (Fig. 2b). Selected area diffraction across such an interface shows that the plates are $(10\bar{1}1)$ twin related with a slight misorientation (Fig. 3). This is consistent with them being different variants of a transformation product which obeys the Burgers orientation relationship. Since martensitic α (1), massive α (3) and nucleation and growth α all exhibit the Burgers relation, the above observation is not helpful in determining the nature of the large plates. Immediately apparent, however, is the high dislocation density and the change of contrast about the center line of the left hand plate. The change is due to a misorientation across the center line corresponding to a rotation of ~ 0.5 degree about the $\langle c \rangle$ axis. Contrast experiments showed the existence of long, predominantly straight dislocations, with steps in them, lying normal to the plate center line

Fig. 1 - Light micrographs showing, (a) three types of transformation products and (b) higher magnification of a pair of large plates.

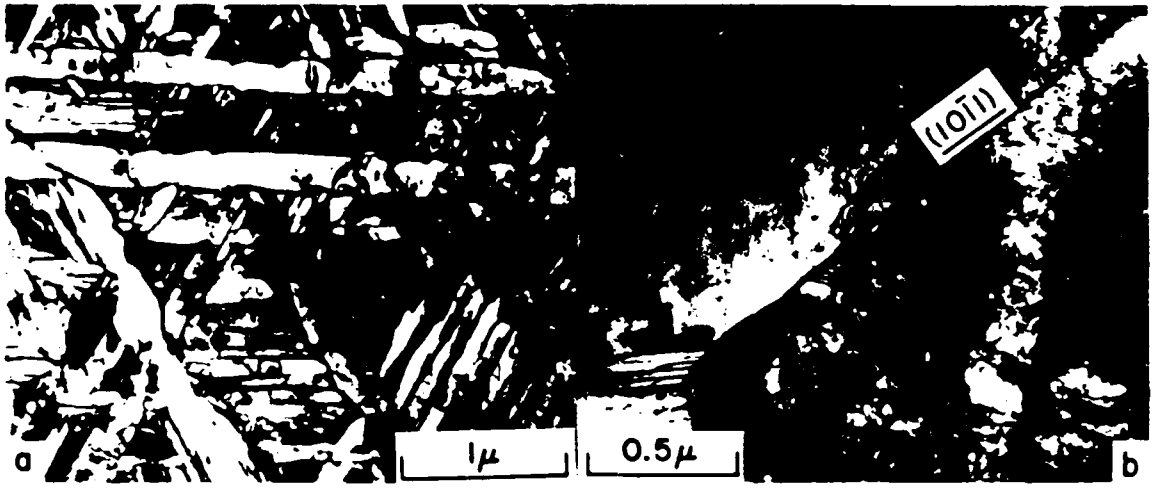

Fig. 2 - TEM micrograph of two martensite types.
a) small plates b) large plates

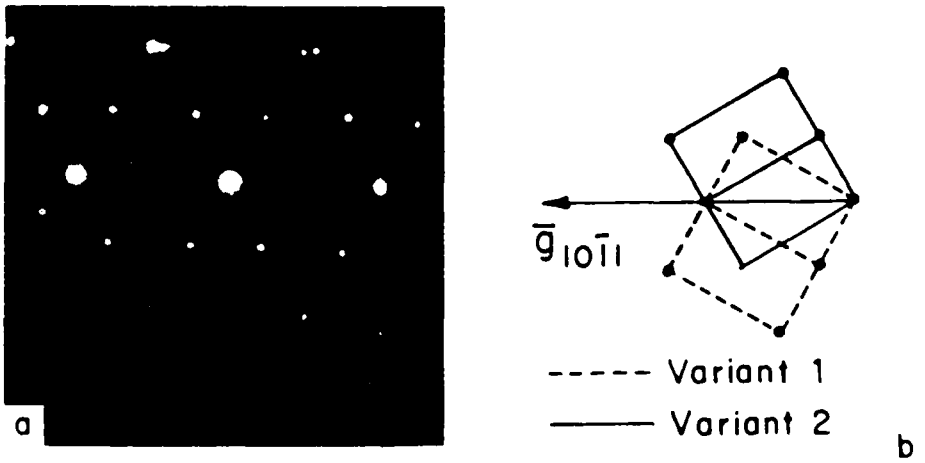

Fig. 3 - SAD pattern (a) of area in Figure 2b showing twinned relation as seen from (b).

(Fig. 4). The density of these dislocations was lower near the perimeter of the large plates. These dislocations are seen on edge in Figure 5a and the stacking faults associated with them are shown by tilting in Figure 5b. Some of the remaining <a> dislocations are also in contrast in Figure 5b. The latter have random configurations and are homogeneously distributed (unlike the arrays produced by room temperature deformation of this alloy).

Both types of dislocation are slightly more prevalent near the center of the plate but no kind of array can be seen at the center-line as would be expected for a low angle boundary. In this respect, the center-line appears more like a dislocation cell boundary than the classical mid rib which results from the change from twinning to slip as the operative lattice invariant deformation mode as found in Fe-Ni martensites.

STEM microanalysis established that there was no detectable concentration profile across the large plates and that they had the same composition as the small plates (i.e., the base composition since there is no retained β in these alloys). The high dislocation density (including the mid rib) and the pair-wise occurrence of the large plates which is self-accommodating, suggests that the large plates are martensitic. In fact, the large plates are strikingly similar to the butterfly martensite observed in Fe-Ni-C alloys by Umemoto and Tamura(2). They point out that in these alloys systematic changes in M_s temperature and habit plane correspond to different morphologies.

Intuitively it would seem that the large plates form first, i.e., at a higher M_s temperature. Thus, we suggest that a similar situation exists in both Fe-Ni-C and this Ti alloy. That is, the competition between the various forms of hexagonal transformation product is nearly balanced in this alloy.

From the light micrograph of Figure 1a, it is inferred that the heterogeneous nucleation and growth α forms first and "decorates" the prior β grain boundaries. This is followed by the large and small plate martensites with their successively lower M_s temperatures. The product which we term massive α has to compete with all three of these products. Consistent with this is the fact the massive phase has only been observed in very limited regions approximately parallel to the edge of the specimen. Thus, it would appear that its formation occurs at critical cooling rates.

Finally, it is worth inquiring why the massive α has not been observed in other Ti alloys such as Ti-6Al-4V or Ti-8Al-1Mo-1V. It is our view that both of these alloys have compositions which promote the nucleation and growth of α and thus the massive α formation becomes non-competitive in these alloys. In the latter alloy the higher Al content accelerates α-phase nucleation, whereas in the former, V is a more rapidly diffusing element than the Mo, Ta or Nb, which leads to more rapid growth of α. Both of these compositional factors favor α_m formation. Thus, the alloy we have studied happens to have a wider range of cooling rates over which massive α formation is at least somewhat competitive. Further work is planned to quantify these factors.

Acknowledgment

This work was supported by the Office of Naval Research.

References

1. [illegible] and M. J. Blackburn, [illegible], 606 (1967).
2. [illegible] and T. Tamura, [illegible]; MIT, Cambridge, MA 1979.
3. [illegible], Met. Trans. 8A, 1885 [illegible].

Fig. 4 - TEM micrograph showing high density of $\langle \frac{\bar{c}}{2} \rangle$ dislocations near center of large plate.

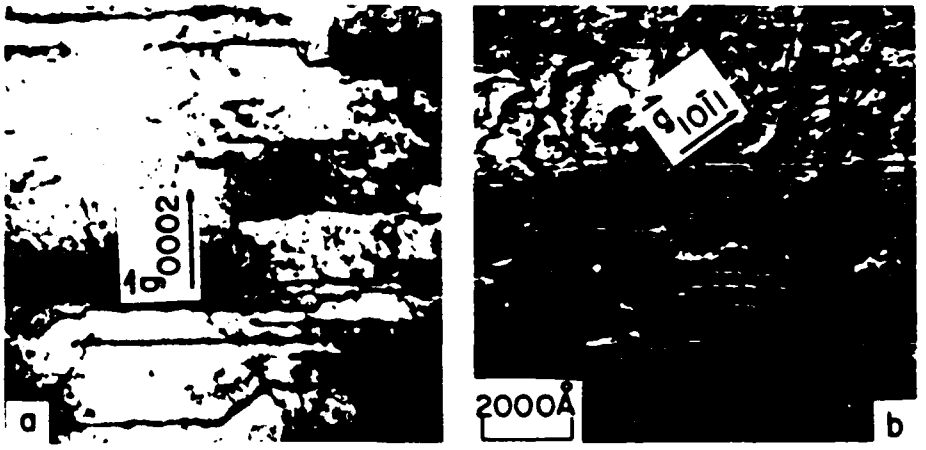

Fig. 5 - TEM micrographs showing only $\langle \frac{\bar{c}}{2} \rangle$ dislocations (a) and associated faults plus $\langle \bar{a} \rangle$ dislocations (b).

APPENDIX E

THE EFFECT OF BORON ON WELDMENT MICROSTRUCTURES IN THE Ti-6Al-2Nb-1Ta-1Mo ALLOYS

(Paper published in Titanium Science and Technology, Proceedings of the Fifth International Conference in Titanium, Munich, FRG, September 1984, G. Lutjering, U. Zwicker, W. Bunk, eds., Deutsche Gesellschaft fur Metallkunde E. V., Oberursel, FRG, 1985, pp. 799 - 805).

THE EFFECT OF BORON ON WELDMENT MICROSTRUCTURES IN THE Ti-6Al-2Nb-1Ta-1Mo ALLOY

R. E. Lewis, Lockheed Palo Alto Research Laboratory, Palo Alto, CA., USA
W. C. Coons, Consultant, San Jose, CA., USA
F. A. Crossley, Lockheed Missiles & Space Co., Inc., Sunnyvale, CA., USA
I. L. Caplan, Research Metallurgist, Arnold, MD., USA
W. E. Lukens, Welding Scientist, Annapolis, MD., USA

Introduction

A small amount of boron can be present in titanium alloys, introduced as an impurity in master alloys. Unless controlled, certain master alloys may contain a sufficient quantity of boron to result in a residual amount greater than 0.003 wt% in the final product. Additionally, boron can be introduced during the processing of material such as weld wire. Previous studies have shown that small amounts of boron added to titanium can affect microstructure (1), ductility (2), and toughness (3). This paper discusses the effect of low levels of boron on weld metal impact toughness. The effect of boron is also related to the solid-solid transformations and resultant microstructures in the weld fusion zones.

Procedure

Material. A near alpha titanium alloy, Ti-6Al-2Nb-1Ta-1Mo (Ti-6211), was used in this study. Two weldments of the alloy were prepared from 27-mm thick plate in an identical manner except that a different heat of Ti-6211 filler wire was used for each. The chemical composition of the filler wires is shown in Table 1. The boron content of each of the resultant welds is also included in the table. Except for boron, the chemistries of the weld fusion zones are essentially the same as the filler wire chemistries. The boron content was determined by argon plasma

Filler Wire Lot	Composition (wt%)							
	Al	Nb	Ta	Mo	C	N	O	H
A	6.0	2.1	1.1	0.8	0.01	0.008	0.07	0.003
B	5.8	2.1	1.2	0.7	0.02	0.008	0.07	0.003
	Cu	Mn	Si	Fe	Y	S	B	P
A	0.002	0.003	0.01	0.04	0.0005	0.001	0.002*	0.02
B	0.007	0.005	0.01	0.04	0.0010	0.002	0.004**	0.01

*Resultant weld metal, 0.001 wt%
**Resultant weld metal, 0.005 wt%

Table 1: Chemical analyses of Ti-6211 weld filler wires

emission spectroscopy to an accuracy of ±20 percent. The beta transus of lot A filler wire and lot B filler wire was determined to be 1020° and 1005°C, respectively.

Welding. The weldments were fabricated by the gas-tungsten-arc hot wire welding process using a single-vee, butt-joint design. The welding parameters for both weldments were exactly the same.

Dynamic Tear (DT) Toughness Tests. DT impact toughness tests (4) were performed on each of the weldments. Specimen orientation for the 25.4-mm thick dynamic tear specimens was transverse to the weld with the notch located in the centerline of the weld fusion zone and with the axis of the notch perpendicular to the plate surface. The test temperature was 0°C. A schematic of the DT specimen and test setup is shown in Fig. 1. An electron beam weld, embrittled by the addition of iron during the welding operation, is used to effectively generate the desired deep, sharp crack. Preparation of the DT specimens with the electron beam crack starter requires machining shallow grooves on both sides of the specimen. Stainless steel wire is then peened into both grooves and melted in from both sides. The bottom (tension) edge and sides of the crack starter weld are mechanically notched in a trapezoidal pattern to assist initiation of the crack in the brittle weld. Impact loading with a calibrated swinging weight is used to fracture the specimen and measure the energy absorbed. Since the energy required to initiate a crack in the embrittled electron beam weld is a very small portion of the total energy to fracture the specimen, the DT test generally reflects the resistance of the subject weld fusion zone to resist crack propagation under dynamic conditions.

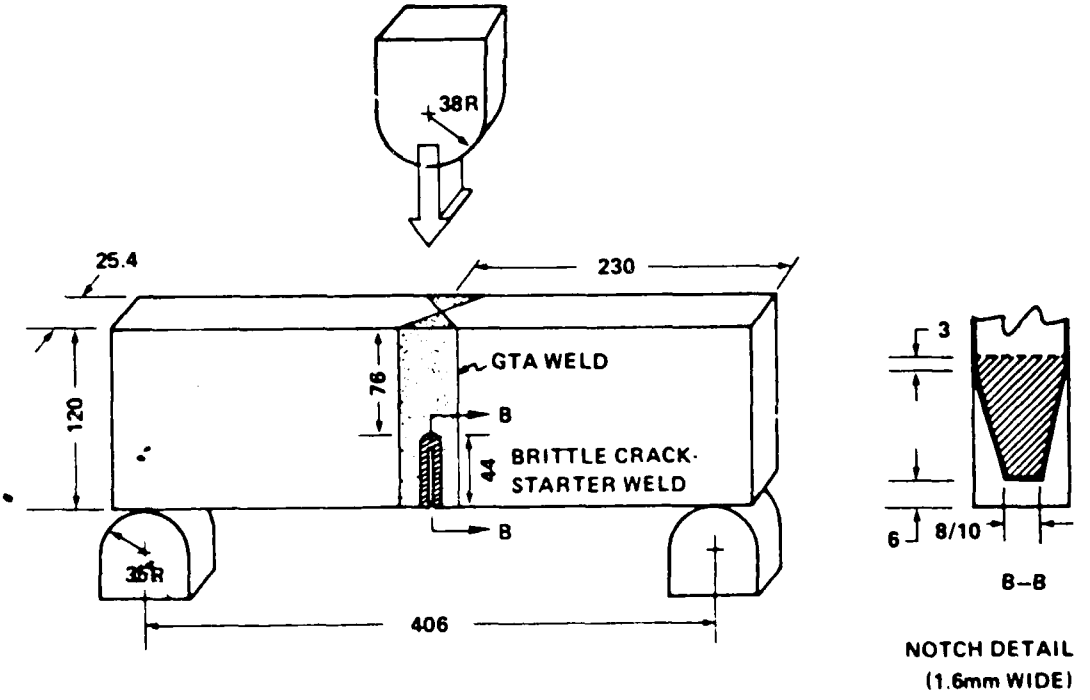

Fig. 1: Schematic of dynamic tear test

Results

The fusion zone impact toughnesses of the two weldments were found to be distinctly different: The weldment with high boron content of 0.005 wt% had average toughness values 40% lower than the standard weldment with 0.001 wt% (low) boron. The fracture was transgranular in those specimens with low boron content whereas the fracture path tended to follow along the long columnar prior beta grain boundaries in those specimens with high boron content. The microstructures of welds from the two wire heats differed significantly. The weld metal with low boron content contained finer, more equiaxed prior beta grains averaging 1.7 mm long and 0.7 mm wide. The weld metal with high boron content contained long epitaxial columnar prior beta grains averaging 2.8 mm long and 0.8 mm wide. In addition, the solid state transformation product was martensitic alpha (α') in the weldment with low boron and alpha formed by nucleation and growth transformation in the weldment with high boron.

Discussion

Detailed metallographic examination of the high boron filler wire used in the low toughness weldments disclosed a number of fine, angular, hard particles elongated in the axial direction of the wire, see Fig. 2. An electrolytic 1% chromic acid anodizing etchant readily revealed the particles whereas the conventional Kroll's reagent (HF-HNO_3-H_2O) did not, see Figs. 3 and 4. Microchemical analyses of these particles using Scanning Auger Electron Spectrocopy disclosed they are comprised entirely of titanium and boron, see Figs. 5 and 6. The titanium and boron contents were found to be approximately 50-50 atomic percent. It is tentatively concluded these particles are TiB. No such particles were found in the low boron filler wire used in the high toughness weldments. Further examination disclosed that these particles were not detected in the weld fusion zone of either the low toughness or high toughness weldments, but the solidification structure was distinctly different (Widmanstatten alpha plus beta versus martensite platelets of various sizes, respectively, see Figs. 7 and 8. During the welding process, the filler wire containing TiB particles is entirely melted and is diluted with the base metal. It is postulated that either some of the TiB particles do not dissolve entirely during the welding operation or they nucleate and reform at very high temperatures upon solidification in the weld fusion zone. These particles provide a preferential locus for nucleation and growth transformation of alpha from beta throughout the microstructure, thereby suppressing the transformation of beta to martensite on cooling of the weld fusion zone during the welding operation.

In order to get a better understanding of the role of the boride particles in the phase transformations, tips of wire samples from each lot were fused by localized heating and allowed to solidify in situ. Metallographic examination of the fused samples show boride particles only in the high boron lot of wire. It is clear from Fig. 9 that the boride particles nucleate the alpha phase.

Paltz et. al. (1) reported the titanium-rich end of the TiB phase diagram to have a peritectoid reaction: beta + TiB → alpha. It is hypothesized that this is the mechanism by which TiB particles nucleate alpha. The nucleation of alpha by the peritectoid reaction mechanism (above the

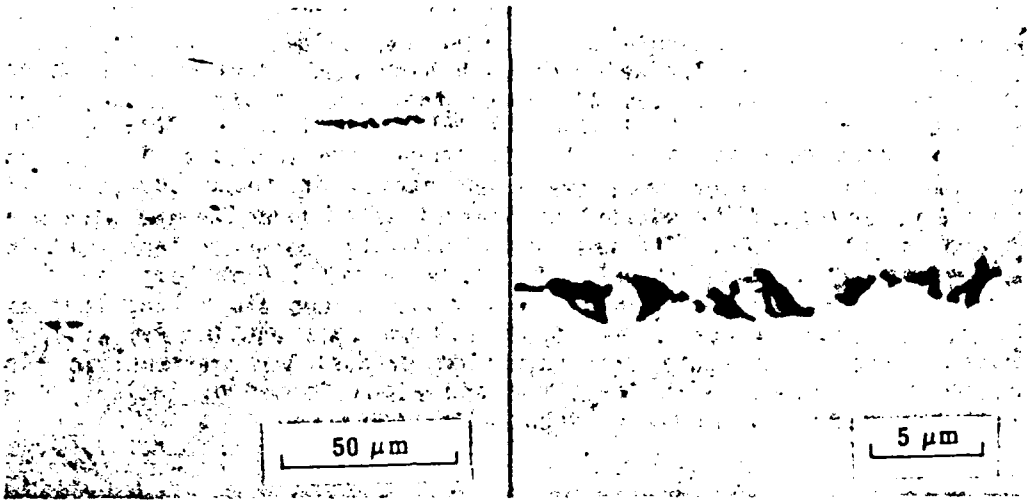

(a) (b)

Fig. 2: Optical micrograph of weld wire containing high (0.005 wt%) boron. Polished longitudinal section of the weld wire; wire axis is horizontal. Note hard particles (light) with interspersed voids (dark).

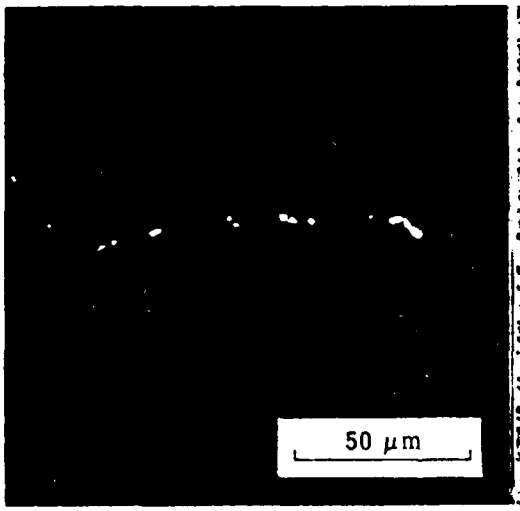

Fig. 3: Similar field as Fig. 2(a) but chromic acid anodized. Note bright appearance of hard particles.

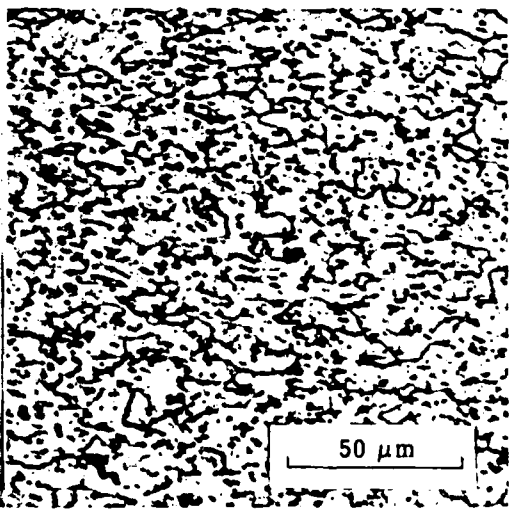

Fig. 4: Similar field as Fig. 2(a) but etched with Kroll's Reagent. Note inability to discriminate between general etching effects and hard particles

(a) (b)

Fig. 5: Secondary electron image of argon ion sputtered surface of longitudinal section of weld wire containing high boron. Hard particle (black) is bracketed by large voids (white). The small scattered, white-appearing particles are small pools of beta.

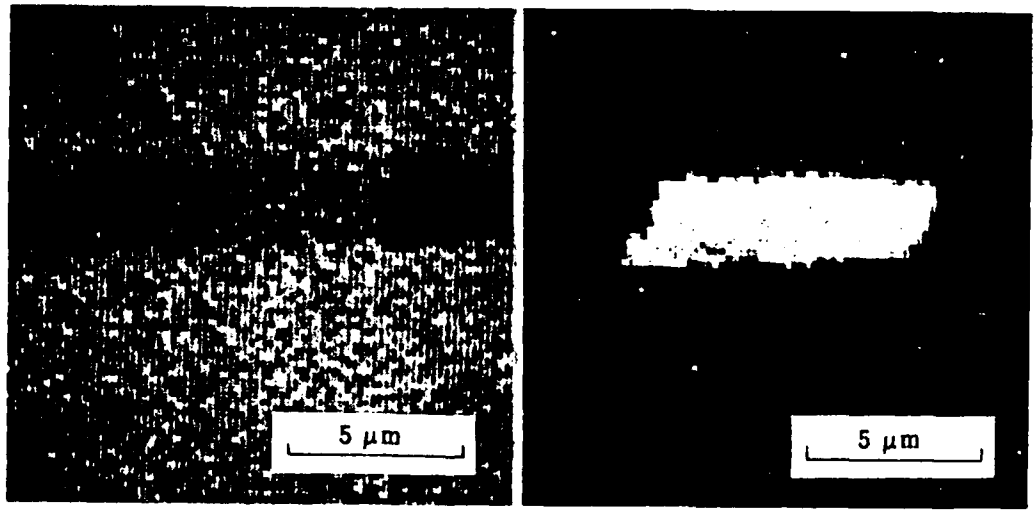

(a) (b)

Fig. 6: Scanning Auger Electron Spectroscopy images of the same field shown in Fig. 5(b). Titanium (a) and boron (b) were the only elements detected in the particles.

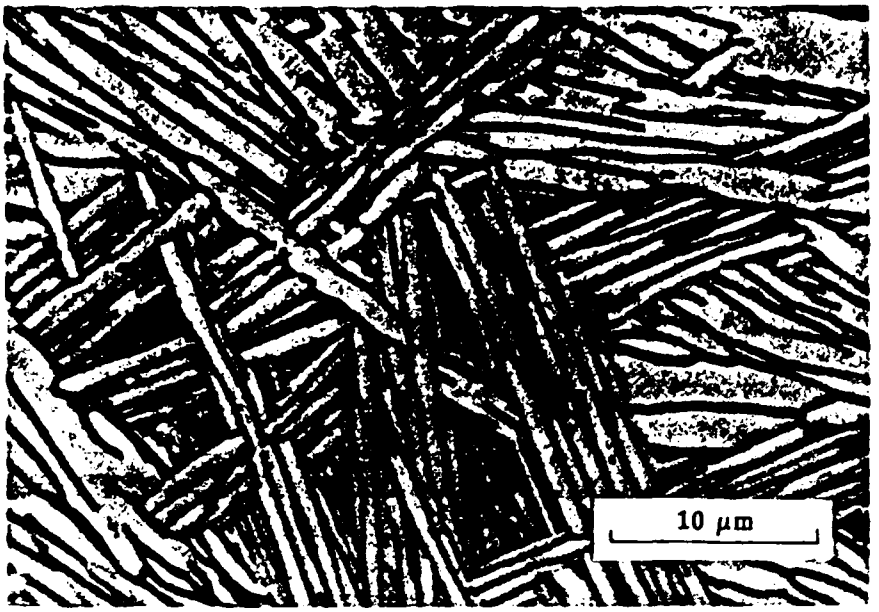

Fig. 7: Optical micrograph of Widmanstatten alpha plus beta microstructure in the fusion zone of the weldment produced from weld wire containing high boron. Etchant is HF-alcohol.

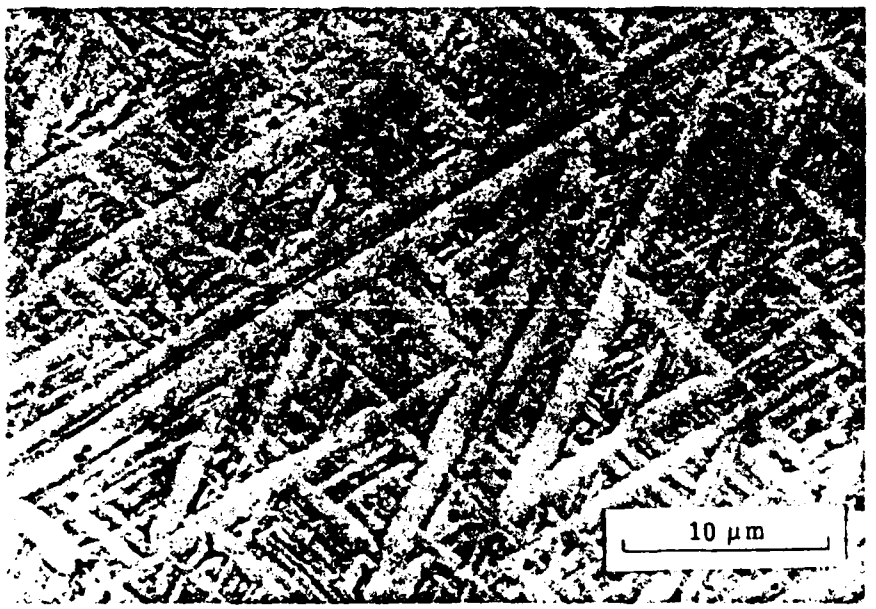

Fig. 8: Optical micrograph of martensite in the fusion zone of the weldment produced from weld wire containing low boron. Etchant is HF-alcohol.

transformation temperature of pure titanium) prevents the undercooling necessary to effect the martensitic transformation of beta to alpha. The existence of this peritectoid reaction is a key to the preferential formation of alpha at high temperature. It should be noted that only two other elements have a similar peritectoid reaction with titanium at very dilute levels: they are sulfur and carbon.

Conclusions

The analyses of filler wire and weld fusion zone microstructures verifies the presence of boron as an undesirable impurity. Furthermore, the peritectoid reaction, beta + TiB → alpha, proposed as the mechanism by which only 40 ppm of boron can suppress the martensitic transformation in the Ti-6211 alloy weld fusion zone by providing nucleation sites for alpha titanium in the form of submicroscopic particles of TiB.

Significantly reduced dynamic fracture toughness in titanium alloy welds can be caused by the presence of a small concentration of boron in the weld metal. Thus, it is important to control the boron content in final products to less than 0.003 wt%.

References

(1) A. E. Palty, H. Margolin, and J. P. Nielsen: Transactions of the ASM, 46 (1954) 312.
(2) H. R. Ogden and R. I. Jaffee: J. Metals 191 (1951) 335.
(3) S. M. Gurevich: Automatic Welding, No. 3 (1963) 28.
(4) P. P. Puzak and E. A. Lange: Naval Research Laboratory Report 6851 (Feb. 1969).

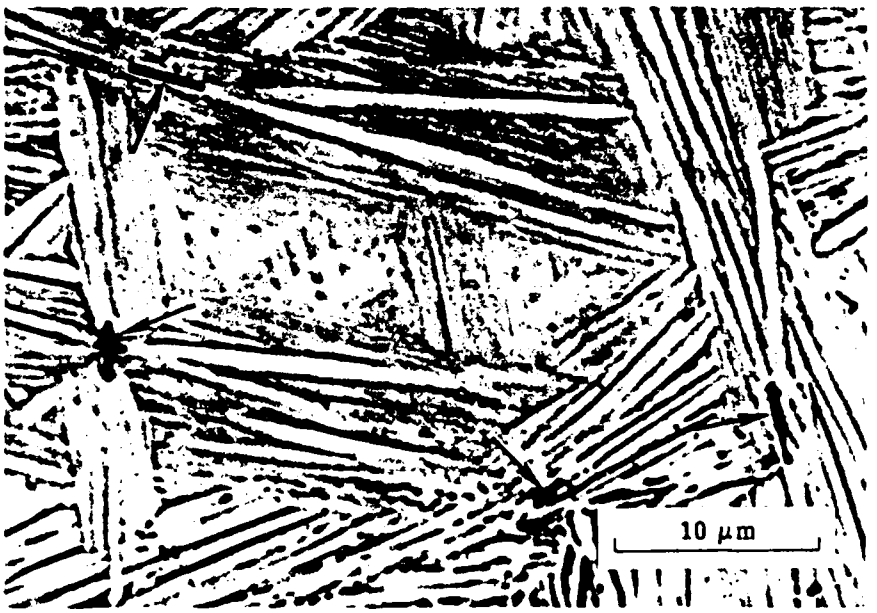

Fig. 9: Optical micrograph of microstructure in fused end of welding wire containing high boron. The dark appearing particles (see arrows) have been tentatively identified as TiB.

APPENDIX F

REPORT ON PREPARATION OF SPECIAL LOT OF Ti-6211 ALLOY PLATE (CONTROLLED ADDITIONS OF SULFUR AND YTTRIUM)

by

H. A. Waddell
RMI Company
Niles, OH

Final Report Prepared for

Lockheed Missiles & Space Co.
Sunnyvale, California 94088

SPECIAL LOT OF Ti-6211 ALLOY PLATE

Customer Order SQ26M-Z040F
RMI Mill Order 81148

RMI Company
1000 Warren Ave.
Niles, OH 44446

October 21, 1980

Supervised and Reported by:

H. A. Weddell
Manager, R & D Services

Directed by:

H. B. Bomberger
Director-Metallurgy and Research

Introduction

Lockheed Missiles & Space Co. ordered a series of Ti-6211 alloys all having the same composition of Ti-6Al-2Cb-1Ta-1Mo (weight percent) with different amounts of sulfur and yttrium added. The ingots were manufactured using the melting, forging, and hot working practice normally used for producing large plates of beta-processed Ti-6211 for structural applications.

Consolidation and Melting

The raw materials used to prepare the Ti-6Al-2Cb-1Ta-1Mo alloy are detailed in Table 1. RMI commercial titanium sponge was used as the basic raw material with the Al, Cb, Ta, and Mo added as Al-Cb-Ta and Al-Mo master alloys. The additional aluminum necessary was added as commercially pure aluminum pellets. Yttrium additions were made by blending fine yttrium oxide powder in the melt charge. Details of the yttrium additions are shown in Table 2. Sulfur additions were made by blending sulfur powder with titanium fines. The details of the sulfur additions are shown in Table 3.

All materials were blended together and compacted to 1.5 by 8 by 15-inch compacts which sectioned for electrode construction. These sections were welded into a 3 by 4 by 45-inch long electrode for first-stage melting (Table 4). First-stage consumable arc melting into a 6-inch diameter crucible was performed under vacuum with volts, amps and total melt time shown in Table 5. After cooling the cast was removed from the crucible and the skull removed by band-saw cutting. The cast was inverted and a header was welded to the bottom. The second-stage melting operation was performed under partial argon pressure in an 8-inch diameter crucible. Every attempt was made to maintain consistent melting parameters for each heat.

Chemical Composition

The chemical composition for each heat is shown in Table 6. The sulfur analyses were supplied by Herron Testing Laboratories of Cleveland, Ohio.

Ingot Conversion to Plate

The top skull was removed by cutting prior to further processing of the ingots. No surface preparation of the ingots was done prior to forging.

A schematic diagram of the hot working of the ingots is shown in Exhibit A. The ingots were hammer forged to 1-inch thick plate from a gas-fired furnace operating at a 2100F aim temperature at Jos. Dyson & Sons, Inc. in Painesville, Ohio. Specifics of the forging process are detailed in Table 7. Large differences in the surface appearance of the various alloys were not apparent.

Material was cut from the 1-inch plate for analyses representing top and bottom. The remaining material was conditioned, cut into plates 1 by 5 by 8 inches in length for hot working on RMI research rolling mill. This hot working was performed from a 1950F furnace temperature and proceeded in a direction 90 degrees to the original forging direction with a reduction of plate thickness from 1 inch to 0.75 inch. Some minor conditioning was then performed on all pieces before reheating for final rolling. The plates were then reheated in a 1950F furnace and rolled to 0.5-inch thick plate in the original forging direction. The final plates had a nominal size of 0.5 by 7 by 11 inches. They are in the as-hot-rolled condition but have been cleaned by grit blasting and light acid pickling.

Chemical Composition on 0.5-Inch Thick Plate

A schematic diagram of the cutting of the 1-inch thick plate is shown in Exhibit B. Additional chemical analyses were requested from each of the four plates from the six Ti-6211 heats. The drawing shows the plate ends where the chemical specimens were taken. The chemical analyses are contained in Table 8. The chemical analysis technique used to determine elemental compositions of the various alloys is contained in Table 9.

TABLE 1. RAW MATERIALS FOR Ti-6211 EVALUATION

Titanium Sponge	RMI Lot 1455 (0.07 O, 0.02C, 0.006N)
Al-Cb-1Ta Master Alloy	44Al-36.2Cb-18.1Ta (Union Carbide)
Al-Mo Master Alloy	43Al-51Mo
Aluminum Pellets	Commercial purity
Yttrium	Y_2O_3 powder, -270 mesh, 99.5 percent purity

TABLE 2. METHOD OF ADDING YTTRIUM

Heat No.	Yttrium Aim Weight %	Yttrium Addition Agent	Yttrium Added Weight %
X-20052	--		
X-20053	--		
X-20054	--		
X-20055	0.0075	Y_2O_3	0.015
X-20056	0.0075	Y_2O_3	0.015
X-20057	0.0075	Y_2O_3	0.015

TABLE 3. METHOD OF ADDING SULFUR

Heat No.	Weight %	Sulfur Addition Agent*
X-20052	--	
X-20053	0.0025	Commercial Sulfur
X-20054	0.0075	Commercial Sulfur
X-20055	--	
X-20056	0.0025	Commercial Sulfur
X-20057	0.0075	Commercial Sulfur

*Commercial purity

TABLE 4. ELECTRODE PREPARATION

Compact Size	1.5 by 8 by 15 inches
Compact Weight	8800 grams
Number of Compacts per Heat	3
Total Weight	26308 grams
First-Stage Electrode Size	3 by 4 by 45 inches
Electrode Welding	Thoriated-Tungsten Tip Electrode with Argon Shielding

TABLE 5. MELTING PROCEDURE

Ingot No.	First Stage		Total Melt Time min.	Second Stage		Total Melt Time min.
	Volts	Amps		Volts	Amps	
X-20052	28	2900	19.27	37	5000	15.13
X-20053	28	2900	18.12	37	5000	15.55
X-20054	28	2900	18.38	37	5000	16.47
X-20055	28	2900	17.46	37	5000	16.02
X-20056*	28	2900	17.34	37	5000	17.04
X-20057*	26	2900	19.38	37	5000	16.46

*Melts were very erratic with a problem maintaining arc during both first- and second-stage melting.

TABLE 6. CHEMICAL COMPOSITION OF INGOTS

Heat No.	Weight, percent									ppm	
	C	N	Fe	Al	Mo	Cb	Ta	O	S	H	Y
X-20052	0.02	0.007	0.03	5.9	0.72	2.04	1.06	0.067		41	
	0.04	0.006	0.03	5.8	0.84	1.82	0.98	0.070		42	
Aim				6.0	0.8	2.00	1.00		-		-
X-20053	0.02	0.007	0.03	5.7	0.72	1.84	0.92	0.081	0.006	36	
	0.03	0.005	0.03	6.8	0.98	2.15	1.10	0.080	0.003	39	
Aim				6.0	0.8	2.00	1.00		0.0025		-
X-20054	0.02	0.006	0.03	5.7	0.82	1.96	1.0	0.070	0.008	32	
	0.04	0.006	0.02	5.7	0.78	2.13	1.15	0.070	0.007	33	
Aim				6.0	0.8	2.00	1.00		0.0075		-
X-20055	0.03	0.005	0.03	5.5	0.82	2.00	1.0	0.079		41	33
	0.04	0.008	0.03	6.2	0.84	2.20	1.16	0.082	-	40	53
Aim				6.0	0.8	2.00	1.00				75
X-20056	0.04	0.008	0.05	5.7	0.74	1.96	1.05	0.098	0.007	69	55
	0.06	0.007	0.02	5.6	0.66	1.92	1.00	0.091	0.005	56	45
Aim				6.0	0.8	2.00	1.00		0.0025		75
X-20057	0.04	0.006	0.03	6.0	0.68	2.04	1.05	0.080	0.009	37	66
	0.02	0.010	0.04	5.1*	0.72	1.84	0.98	0.087	0.004	49	66
Aim				6.0	0.8	2.00	1.00		0.0075		75

*Sample taken from extreme bottom of ingot

TABLE 7. FORGING PROCEDURE 7.75-INCH DIAMETER INGOT TO 1 INCH BY 5 INCHES BY RANDOM LENGTH PLATE

Heat No.	Time in Furnace min.	Temperature in Furnace F	Forge Size in.	Reheat Time min.	Finish Forge Size in.	Finish Temperature F
X-20052	120	2100	2 x 5 x RL	15	1.125 x 5 x RL	1750
X-20053	123	2100	2 x 5 x RL	20	1.125 x 5 x RL	1720
X-20054	127	2090	2 x 5 x RL	25	1.125 x 5 x RL	1755
X-20055	120	2100	2 x 5 x RL	17	1.125 x 5 x RL	1745
X-20056	125	2105	2 x 5 x RL	25	1.125 x 5 x RL	1760
X-20057	130	2100	2 x 5 x RL	15	1.125 x 5 x RL	1750

Large differences in surface appearance of the various alloys were not apparent.

TABLE 8. CHEMICAL COMPOSITION OF 0.5-INCH THICK PLATES

Heat No.	Weight, percent									ppm	
	C	N	Fe	Al	Mo	Cb	Ta	O	S	H	Y
X-20052-1A	0.01	0.005	0.05	6.0	0.9	2.10	2.10	0.071	-	58	-
-1B	0.02	0.008	0.02	5.8	0.8	2.20	1.07	0.072	-	60	-
-2A	0.02	0.008	0.03	5.7	0.9	2.10	1.03	0.074	-	58	-
-2B	0.03	0.009	0.03	5.8	0.9	2.10	1.01	0.073	-	62	-
-3A	0.03	0.008	0.04	5.8	0.9	2.08	1.04	0.070	-	62	-
-3B	0.01	0.006	0.04	5.9	0.8	2.10	1.04	0.074	-	68	-
-4A	0.02	0.004	0.04	5.8	0.8	2.16	1.05	0.056	-	56	-
-4B	0.01	0.010	0.05	5.8	0.9	2.15	1.07	0.066	-	49	-
X-20053-1A	0.02	0.004	0.03	5.7	0.8	2.05	1.02	0.076	0.003	43	-
-1B	0.03	0.008	0.03	5.6	0.8	2.05	1.03	0.082	0.002	41	-
-2A	0.02	0.006	0.03	5.7	0.8	2.05	1.00	0.082	0.002	35	-
-2B	0.03	0.006	0.02	5.6	0.8	2.0	0.97	0.082	0.003	42	-
-3A	0.02	0.006	0.03	5.6	0.8	2.00	0.99	0.085	0.005	50	-
-3B	0.02	0.006	0.03	5.7	0.8	1.99	0.99	0.078	<0.001	47	-
-4A	0.02	0.004	0.03	5.6	0.8	2.03	0.97	0.079	0.002	45	-
-4B	0.02	0.008	0.04	5.7	0.8	2.05	1.00	0.076	0.002	49	-
X-20054-1A	0.02	0.005	0.03	5.8	0.8	2.05	0.96	0.070	0.007	57	-
-1B	0.02	0.010	0.03	5.8	0.8	2.02	0.97	0.068	0.004	41	-
-2A	0.02	0.009	0.03	5.7	0.8	2.04	1.00	0.070	0.005	53	-
-2B	0.02	0.008	0.03	5.7	0.7	2.03	1.01	0.078	0.005	44	-
-4A	0.03	0.008	0.03	6.1	0.8	2.17	1.05	0.072	0.004	56	-
-4B	0.03	0.008	0.02	6.1	0.8	2.17	1.07	0.074	0.004	49	-
[illegible]	0.02	0.009	0.03	6.0	0.8	2.04	1.01	0.068	0.005	50	-
[illegible]	0.02	0.009	0.03	6.0	0.8	2.09	1.00	0.070	0.006	49	-

(Continued)

AD-A184 286 METALLURGICAL INVESTIGATION OF HOT DUCTILITY LOSS IN TI-6211 ALLOY(U) LOCKHEED MISSILES AND SPACE CO INC PALO ALTO CA R E LEWIS 15 JAN 86 LMSC-F108004 3/3

UNCLASSIFIED N00014-79-C-0449 F/G 11/6 NL

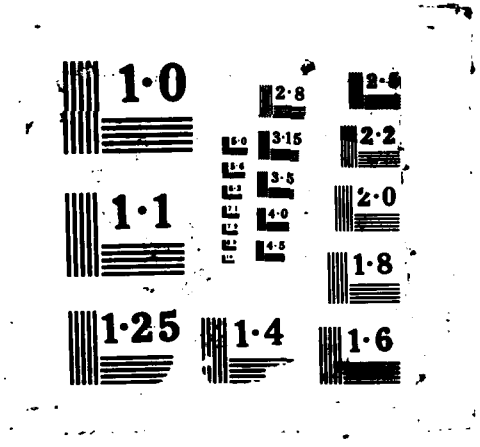
1·0
1·1
1·25
2·8
3·15
3·5
4·0
4·5
1·4
2·2
2·0
1·8
1·6

TABLE 8. CHEMICAL COMPOSITION OF 0.5-INCH THICK PLATES (Concluded)

RMI Company

F-11

Mill Order 81148

Heat No.	Weight, percent									ppm	
	C	N	Fe	Al	Mo	Cb	Ta	O	S	H	Y
X-20055-1A	0.02	0.008	0.03	5.9	0.9	2.17	1.07	0.070		80	65
-1B	0.02	0.005	0.05	6.1	0.8	2.20	1.07	0.068		80	70
-2A	0.02	0.004	0.03	5.8	0.8	2.06	1.03	0.068		83	66
-2B	0.02	0.008	0.04	5.7	0.9	2.20	1.02	0.069		66	70
-3A	0.03	0.004	0.05	6.0	0.8	2.03	1.02	0.073		71	58
-3B	0.03	0.004	0.04	5.8	0.8	2.01	1.05	0.070		84	60
-4A	0.02	0.008	0.03	6.1	0.9	2.05	1.01	0.066		85	57
-4B	0.03	0.008	0.03	6.1	0.8	2.01	1.00	0.074		100	56
X-20056-1A	0.03	0.010	0.03	6.0	0.9	2.20	1.08	0.093	0.003	82	73
-1B	0.02	0.010	0.03	6.1	0.8	2.19	1.08	0.084	<0.001	80	70
-2A	0.03	0.009	0.03	5.7	0.8	2.03	1.02	0.082	0.004	92	74
-2B	0.03	0.006	0.03	6.0	0.8	2.02	0.98	0.078	<0.001	96	68
-3A	0.02	0.010	0.03	6.1	0.9	2.11	1.06	0.092	0.002	92	71
-3B	0.02	0.010	0.04	5.9	0.8	2.12	1.05	0.090	0.002	85	71
-4A	0.02	0.010	0.03	6.0	0.8	2.12	1.07	0.077	<0.001	82	76
-4B	0.02	0.010	0.03	6.0	0.8	2.20	1.05	0.082	0.002	83	68
X-20057-1A	0.02	0.008	0.03	5.8	0.8	2.16	1.06	0.074	0.004	73	82
-1B	0.02	0.007	0.03	6.0	0.9	2.04	1.08	0.074	0.004	86	80
-2A	0.02	0.009	0.03	6.0	0.8	2.20	1.08	0.074	0.004	77	74
-2B	0.03	0.006	0.03	6.0	0.9	2.12	1.10	0.069	0.006	73	62
-3A	0.02	0.008	0.03	5.9	0.8	2.20	1.10	0.095	0.006	76	74
-3B	0.02	0.008	0.03	5.9	0.9	2.15	1.10	0.070	0.004	68	74
-4A	0.03	0.004	0.03	6.1	0.8	2.15	1.08	0.070	0.005	77	70
-4B	0.02	0.004	0.04	6.0	0.9	2.20	1.10	0.071	0.003	79	70

TABLE 9. CHEMICAL ANALYSIS TECHNIQUE

Element	Method Used for Analysis	Minimum Detectable Amount	Accuracy (± range) per Technique
Al	Gravimetric	0.05%	1-10% ±0.2%
Cb	X-ray Quan.	Limited to Standards 1.367% to 3.479% Cb	1/2 of 1%
Ta	X-ray Quan.	Limited to Standards 0.633% to 1.579% Ta	1/2 of 1%
Mo (Alloy Addition)	Photometric	0.01%	<0.1% ±0.02% 0.1% to 0.8% ± 0.04%
N	Wet	0.001%	All ±0.003/or ±10%, whichever is higher
H	Hot Extraction	0.0002%	All ±0.0002/or ±10%, whichever is higher
Fe	Spectrographic/or Photometric	0.01%	<0.4% ±0.04%
C	Combustion	0.005%	All ±0.002/or ±20%, whichever is higher
S	Leco Combustion	<0.001	±0.0003%
Y	RMI-Spectrograph USS-Chemical Separation - Spectrograph	0.001% 0.003%	±0.001/or ±10%, whichever is higher
O	Fusion (Thermoconductivity Detection or Intra-Red Detection)	0.003%	<0.1% ±0.01/or ±10%, whichever is higher

EXHIBIT A. SCHEMATIC DIAGRAM OF Ti-6211 HOT WORKING

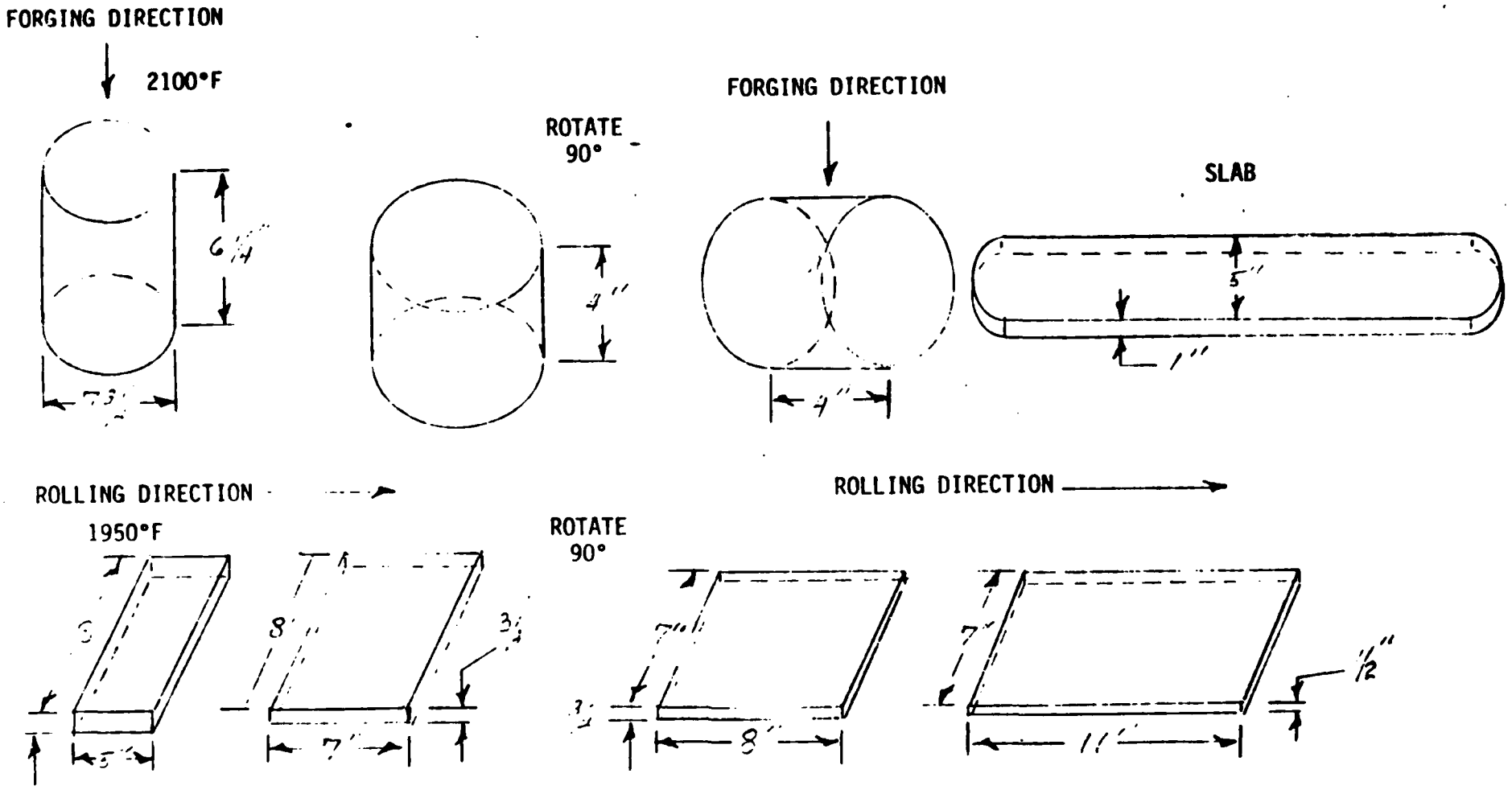

EXHIBIT B. SCHEMATIC DIAGRAM OF Ti-6211 0.5-INCH THICK PLATE

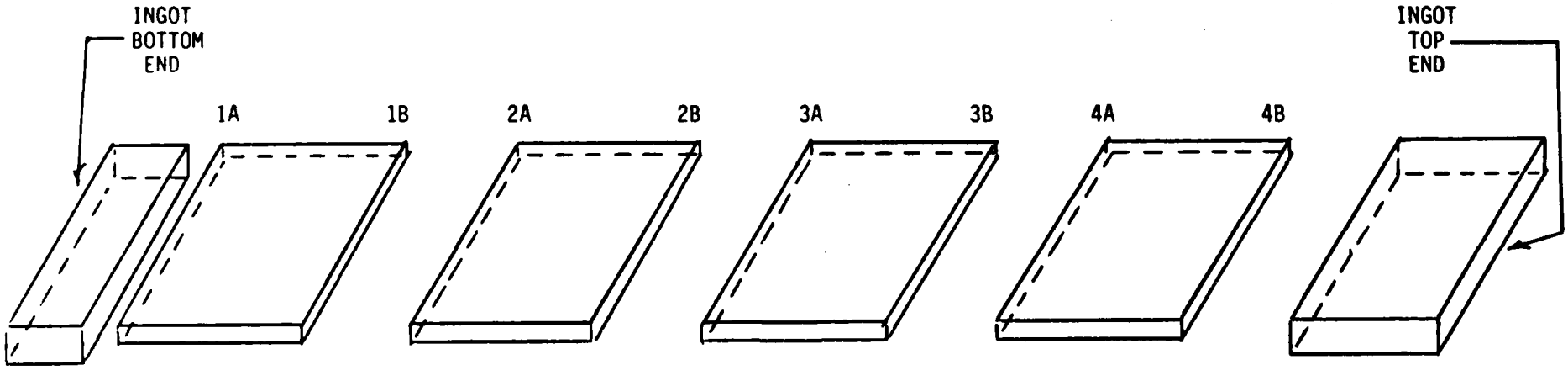

END

10-87

DTIC